BULK METALLIC GLASS MATRIX COMPOSITES: PROCESSING, MICROSTRUCTURE, AND APPLICATION AS A KINETIC ENERGY PENETRATOR

Thesis by

Richard B. Dandliker

In Partial Fulfillment of the Requirements

for the Degree of

Doctor of Philosophy

California Institute of Technology

Pasadena, California

1998

(Submitted October 24, 1997)

ACKNOWLEDGMENTS

None of this work would have been possible without Dr. Bill Johnson, a man whose intuition and insight is often stupefying to behold. I must thank him for giving me the freedom to find a path which truly made my research dear to me, and for his amazingly infectious enthusiasm for science and discovery.

Special thanks also goes to Dale Conner, my collaborator for much of the work on this project and a good friend. His expertise in mechanics was very valuable, as were our discussions which helped me focus on what was important.

Many other members of the Johnson group, both past and present, have also been a great help. Dr. Atakan Peker's work in developing the first Vitreloy™ alloys laid the basis for much of this study. Drs. Peker and David S. Lee showed me how to operate most of the lab equipment and many of the techniques I was to use later in my graduate career. Dr. Ralf Busch was always willing to give me a tutorial on thermodynamics and the glass transition. Drs. Susanne Schneider, Ulli Geyer, and Y. J. Kim brought a wide range of knowledge and experience to our discussions. Dr. Mo Li was a great source of stability in the group during his time at Caltech, and his work always made me grateful for the opportunity to be an experimentalist. The work of Dr. Xianghong Lin provided essential insights and brought increased understanding to processing techniques for metallic glass. I would also like to thank Haein Choi-Yim for many useful discussions about composites and processing. The rest of the Johnson group, including Steven Glade, Sven Bossuyt, Valerie Scruggs, Jian Li, Andreas Masuhr, Eric Bakke, Brian Burkholder, Wenshan Liu, Andy Waniuk, and de facto member Dr. Karina Montilla Edwards, helped make my tenure at Caltech thoroughly enjoyable.

Carol Garland was invaluable for help and instruction with the TEM, as well as other microscopy techniques. Professor Brent Fultz instructed me in electron and x-ray diffraction both in the classroom and the laboratory. Dr. Channing Ahn happily tolerated my repeated borrowing of his 35 mm camera. Dr. Jack Worrell at the University of Southern California operated the scanning Auger microscope and was of great help in the analysis of data from that instrument. Pam Albertson was always eager to help find creative solutions to any administrative or budgetary problem. Eve Kiefer and Elaine Granger were also instrumental in making sure the lab ran smoothly.

This report is based upon work supported in part by the U. S. Army Research Office under grant number DAAH04-95-1-0233. Robert Dowding from the Army Research Laboratory at Aberdeen was very helpful in providing tungsten heavy alloy samples and background data for penetrator testing. I would also like to thank the National Science Foundation for the fellowship which supported me through the first three years of graduate school.

Amorphous Technologies International (Laguna Niguel, California) provided some samples of metallic glass, and made their facilities and equipment available to me without hesitation. Dr. Michael Tenhover has always been a great help and a nearly limitless source of ideas. In addition, I would like to thank Dr. Tenhover and the Carborundum Company for supplying silicon carbide fibers and preforms, and performing scanning Auger and secondary ion mass spectrometry (SIMS) analysis on silicon carbide reinforced samples.

Finally, I would like to thank my parents and my brother for always being encouraging and supportive of my education and research. And to Mary, thanks for putting up with me throughout the entire process and for helping me make it through with my sanity intact.

ABSTRACT

The development of alloys with high glass forming ability allows fabrication of bulk samples of amorphous metal. This capability makes these materials available for applications which require significant material thickness in all three dimensions. Superior mechanical properties and advantages in processing make metallic glass a choice candidate as a matrix material for composites.

This study reports techniques for making composites by melt-infiltration casting using the alloy $Zr_{41.2}Ti_{13.8}Cu_{12.5}Ni_{10.0}Be_{22.5}$ (Vitreloy™ 1) as a matrix material. Composite rods 5 cm in length and 7 mm in diameter were made and found to have a nearly fully amorphous matrix; there was less than 3 volume percent crystallized matrix material. The samples were reinforced by continuous metal wires, tungsten powder, or silicon carbide particulate preforms. The most easily processed samples were made with uniaxially aligned tungsten and carbon steel continuous wire reinforcement; the majority of the analysis presented is of these samples. The measured porosity was typically less than 3%. The results also indicate necessary guidelines for developing processing techniques for large scale production, new reinforcement materials, and other metallic glass compositions.

Analysis of the microstructure of the tungsten wire and steel wire reinforced composites was performed by x-ray diffraction, scanning electron microscopy, scanning Auger microscopy, transmission electron microscopy, and energy dispersive x-ray spectroscopy. The most common phase in the crystallized matrix is most likely a Laves phase with the approximate formula $Be_{12}Zr_3TiNiCu$. In tungsten-reinforced composites, a crystalline reaction layer

240 nm thick of tungsten nanocrystals in an amorphous matrix formed. In the steel reinforced composites, the reaction layer was primarily composed of a mixed metal carbide, mainly ZrC.

One promising application of the metallic glass matrix composite is as a kinetic energy penetrator material. Ballistic tests show that a composite of 80 volume percent uniaxially aligned tungsten wires and a Vitreloy™ 1 matrix has self-sharpening behavior, which is a necessary characteristic of superior penetrator materials. Small-scale tests with both aluminum and steel targets show that this composite performs better than tungsten heavy alloys typically used for penetrator applications, and comparably with depleted uranium.

TABLE OF CONTENTS

LIST OF FIGURES

LIST OF TABLES

NOTATION AND ABBREVIATIONS

BCC	body centered cubic
BF	bright field
C_p	specific heat at constant pressure
DF	dark field
DSC	differential scanning calorimeter
DU	depleted uranium
EDS	energy dispersive spectroscopy
EDXS	energy dispersive x-ray spectroscopy
E_m; E_f	elastic modulus of the matrix; fiber/wire
ESL	electrostatic levitator
f	volume fraction of fibers
G_{ic}	fracture energy of the interface
ΔG	Gibbs free energy of formation
ΔG_A	free energy of activation for transfer of atoms from the liquid to the crystal
ΔG_v	difference in free energy between the crystal and the liquid per unit volume
I	nucleation rate
K	thermal conductivity
L/D	length to diameter ratio
n	number of equilibrium number of crystalline clusters per unit volume
n_0	number of unassociated molecules per unit volume
n*	number of atoms on the surface of a critical nucleus
P/L	penetration depth to length ratio

R_f	radius of the fiber/wire
R_c	critical cooling rate
SAM	scanning Auger microscope
SEM	scanning electron microscopy
STEM	scanning transmission electron microscopy
S_c	surface area of a critical nucleus
T	absolute temperature
T_g	glass transition temperature
T_m	melting point
T_{rg}	reduced glass transition temperature (T_g/T_m)
TEM	transmission electron microscopy
v	velocity
Vitreloy ™1	metallic glass-forming alloy composition ($Zr_{41.2}Ti_{13.8}Cu_{12.5}Ni_{10.0}Be_{22.5}$)
WHA	tungsten heavy alloy
X-27C	designation for tungsten heavy alloy (see Table 4.2)
Z	net rate of transfer of atoms from the liquid to the embryo per unit area
υ	Poisson's ratio
η	viscosity
σ	liquid-crystal interfacial energy per unit area
τ	flow stress
γ	strain
$\dot{\gamma}$	strain rate

CHAPTER 1
INTRODUCTION

1.1 BULK GLASS FORMING METALLIC ALLOYS

1.1.1 History of Metallic Glasses

Although glassy solids have been familiar in everyday life for centuries, glassy metals have been virtually unknown. Silicate and other oxide-based glasses are found in diverse applications, from window panes to fiber-optic communication lines. By definition, an amorphous solid lacks long-range atomic order. Amorphous solids can be ordered within small clusters, but atoms in crystalline materials are arranged periodically over lengths much larger than the atomic size. Nearly all metals in common use are composed of grains, each of which is a region with crystalline ordering of its atoms.

Amorphous structures are rarely found in nature because there is always a corresponding crystalline phase or mixture of phases with the same overall composition and a lower free energy. That is, the amorphous state is thermodynamically unstable or metastable. However, there can be kinetic constraints so that the transformation to a crystal is very slow. The more commonly found oxide-based glasses are extremely stable and can be in fact difficult to crystallize. On the other hand, metals and metal alloys are, as a whole, very poor glass formers and crystallize easily.

Qualitatively, the structure of non-crystalline, or amorphous, solids has much in common with that of liquids. The primary difference is that the atoms of liquids are free to move and redistribute themselves on time scales easily measurable in the laboratory. Amorphous solids can still exhibit flow, but on much longer time scales. Thus, the division between amorphous solids and liquids is quite arbitrary, and is often taken to be at a viscosity of 10^{13} poise.[1]

The most distinctive physical property that defines a glassy solid is a glass transition. The glass transition can be detected by the rapid increase of the heat capacity over a small range of temperature. A true second order phase transition would have a discontinuity in heat capacity at a fixed temperature. The glass transition does not meet this criteria since it occurs over a range of temperature, and the onset temperature varies with experimental parameters such as the heating rate as measured in a differential scanning calorimeter (DSC). Because most amorphous metallic alloys also exhibit a glass transition, for simplicity, "amorphous" and "glassy" will be used interchangeably.

Despite their thermodynamic metastability, amorphous metallic alloys can be made by a variety of different processes; techniques now exist which can use gases, liquids, or even crystals as starting material. The first major breakthrough in metallic glass formation came in 1960 when Klement, Willens, and Duwez discovered that $Au_{75}Si_{25}$ could be made amorphous by rapid cooling, or quenching, from the liquid state.[2] The amorphous foil produced by their technique was so unstable, though, that significant crystallization had occurred after only 24 h at ambient temperature. In 1983, Schwarz and Johnson observed the growth of an amorphous layer between two layers of crystalline metals at elevated temperature.[3] Other techniques, such as vapor deposition, electrodeposition, sputtering, plasma spray deposition, and ion implantation, have also been developed to make thin layers or coatings of amorphous metals.

This work will focus on glass-forming techniques which quench material from the molten state. Most metals and metal alloys historically investigated require cooling rates of 10^2 K/s or higher to freeze from the melt to the

metastable amorphous state. The high heat transfer rate required limits these metallic glasses to thin samples produced by such techniques as splat quenching or melt-spinning.[2, 4]

The process of melt spinning has been widely used because of the relative ease with which it can be used to make uniform continuous amorphous ribbons. A schematic of the process is shown in Fig. 1.1. The basic melt-spinning process involves a heated crucible of molten metal of the desired composition. The crucible is usually heated with an induction coil. Applied pressure at the top of the crucible forces a continuous stream of melt through an orifice and onto a rapidly moving chilled substrate, such as a drum, wheel, roller, belt, or between twin rollers.[4] The melt is drawn off and cooled continuously to form the ribbon.

Fig. 1.2 shows a graph of the reduced glass transition temperature, T_{rg}, plotted versus the log of the critical cooling rate, R_c, for a range of traditional glass forming alloys.[5] T_{rg} is the glass transition temperature, T_g, divided by the melting point, T_m; R_c refers to the minimum cooling rate in degrees per second required to cool to the glassy state. As the graph shows, as the reduced glass transition temperature increases, the critical cooling rate required drops precipitously. The critical cooling rates range from 10^2 K/s to 10^{10} K/s, with elemental metals like nickel and tellurium near the highest part of that range. This graph includes the best glass formers when the article was published in 1976.

Bulk metallic glasses are not limited to these standard methods of preparation and thin sample geometries. A "bulk" glass can be defined as one which can be quenched from the melt into a specimen with minimum dimension on the order

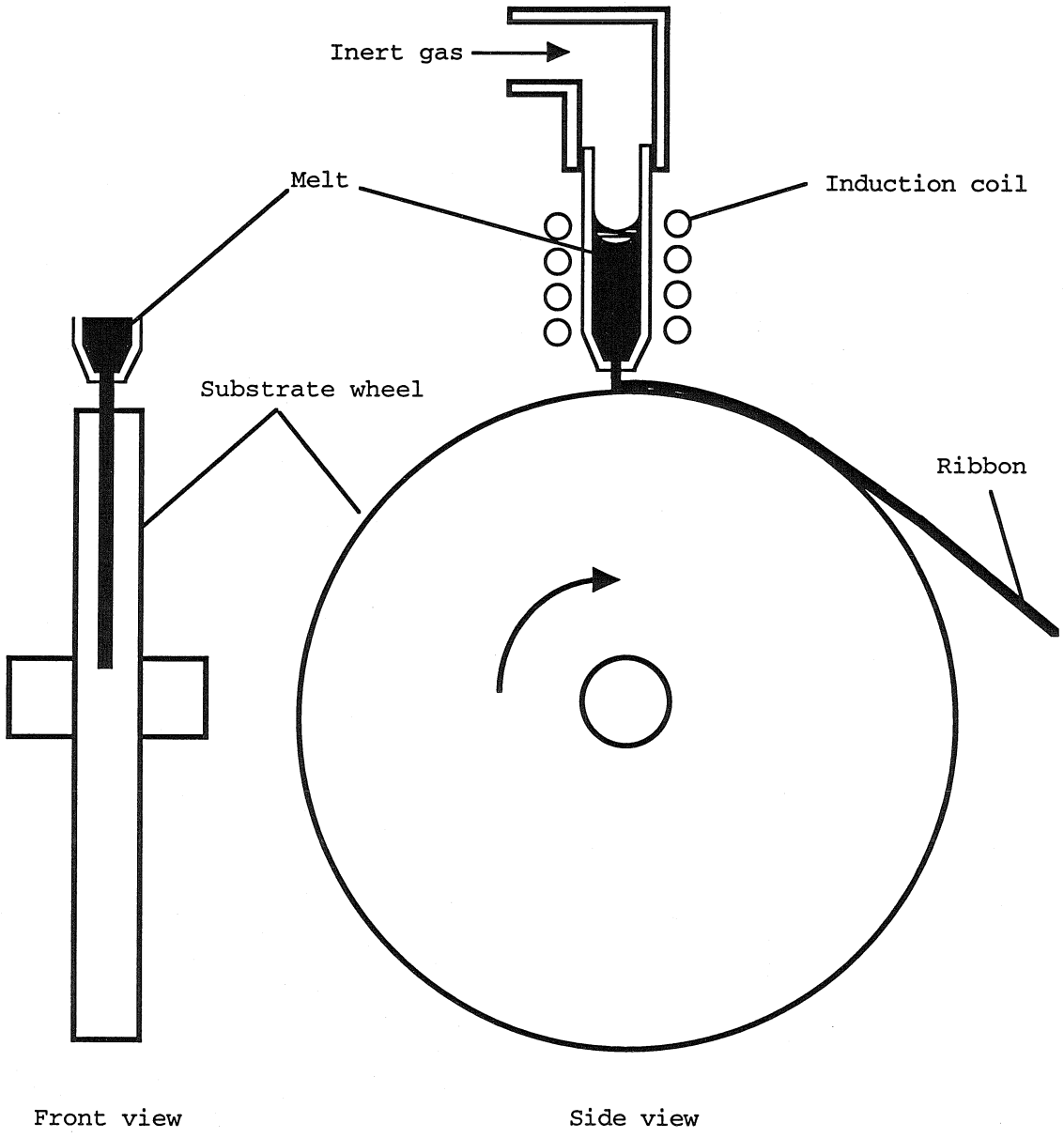

Fig. 1.1. Schematic of melt spinning apparatus. Reproduced from refs. 6 and 7.

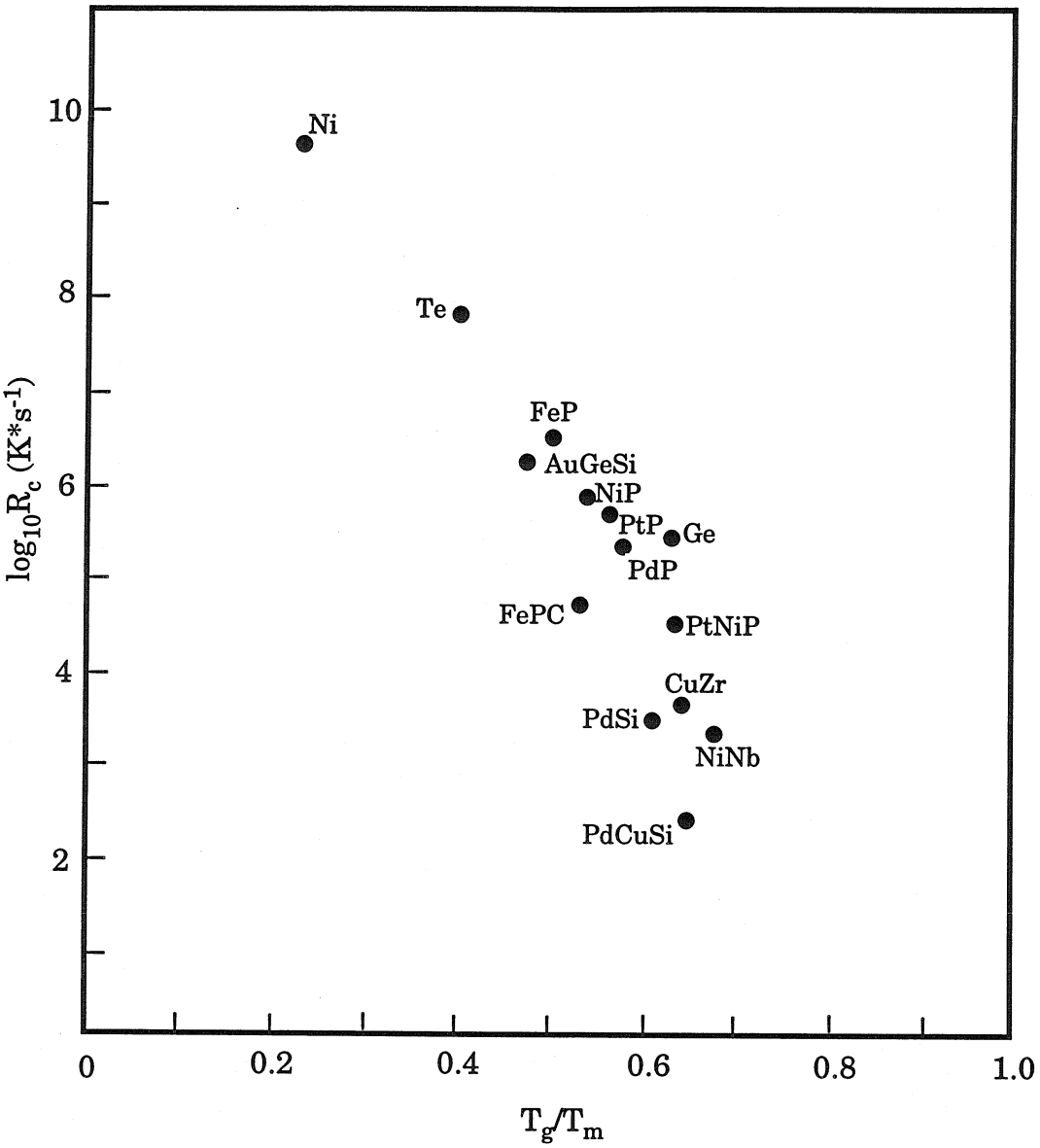

Fig. 1.2. Critical cooling rate, R_c, versus the reduced glass transition temperature, $T_{rg}=T_g/T_m$, for different metals and metallic alloys. Reproduced from ref. 5.

of 1 cm, thus having critical cooling rates of approximately 10^2 K/s or less. Clearly, this definition varies with the quenching technique employed. Chen and Turnbull found in 1969 that amorphous samples of such alloys as Pd-Au-Si could be made up to 1 mm thick by simply dropping the melt onto a metal substrate.[8] In 1982, Drehman, Greer, and Turnbull formed a spheroid of glassy $Pd_{40}Ni_{40}P_{20}$ after etching the surface heterogeneities away and thermally cycling the sample to dissolve any crystalline inclusions. The observed cooling rate for a sample with minor diameter greater than 5 mm was 1.4 K/s; the conclusion was that the critical cooling rate for this specimen was even less than that of Pd-Au-Si. The reported reduced glass transition temperature of $Pd_{40}Ni_{40}P_{20}$ is 0.67.[9]

One of the most highly processible of the bulk metallic glasses is $Zr_{41.2}Ti_{13.8}Cu_{12.5}Ni_{10.0}Be_{22.5}$, trade name Vitreloy™ 1, which has a critical cooling rate of about 1 K/s and a reduced glass transition temperature of 0.67 with no special fluxing procedure required.[10, 11] Rods of this alloy of up to 5 cm in diameter have been cast.[12] In addition to being easily processed, this bulk metallic glass has many superior mechanical properties and shows promise as a new engineering material.[13-15] Further research in the area of alloy development for bulk metallic glasses continues and is yielding new alloy systems and compositions.[16, 17] Nevertheless, $Zr_{41.2}Ti_{13.8}Cu_{12.5}Ni_{10.0}Be_{22.5}$ remains one of the most robust glass-formers and the most easily processed by quenching from the melt. In addition, its physical properties are perhaps the most well characterized of any of the bulk metallic glass alloys. For these reasons, the studies contained in this work exclusively use this alloy.

1.1.2 Scientific and Technological Interest in Metallic Glasses

The interest in metallic glasses has traditionally been driven by scientific curiosity. Investigations of these materials have yielded information about rapid solidification, the nature of the glass transition, metastable phase equilibria, crystallization, and the effects of atomic symmetry on macroscopic properties. Newly developed techniques for synthesizing metallic glass allowed study of a class of material not found in nature.

The many unusual physical, chemical, and mechanical properties of metallic glasses have led to their use in a number of specialized applications. The most widely exploited property of amorphous metals to date is the soft ferromagnetism of certain alloys. The Metglas™ alloys developed by Allied Signal have been used extensively in such applications as transformer cores. Mechanical applications have been rare because of limitation on sample geometry and certain undesirable mechanical properties of amorphous metal ribbons, such as low fatigue life.[18]

Nevertheless, many superior properties of metallic glasses make it an attractive candidate for mechanical applications. The most notable is the extremely high strength. Another is the high elastic strain limit, which is nearly three times that of most crystalline metals. The lack of grain boundaries and the ease with which an amorphous passive oxide layer is formed give many metallic glasses good corrosion resistance.

Since good glass forming alloys are usually found near deep eutectics, these materials can be processed as a liquid at relatively low temperatures, which can reduce manufacturing costs. Moreover, three factors reduce the amount of shrinkage in castings. One, the lower casting temperature lowers the total

amount of thermal contraction upon cooling to room temperature. Two, amorphous alloys usually have low thermal expansion coefficients, and thus contract proportionally less per degree cooled. Three, there is no volume contraction from the liquid-to-solid phase transition in metallic glasses processed by solidification from the melt. These three properties work in conjunction to yield near net shape castings.

Table 1.1 shows a number of selected properties of the amorphous Vitreloy™ 1 in comparison with other metals and alloys commonly used for high strength structural applications.

	Vitreloy™ 1	steel -1080 quenched & tempered	tungsten	Ti-6Al-4V cast	maraging steel-C200
Yield Strength (GPa)	1.93[14]	0.979[19]		0.890[19]	1.4[19]
Elastic Strain Limit (%)	2.0	0.5		0.8	0.7
Young's Modulus (GPa)	93[14]	210[19]	345[19]	114[19]	
Poisson's Ratio	0.387[14]	0.293[19]	0.280[19]	0.361[19]	
Density (g/cc)	6.11[14]	7.84[19]	19.3[20]	4.43[19]	
Coefficient of Thermal Expansion (10^{-6} K^{-1})	10.1	11.6[19] @473 K	4.5[20]	≈9.3[19]	
Thermal Conductivity (W $cm^{-1}K^{-1}$)	0.035	0.381[19] @673 K	1.74[20]		
Melting Point ($T_{liquidus}$, K)	993[10]	1753[19]	3422[20]		

Table 1.1. Selected properties of metallic glass and other comparable engineering materials.

There are a number of promising new applications for metallic glasses, including sporting goods. Vitreloy™ 1 is currently being used to make golf club heads under the name LiquidMetal™. The striking face of the club is designed thinner to take advantage of the large elastic strain limit of the metallic glass. The result is that proportionally more deformation caused by the collision is in the club face rather than the golf ball. The elastic losses in the club are substantially less than those in the ball, so more energy is returned as ball velocity following the impact.

There are, nevertheless, a number of drawbacks to using metallic glass in mechanical applications. One of the major problems is that there is no significant plastic strain before failure. This limits the amount of energy that the material can absorb and dissipate; also, there is no warning before failure. This behavior is called "catastrophic" because of its sudden onset. Another limitation is still the size of the samples produced as determined by the critical cooling rate of the alloy. Although the minimum dimension of a casting which can be made has increased dramatically, it still may be insufficient for many applications. Other drawbacks can be the cost of starting materials, potentially health hazards from constituents such as beryllium, sensitivity to contamination, and lack of manufacturing experience with the alloys.

1.2 CRYSTALLIZATION OF METALLIC GLASSES

As mentioned in the previous section, metallic glass is a thermodynamically metastable or unstable phase. Thus, given the correct conditions, a glass will spontaneously crystallize. However, it is possible to kinetically constrain metastable phases so that the time required for transformation is much longer than is measurable in the laboratory. One excellent example of this phenomenon is diamond. At room temperature and pressure, graphite is the

thermodynamically stable form of carbon, and diamond is metastable. Nevertheless, as far as any new fiancée is concerned, "Diamonds are forever."

1.2.1 Homogeneous Nucleation Theory

One of the most important considerations in determining the feasibility of making a metallic glass composite is that of crystal nucleation and growth. During composite processing, impurity elements which are not constituents of the glass forming alloy may dissolve into the melt, elements already present in the glass may change in concentration, or crystalline debris might act as a heterogeneous nucleation site.

Turnbull et al.[21, 22] developed classical nucleation theory to describe the process of homogeneous nucleation, or nucleation events in the absence of "structural impurities" to catalyze crystallization. Turnbull's work was an extension of that done by Volmer and Webber for the condensation of a vapor.[23] We want to consider the Gibbs free energy of formation, ΔG, for a small aggregate, or embryo, of crystalline material in a liquid. Although ΔG is positive for small crystalline embryos, there is an entropy gain from having them distributed in the liquid; thus there is some equilibrium concentration of these embryos.

There are two terms for this energy ΔG. The first is simply due to the free energy difference between the crystal and the liquid; this is dependent upon the temperature. At temperatures above the melting point, the liquid will have a lower free energy; at temperatures below the melting point, the crystal will have a lower free energy, assuming it is the equilibrium phase. The second term arises from the surface tension between the liquid and the crystal. The surface tension can be thought of as an extra amount of energy needed to

accommodate the mismatch in the atomic arrangements between the two phases. Thus, as the crystal embryo grows, the interfacial area grows and this second term in the energy increases. We can write:

$$\Delta G = \frac{4\pi}{3} r^3 \Delta G_v + 4\pi r^2 \sigma \tag{1.1}$$

where ΔG is the free energy of a crystal embryo of radius r, ΔG_V is the difference in free energy between the crystal and the liquid per unit volume, and σ is the liquid-crystal interfacial energy per unit area. Below the melting point, ΔG_V will be negative and the two terms will compete as r increases, as shown in Fig. 1.3. At small r, the interfacial free energy term will dominate, but for large enough r, the volume term becomes larger and the crystal will grow indefinitely. At this point, the embryo becomes a nucleus. The radius separating these two regimes, the critical radius, r_c, is the point at which the free energy ΔG reaches a maximum. Differentiating Eqn. 1.1 and solving, we find a maximum in free energy at:

$$\Delta G_c = \frac{16\pi\sigma^3}{3(\Delta G_v)^2} \tag{1.2}$$

when

$$r = r_c = -\frac{2\sigma}{\Delta G_v} \tag{1.3}$$

These values represent the nucleation energy barrier and the critical nucleus radius of the crystalline embryo, respectively.

The density of embryos of critical radius follows a Boltzmann distribution:

$$n_c = n_0 e^{-\Delta G_c / kT} \tag{1.4}$$

where n is the number of equilibrium crystalline clusters per unit volume, n_0 is

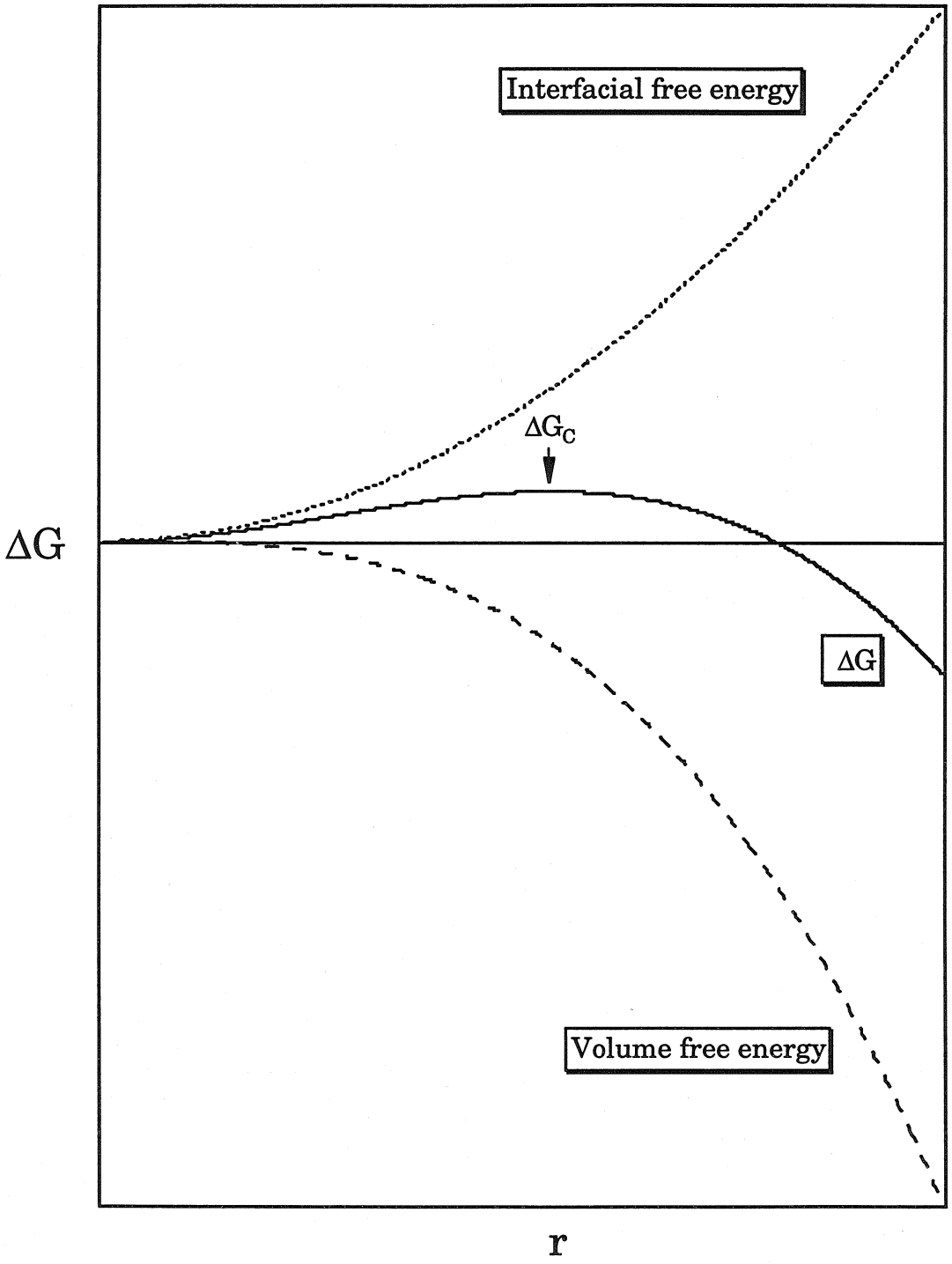

Fig. 1.3. Gibbs free energy ΔG for crystalline embryo as a function of radius.

the number of unassociated molecules per unit volume, k is Boltzmann's constant, and T is the absolute temperature. If we assume that when a crystal grows to the critical nuclei size it is removed from the equilibrium considerations, then the nucleation rate I is governed by the rate at which smaller embryos can grow to the critical size. Then,

$$I = ZS_c n_c \tag{1.5}$$

where Z is the net rate of transfer of atoms from the liquid to the embryo per unit area, S_c is the surface area of a critical nucleus, and n_c is defined by Eqn. 1.4. This becomes:

$$I = K_v \exp\left[-\frac{\Delta G_c + \Delta G_A}{kT}\right] \tag{1.6}$$

where ΔG_A is free energy of activation for transfer of atoms from the liquid to the crystal. K_v is given by:

$$K_v = n^* \left[a\sigma/9\pi kT\right]^{1/2} n\frac{kT}{h} \tag{1.7}$$

where n* is the number of atoms on the surface of a critical nucleus, a is a constant depending on the shape of the nucleus, n is the number of atoms per unit volume of the liquid, and h is Planck's constant.

Turnbull also did an analysis of glass-forming materials, and made the further assumptions that the average jump time of the molecules in the interfacial region is proportional to the viscosity, and that there is no difference in the heat capacity between the liquid and the crystal. This gives:

$$I = \frac{k_n}{\eta}\exp\left[-\frac{b\alpha^3\beta}{T_r(\Delta T_r)^2}\right] \tag{1.8}$$

where k_n is a constant, η is the viscosity, b is a shape constant, $T_r=T/T_m$, $\Delta T_r=(T_m-T)/T_m$, and α and β are dimensionless constants defined by:

$$\alpha = \frac{N^{1/3}V_m^{2/3}\sigma}{L} \tag{1.9}$$

and $$\beta = \frac{L}{RT_m} \tag{1.10}$$

N is Avogadro's number, L is the molar latent heat of melting, V_m is the molar volume of the crystal, and R is the molar gas constant. The viscosity can be modeled by the Vogel-Fulcher relation:

$$\eta = A\exp\left(\frac{B}{T - T_0}\right) \tag{1.11}$$

where A, B, and T_0 are constants.

Eqn. 1.8 shows the two competing forces to homogeneously nucleate crystals in an undercooled melt. When undercooling is small, there is little thermodynamic driving force to crystallize. ΔT is small, and the exponential term keeps the nucleation rate low. As the undercooling increases, the nucleation rate increases until the increasing viscosity begins to dominate. Physically, the mobility of atoms is drastically reduced, making crystallization more difficult. Thus, it is over the range in temperature below the melting point and above the glass transition temperature that crystallization of a glass-former is possible. This is frequently stated in terms of the reduced glass transition temperature T_{rg}, which is T_g/T_m. Turnbull notes that there is a strong dependence upon T_{rg} for glass-forming ability; as T_{rg} increases to approach 2/3, it becomes quite easy to cool the material to a glass, provided that only homogeneous nucleation is considered.

1.2.2 Heterogeneous Nucleation Theory

In practice, very rarely is a melt totally homogeneous; there can be free surfaces, internal surfaces, container walls, or suspended crystals which can catalyze crystallization by acting as heterogeneous nucleation sites. It is

extremely difficult to eliminate all of these effects in an experiment, so heterogeneous nucleation often dominates homogeneous nucleation in physical experiments.

Heterogeneous nucleation can be thought of as a crystalline embryo in a supercooled liquid growing on an impurity crystal. The shape of the embryo will approximate a sphere in order to minimize the surface area per unit volume between the embryo and the liquid; it can take the form of a spherical cap. This is shown schematically in Fig. 1.4. Assuming that the interface is stable and in equilibrium, the forces from the surface tensions balance where the three interfaces meet:[22]

$$\sigma_{SL} = \sigma_{SC} + \sigma_{LC}\cos\theta \tag{1.12}$$

where C refers to the crystal embryo, L to the liquid, S to the catalytic substrate, and θ is the angle of contact between the crystalline embryo and the substrate, also known as the wetting angle.

Clearly, there are only certain conditions for which Eqn. 1.12 is satisfied. In particular, since $-1 \geq \cos\theta \leq 1$, the parameter m is defined as :

$$m = \frac{\sigma_{SL} - \sigma_{SC}}{\sigma_{LC}} \tag{1.13}$$

For a stable interface, the condition $-1 \leq m \leq 1$ must be met. If $m < -1$, then no contact occurs; it is a lower energy state for the crystalline embryo to be completely within the liquid. This then degenerates to the case of homogeneous nucleation. If $m > 1$, then there is complete contact; there is a driving force for the crystal to spread completely across the surface of the substrate. A spherical cap forms for wetting angle between 0° and 90°; that is, $0 < m \leq 1$.

For a spherical cap, the volume is given by (see Fig. 1.5)[24]:

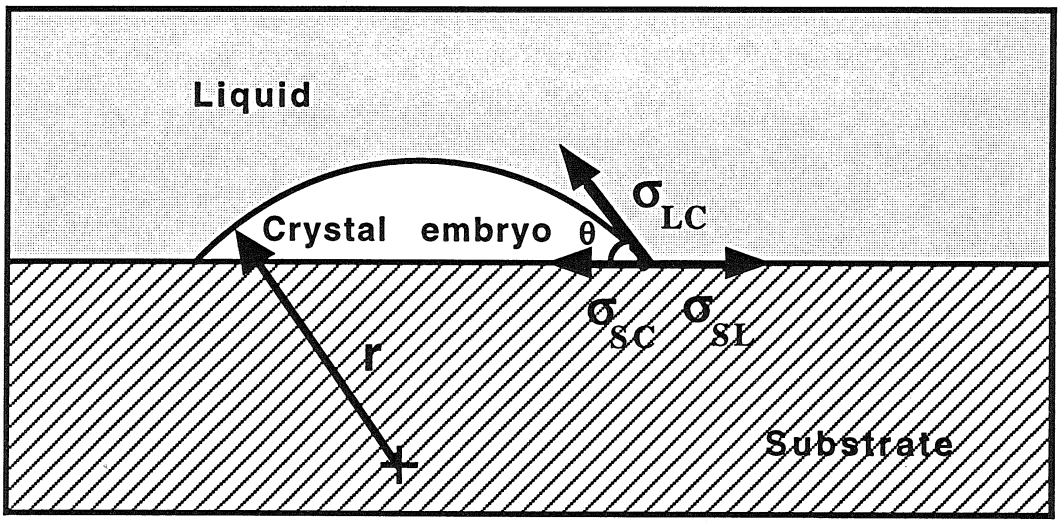

Fig. 1.4. Schematic of a spherical-cap-shaped crystalline embryo forming in a supercooled liquid on a catalytic substrate. Reproduced from ref. 24.

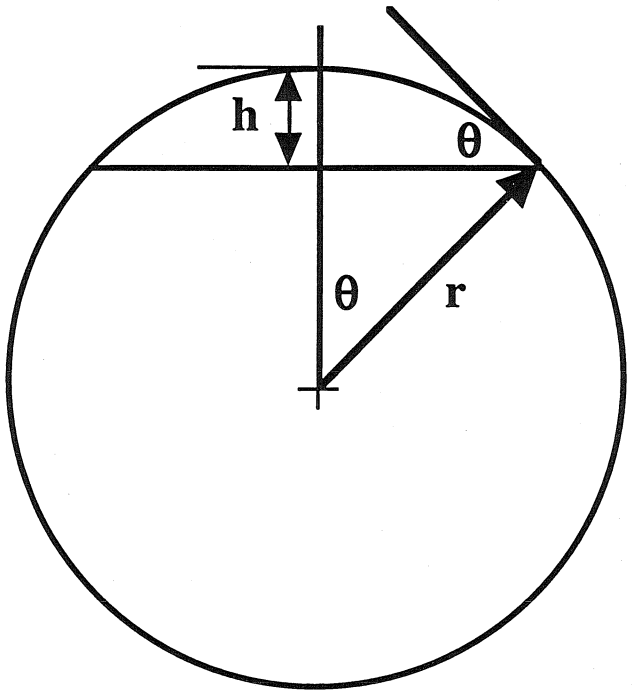

Fig. 1.5. Spherical cap geometry.

$$\begin{aligned} V_c &= \tfrac{1}{3}\pi h^2(3r-h) \\ &= \tfrac{1}{3}\pi(r-r\cos\theta)^2[3r-(r-r\cos\theta)] \\ &= \tfrac{1}{3}\pi(1-\cos\theta)^2[2+\cos\theta]r^3 \end{aligned} \tag{1.14}$$

and the surface area representing the interface between the liquid and the embryo is:

$$A_c = 2\pi(1-\cos\theta)r^2 \tag{1.15}$$

The Gibbs free energy change associated with the formation of a spherical cap-shaped crystalline embryo on a substrate is given by:

$$\begin{aligned} \Delta G_{hetero} = {} & 2\pi(1-\cos\theta)r^2\sigma_{LC} + \pi(r\sin\theta)^2(\sigma_{SC}-\sigma_{SL}) \\ & + \tfrac{\pi}{3}(1-\cos\theta)^2(2+\cos\theta)r^3\Delta G_v \end{aligned} \tag{1.16}$$

The first term represents the new interfacial energy between the liquid and the crystalline embryo, the second term is the energy associated with replacing the interface between substrate and liquid by one between substrate and crystal, and the third term is the energy of converting the volume of liquid to crystal. This can be simplified using Eqn. 1.12 and our result from homogeneous nucleation theory (Eqn. 1.1):

$$\begin{aligned} \Delta G_{hetero} &= \frac{(1-\cos\theta)^2(2+\cos\theta)}{4}\Delta G \\ &\equiv f(\theta)\cdot\Delta G \end{aligned} \tag{1.17}$$

recalling that ΔG is the energy change for an embryo according to homogeneous nucleation theory. Differentiating with respect to r, we find that ΔG_{hetero} has a maximum at the same point as ΔG. Thus, the radius of a critical nucleus is the same for heterogeneous and for homogeneous nucleation, but the energy of formation is reduced by the factor f(θ).

Referring back to Eqn. 1.6 and the theory of homogeneous nucleation, we see that since this factor of f(θ) is between 0 and 1, it increases the rate of heterogeneous nucleation as given by:

$$I_{hetero} = K_v \exp\left[-\frac{\Delta G_A}{kT}\right]\exp\left[-\frac{f(\theta)\Delta G_c}{kT}\right] \qquad (1.18)$$

1.3 COMPOSITE THEORY AND TRADITIONAL COMPOSITE SYSTEMS

1.3.1 Classification and Types of Composites

A composite can be defined as having a heterogeneous structure composed of two or more distinct components which are bonded together to achieve a definite goal for a specific purpose.[25] Composite materials have been in frequent use for many centuries and often provide better properties than any of the constituent materials would alone. Brick made from mud and straw, plywood, and reinforced concrete are all composites engineered to give certain properties. Extensive research continues to give new types of composites, better processing techniques for fabrication, and improved characterization of existing materials.

Although certain high-performance composites can have many superior properties, no single material will have all of the best properties. Some of the most common properties desired are strength, fracture toughness, ductility, fatigue resistance, oxidation resistance, and low cost. There are inevitable trade-offs, so the material must be chosen to have the best characteristics for the most important properties, and minimal degradation of the others.

One way to categorize different high performance composites is based on the matrix material used. There are three basic matrices: polymer, ceramic, and metal; reinforcements are used from all three of these classes as well. Composite materials can also be divided into five different groups depending upon the geometry of the reinforcement phase: particles, fibers, flakes, skeletal, and laminar. Particulate reinforced composites are usually reinforced with a discontinuous, roughly spherical second phase giving an isotropic final material. Fibers can vary widely in size and aspect ratio, in addition to being either randomly oriented or aligned. Flakes would be considered discontinuous reinforcements with one dimension significantly less than the other two. Skeletal composites are composed of a continuous porous matrix which is then filled by a second material. Since both the starting material and the filling material are continuous, it is unclear which to consider the matrix and which the reinforcement. Layers of different materials can be stacked one on top of another to make a laminar composite.[26]

Combinations of these different reinforcement geometries are possible as well. Fiber reinforced composites can use short fibers to yield an isotropic material, aligned short fibers, uniaxially aligned continuous fibers, or fibers woven in two dimensions to give sheets, which can then be stacked and made into a laminar composite. No one configuration is ideal for all applications; the requirements of a given task must be considered in determining both the materials and the reinforcement geometry to use.

Techniques of fabrication of composites can also vary widely. For metal matrix composites, three basic techniques exist: powder metallurgy, ingot metallurgy, and mechanical alloying. Powder metallurgy begins with the matrix in powder form; it is then incorporated with the reinforcement, and then

consolidated in some fashion at elevated temperature and pressure. The consolidated composite can then be shaped by either extrusion or forging. Ingot metallurgy involves mixing the reinforcement with the molten matrix; this mixture can then be cast directly. Also, vacuum infiltration can be used to make metal-matrix composites. In this technique, the reinforcing fibers are placed in a die, a vacuum is applied to one end, and molten matrix is supplied at the other. The vacuum draws the matrix into the mold and infiltrates the reinforcement simultaneously. Finally, the mechanical alloying technique can be used to form an alloy matrix with discontinuous reinforcement starting with the elemental metal powders and the reinforcement. These are all mechanically alloyed in an apparatus such as a high energy ball mill. The powder from this procedure can then be consolidated in a similar fashion as in the powder metallurgy approach.[27]

There are also numerous types of processing techniques for other types of composites. The most pertinent one to this study is injection molding, which is primarily used with thermoplastic matrix materials. In this technique, the polymer is heated, the softened polymer is forced into a cooled mold by a high pressure ram, and the part is allowed to cool and ejected from the mold. Die casting is a similar process used for making metal parts. Typically, since metal is involved, a higher temperature is required for die casting, and die casting is rarely used for processing composites.

1.3.2 Role of the Composite Interface

The work presented in this thesis will focus primarily on reinforcement with continuous uniaxially aligned fiber and wire reinforcements. Thus the

background discussion will focus on these types of composites in traditional systems.

There are a number of advantages given to a composite material by the reinforcement by fibers. The properties of interest are usually the ones which the matrix material is most clearly lacking for a given application. For example, graphite-fiber-reinforced epoxy is a commonly used composite system because the graphite fibers increase the epoxy's poor strength and modulus. Conversely, ceramic and other brittle matrix composites are often designed to improve other properties such as fracture toughness and strain-to-failure of the matrix, since strength and modulus are generally properties which need little improvement.

As discussed previously, toughness and strain-to-failure are properties which would be beneficial to improve in metallic glasses; in brittle matrix composite systems, these properties can be imparted by crack bridging by the fibers. An essential component of this mechanism is control of the interface properties. When a composite is loaded and reaches a stress at which a crack begins to propagate through the matrix, the interface between the matrix and the fiber can serve to lower the stress intensity experienced by the fiber and allow the matrix crack to bypass it. Instead of the matrix crack continuing directly through the fiber, a debonding crack is propagated along the interface. (See Fig. 1.6.) The condition for this to occur has been calculated to be that the ratio of interface fracture energy to fiber fracture energy is less than ~1/4.[28] If this condition is not met, the interface can still transfer enough stress to crack the fibers, rather than fail itself.

The toughening effect arises from the pull-out of fibers from the matrix. Most theories of composite toughening include an initial debonding shear stress

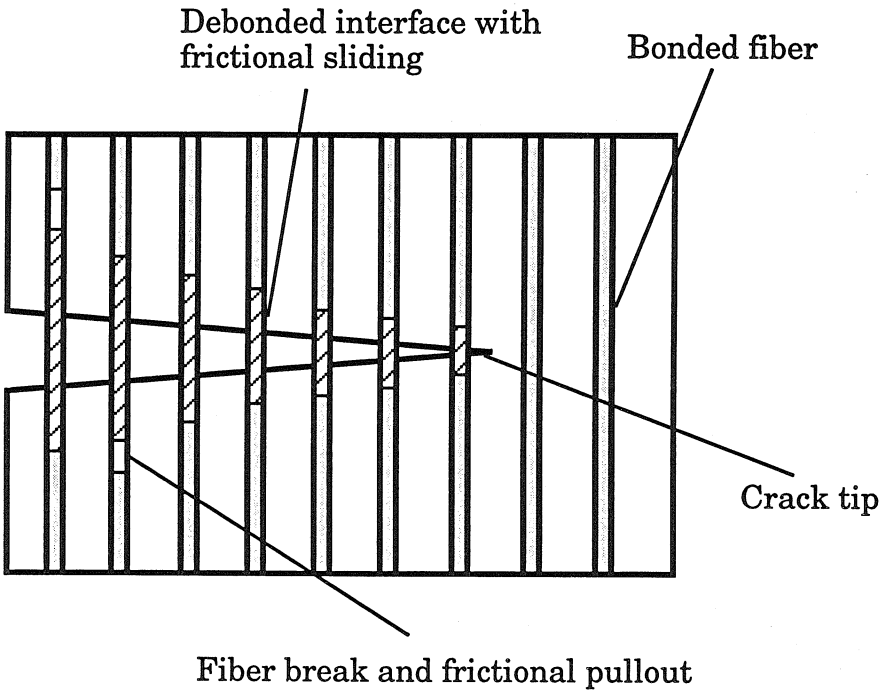

Fig. 1.6. Schematic of crack bridging and fiber pull out in a brittle-matrix brittle-fiber composite. Reproduced from ref. 30.

as well as a frictional sliding stress for the debonded fibers. Most of the energy absorption comes from the work done in opposing this frictional force. In addition to this mechanism, toughening can be accomplished by the work done of plastic deformation of ductile fibers or wires. (See Fig. 1.7.)

The technique of fabrication of the composite is important in determining its final properties. One reason for this is that processing can drastically affect the interface between the matrix and the reinforcement. The desired properties of the interface depend on the type of composite system; systems can be classified as having either a brittle or ductile matrix. In ductile matrix systems, fiber failure precedes matrix failure, and in a brittle matrix system, matrix cracking occurs before or simultaneously with fiber failure. Similarly, the interface between matrix and fiber can be characterized as either "strong" or "weak."[29] As discussed above, the interface must be sufficiently weak to blunt the crack and encourage fiber pull out, but strong enough to transfer the load effectively from the matrix to the fibers.

1.4 METALLIC GLASS AND COMPOSITES

Because of its high strength and high strain limit, metallic glass is a natural candidate for use as a reinforcement in composite materials. There have been a number of attempts to produce composites with amorphous ribbon reinforcements. Strife and Prewo[31] fabricated and mechanically tested an amorphous-metal-ribbon-reinforced resin-matrix composite. It was found to have high strength, both longitudinally and transversely, and good fracture toughness. However, it was not competitive in specific modulus and fatigue resistance with other resin-matrix composites. As a result, they concluded it would not be suitable to replace most other high performance composites.

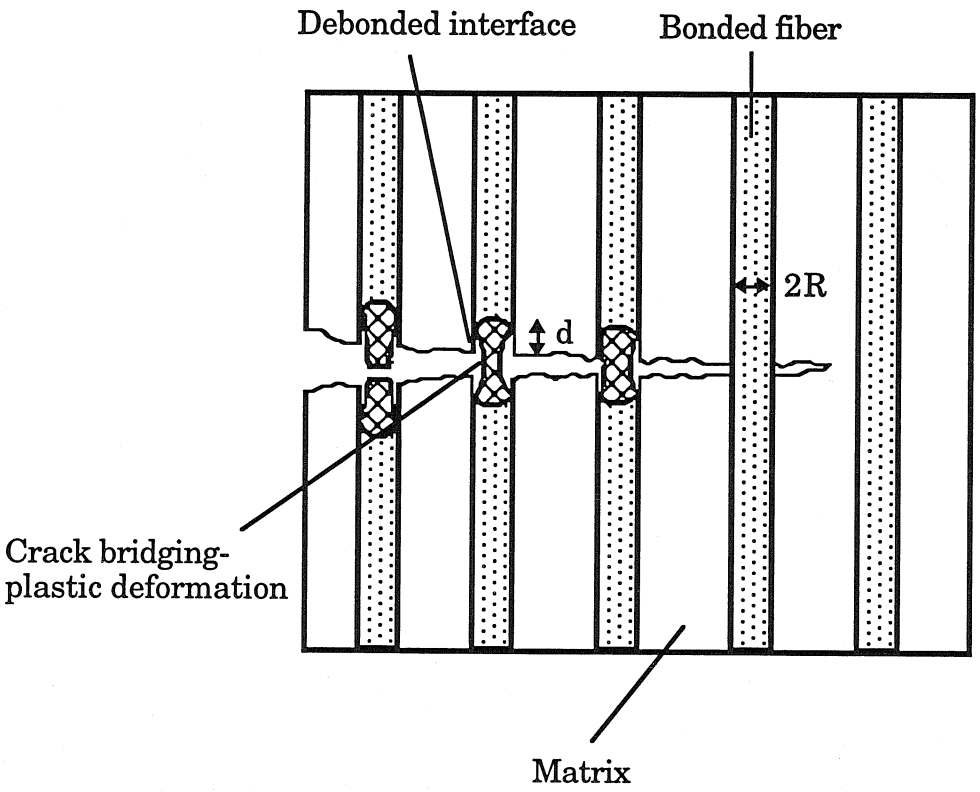

Fig. 1.7. Schematic of toughening mechanisms in a brittle-matrix ductile-fiber composite. d is the debond length, and R is the radius of the fiber. Reproduced from ref. 29.

Nevertheless, a number of other studies have investigated the properties of polymer and glass ceramic matrices reinforced by amorphous metal ribbons.[32-35]

There are a number of clear processing advantages in making a composite material with a metallic glass matrix. One is that since the metallic glass-forming alloys usually are at deep eutectic compositions[36], they have low melting points, considerably lower that those of their constitutive elements. Accordingly, these alloys can be used in liquid-phase processing at lower temperatures; this lowers the cost of processing, decreases the need for specialized equipment, and reduces the interfacial reaction rate between matrix and reinforcement. Further, there is more potential flexibility in processing since many of the good glass forming alloys are stable against crystallization above their glass transition temperature as an undercooled liquid. This characteristic allows for the possibility of processing at even lower temperatures slightly above the glass transition, although higher pressures would be required due to the higher viscosity. Also, upon cooling from a liquid to a glass, good glass forming alloys have minimal shrinkage, as previously discussed. This results in a composite with near net shape, as well as lower differential thermal stresses between the metallic glass and reinforcement.

The past work performed on metallic glass matrix composites is reviewed in the beginning of Chapter 2, which describes the technique developed for processing a bulk metallic glass matrix composite.

REFERENCES

1. T. R. Anantharaman, in *Metallic Glasses: Production, Properties, and Applications* (edited by T. R. Anantharaman), Transtec, Switzerland (1984).

2. W. Klement IV, R. H. Willens and P. Duwez, *Nature* **187**, 869-870 (1960).

3. R. B. Schwarz and W. L. Johnson, *Phys. Rev. Lett* **51**, 5, 415-418 (1983).

4. H. H. Liebermann, in *Amorphous Metallic Alloys* (edited by F. E. Luborsky), 26-41, Butterworths, London (1983).

5. H. A. Davies, *Phys. Chem. Glasses* **17**, 5, 159-173 (1976).

6. X. Lin, Bulk Glass Formation and Crystallization of Zr-Ti Based Alloys, Ph.D. thesis, California Institute of Technology (1997).

7. R. W. Cahn, in *Physical Metallurgy* (edited by R. W. Cahn and Haasen), , 1779, North-Holland Physics Publishing, Amsterdam (1983).

8. H. S. Chen and D. Turnbull, *Acta Metall.* **17**, 1021 (1969).

9. A. J. Drehman, A. L. Greer and D. Turnbull, *Appl. Phys. Lett.* **41**, 8, 716-717 (1982).

10. A. Peker and W. L. Johnson, *Appl. Phys. Lett.* **63**, 17, 2342-2344 (1993).

11. Y. J. Kim, R. Busch, W. L. Johnson, A. J. Rulison and W. K. Rhim, *Appl. Phys. Lett.* **68**, 8, 1057-1059 (1996).

12. W. L. Johnson, *Curr. Opinion in Solid State & Mater. Sci.* **1**, 3, 383-386 (1996).

13. W. L. Johnson, *Materials Science Forum Proc. ISMANAM-95* (edited by Robert Schultz), **225-227**, 35-50, Transtec, Switzerland (1996).

14. H. A. Bruck, T. Christman, A. J. Rosakis and W. L. Johnson, *Scripta Metall. Mater.* **30**, 4, 429-434 (1994).

15. H. A. Bruck, A. J. Rosakis and W. L. Johnson, *J. Mater. Res.* **11**, 2, 503-511 (1996).

16. T. Zhang, A. Inoue and T. Masumoto, *Mater. Trans. JIM* **32**, 11, 1005 (1991).

17. X. Lin and W. L. Johnson, *J. Appl. Phys.* **78**, 11, 6514-6519 (1995).

18. D. Raskin and C. H. Smith, in *Amorphous Metallic Alloys* (edited by F. E. Luborsky), 381-400, Butterworths, London (1983).

19. *Metals Handbook*, American Society for Metals, Metals Park, OH (1985).

20. *Handbook of Chemistry and Physics*, CRC Press, Boca Raton (1991).

21. D. Turnbull, *Solid State Physics* (edited by F. Seitz and D. Turnbull), 226-306, Academic Press, New York (1956).

22. J. H. Hollomon and D. Turnbull, *Prog Metal Phys* **4**, 333-388 (1953).

23. M. Volmer and A. Webber, *Z Phys Chem* **119**, 277 (1925).

24. B. Chalmers, *Principles of Solidification*, Wiley & Sons, New York (1964).

25. K. G. Kreider, *Composite Materials: 4* , 1, Academic Press, New York, (1974).

26. *Composite Materials Handbook*, McGraw-Hill, New York (1984).

27. T. S. Srivatsan, T. S. Sudarshan and E. J. Lavernia, *Prog. Mater. Sci.* **39**, 317-409 (1995).

28. M. Y. He and J. W. Hutchinson, *Int. J. Solids Struct.* **25**, 1053 (1989).

29. A. G. Evans, *Mater. Sci. Eng. A* **143**, 63-76 (1991).

30. J. W. Hutchinson and H. M. Jensen, *Mech. mater.* **9**, 139-163 (1990).

31. J. R. Strife and K. M. Prewo, *J. Mater. Sci.* **17**, 359-368 (1982).

32. R. U. Vaidya and K. N. Subramanian, *J Mater Sci L* **9**, 12, 1397-1399 (1990).

33. R. U. Vaidya, C. Norris and K. N. Subramanian, *J. Mater. Sci.* **27**, 18, 4957-4960 (1992).

34. R. U. Vaidya and K. N. Subramanian, *J. Mater. Sci.* **26**, 23, 6453-6457 (1991).

35. R. U. Vaidya, K. K. Chawla and K. N. Subramanian, *J. Mater. Sci.* **29**, 7, 1719-1723 (1994).

36. H. A. Davies, in *Amorphous Metallic Alloys* (edited by F. E. Luborsky), 8-25, Butterworths, London (1983).

CHAPTER 2
PROCESSING A BULK-METALLIC-GLASS MATRIX COMPOSITE BY MELT INFILTRATION CASTING

2.1 TRADITIONAL PROCESSING OF METAL MATRIX COMPOSITES

A number of techniques are currently used for the fabrication of metal matrix composites. The type of matrix, reinforcement, and target application will all influence the technique for processing the material. Reinforcement size and morphology are influential parameters in determining which fabrication processes are possible and practical. Processing must consolidate and bond the reinforcement and matrix in the desired configuration without excessive reaction between the two, which can degrade the overall properties of the composite.

Fig. 2.1 shows a number of different processing techniques for the fabrication of metal-matrix composites. Processing can be divided up into two stages: primary, for incorporation of the reinforcement into the matrix, and secondary, which may be required for consolidation, shaping, or fiber alignment. Some primary processing techniques may provide satisfactory properties upon incorporation and not require secondary processing.

Processing techniques which are most applicable to the composite system studied in this work will be emphasized. For this reason, traditional secondary processing techniques will not be examined in depth.

2.1.1 Liquid-Matrix Primary Processing

There are a number of techniques for composite fabrication in which the reinforcement is initially incorporated with a molten matrix. This type of

Processing of Metal Matrix Composites

Primary

Liquid (melt) Processing	Non-Liquid (solid) Processing	Reactive Processing
• Incorporation during forming - *Die Casting* - *Squeeze Casting / Infiltration* - *Melt Atomization (Osprey Deposition Process)* - *Thermal Spray* • Incorporation before forming - *Slurry casting* - *Semi-solid (rheocasting and compocasting)*	*Powder Blending* - wet or dry - followed by secondary compaction stage *Stacked Laminates* - primarily used with foils - bonded during consolidation *Physical Vapor Deposition (PVD)*	*Directional Solidification* *Exothermic Reaction*

Secondary

- *extrusion / drawing*
- *forging*
- *rolling*
- *Hot Isostatic Pressing (HIPing)*
- *High energy, high rate processing*
- *Superplastic forming*
- *dynamic powder compaction (shock wave consolidation)*

Fig. 2.1. Different processing techniques for fabricating metal matrix composites.

processing is advantageous because this usually results in a strong bond and intimate contact between matrix and reinforcement. Its primary drawback is that the rate of chemical reaction at temperatures required to keep the matrix molten is high; excessive reaction can lead to a brittle interfacial layer, degradation of the reinforcement, and contamination of the matrix. Due to the high reaction rates, this type of processing often requires that infiltration be accomplished in relatively short times and at high pressures.

One example of liquid-matrix primary processing is casting, which involves forcing molten material into a mold with back pressure, often supplied by a hydraulic ram. During squeeze casting, infiltration is usually done more slowly and at higher pressures than die casting, and typically the ram continues to move during solidification. This continuing movement during solidification refines the microstructure by deforming the growing dendritic array and compensates for the freezing contraction by continuing to feed in new material.[1] This technique can be used to make metal matrix composites either by casting a mixture of molten matrix and reinforcement, or by forcing the matrix into a reinforcement array, such as a fiber preform. This technique has the capability to yield low porosity and near net shape pieces; there is usually little need for any secondary processing. Die casting can provide a smaller grained microstructure due to higher cooling rates, but there can be problems with porosity and achieving complete infiltration.

Melt atomization creates bulk material by blowing drops of molten metal onto a substrate. The metal is melted in a furnace, released in a stream, and atomized by a jet of cold gas. This process was developed in the late 1970s and 1980s by Osprey Ltd., and has become know as the Osprey process. Feed rates of molten material in the range of kilograms per second are possible with

this process. This can be used to make metal matrix composites by introducing a stream of reinforcement particles along with the atomized metal. This allows minimal contact time and interfacial reaction between the melt and the reinforcement. It is an economical process because it makes little waste material, and use of an inert gas jet results in minimal oxide contamination. One drawback of this process is that in practice the volume fraction of reinforcement is limited to about 25 percent. Other disadvantages of this technique are frequent inhomogeneities in reinforcement distribution and significant porosity. Further consolidation through secondary processing is usually required.[1, 2]

Thermal spray techniques are similar to melt atomization because they also use flowing gas to project molten drops of material towards a cool substrate. However, the thermal spray techniques melt the material by introducing it, either in powder or wire form, into a combustion flame or plasma arc. Like the Osprey process, thermal spray deposition can be used to make metal matrix composites by introducing a stream of reinforcement particles along with the matrix material. This family of processes usually results in lower deposition rates than melt atomization, on the order of grams per second. Drop velocities are usually higher, so quench rates can be 10^4 degrees per second, fast enough to be considered rapid solidification. In fact, this technique is very similar to the gun quenching technique used by Duwez to rapidly quench $Au_{75}Si_{25}$ and make the first metallic glass.[3] In addition, porosities from samples made with this technique can be below 1%.

Composites can also be fabricated using techniques which mix the reinforcement together with the molten matrix prior to forming. Slurry casting is perhaps the simplest method of making composites; the reinforcement is

added to the molten matrix, and the mixture is cast and allowed to cool. The advantage of this technique is mainly its simplicity: no specialized equipment is required, and it can be easily adapted to continuous processing. Also, there is sufficient contact time for good wetting to occur. There are three primary problems with this technique: difficulty in casting, inhomogeneities, and excessive interfacial reactions. When solid particles or short fibers are added to the melt, the viscosity increases dramatically, and thus flow of the mixture becomes restricted. This can be ameliorated by agitating or stirring the melt to keep the particles in suspension. Semi-solid casting involves similar processing, but the melt is allowed to partially solidify during agitation. This process, known as rheocasting, encourages formation of spherical crystals rather than dendrites in the matrix, and keeps the viscosity low. The stirring also prevents settling and agglomeration of the particles. With the introduction of ceramic particles to the melt, the process has been called compocasting.[1, 2]

2.1.2 Solid-Matrix Primary Processing

There are also a number of techniques suitable for making metal matrix composites by avoiding having the matrix in the liquid state. The most common form of solid primary processing is mixing the reinforcement together with the matrix in powder form. With this technique, the secondary processing to compact and bond the powder together is essential. The powder can be dry or suspended in a fluid. When the powder is a suspension, the compaction steps also serve to evaporate and remove the liquid carrier. This process is a good one for making composites with all ranges of matrix to reinforcement ratios. It can be difficult to achieve homogeneous reinforcement distribution,

though, particularly with short fibers or whiskers, which tend to clump and tangle.[1]

The initial form of the matrix can also be thin foils instead of powders. Stacking these foils of matrix material alternately with fibers or another form of reinforcement is the primary step; then, compacting this layered structure at elevated temperature allows plastic flow of the foil material around the reinforcement. The different components are joined by diffusion bonding, since the temperatures used are generally below the melting point of the matrix. This is a good process for making continuous fiber composites, and interfacial reactions can be better controlled because of the lower temperatures than would be required for liquid-phase processing. Still, the stacking process can be cumbersome and slow; it is also difficult to make samples with high reinforcement fractions and good fiber distribution. Also, only certain metals, such as titanium, which can dissolve their own oxides at processing temperatures are well-suited to diffusion bonding. Otherwise, the native oxide layer can create problems in joining the foil layers together.[1]

Physical vapor deposition (PVD) can also be used to join reinforcement and matrix, and is neither truly liquid nor solid matrix processing. This is usually done with monofilament reinforcements; the matrix material is deposited, often by evaporation, directly onto a single wire. The wire is then bundled up and suitably arranged, and compacted with a secondary technique such as hot isostatic pressing. This technique provides good control of fiber volume fraction through control of the layer thickness, and allows a wide variety of matrix compositions to be used.[1]

2.1.3 Reactive Primary Processing

Composites need not be made as two distinct phases mixed together; they can also be made by inducing some sort of reaction, driven by either chemical or mechanical energy, in a monolithic material to form multiple phases. Directionally solidified eutectics have a lamellar-type structure of two different phases. Materials can be engineered so that at some elevated temperature, a spontaneous reaction occurs which produces a second phase such as a ceramic or an oxide which acts as a reinforcement.

2.2 PROCESSING OF METALLIC GLASS COMPOSITES BY RAPID QUENCHING

Metal-matrix composites reinforced by metallic glass have also been investigated, as reported by Cytron.[4] The investigator vacuum hot-pressed amorphous $Ni_{60}Nb_{40}$ ribbons sandwiched between two disks of superplastic aluminum. The materials were chosen so that the aluminum disks could be heated to their superplastic zone below the crystallization temperature of the amorphous ribbons. Good bonding was achieved between the reinforcement and the matrix, and the possibility of using such a technique for making this type of composite was supported.

Amorphous metallic alloys have also been frequently used as a matrix for particulate reinforced composites, and to a lesser extent for fiber reinforced composites as well. Usually the melt spinning technique is used to make composites in ribbon form. This was the subject of a number of U.S. patents filed in the early 1980s. Narasimham of Allied Corporation patented the technique of incorporating particulate matter into the melt, and then quenching the mixture by melt spinning.[5] Kimura, Cunningham, and Ast first

reported mechanical tests and microstructural characterization of such a composite.[6] They added tungsten carbide particles to $Ni_{78}Si_{10}B_{12}$ during the melt-spinning process. Ast later patented the technique of blowing particles into the melt between the crucible and the chilled roller, claiming that this improvement allowed better particle distribution while minimizing contact time and chemical reaction between the particles and the melt.[7] This technique has also been used to make amorphous metal ribbons reinforced with discontinuous fibers, although the resulting fiber distribution was poor; most of the fibers were incorporated on the ribbon surfaces, probably due to poor wetting between the fiber and the melt.[8]

In addition to being used to fabricate particulate reinforced metallic glass ribbons, melt-spinning process has been used to make continuous lengths of fiber reinforced composites, as described in a patent filed in 1972 by Williford and Pilger.[9] The inventors described introducing an arrangement of fibers into contact with the meniscus of molten metal protruding from the crucible orifice. The fibers were then drawn out along with the melt onto the moving substrate; the combination was chilled to form the composite. Composites of this type were made successfully, but the best results were ribbons reinforced by one or two tungsten wires.[8, 10] A schematic of the apparatus used by Nussbaum and Ast is shown in Fig. 2.2. Two pulleys are used, one to feed the wire to the melt-spinning apparatus, the other to take up the composite at the other end. The feed pulley (the "Rear pulley" in Fig. 2.2) was also fitted with aerodynamic drag vanes, which were used in conjunction with a nitrogen jet to regulate the tension. The front pulley was controlled by a variable speed electric motor taken from a Dremel tool.

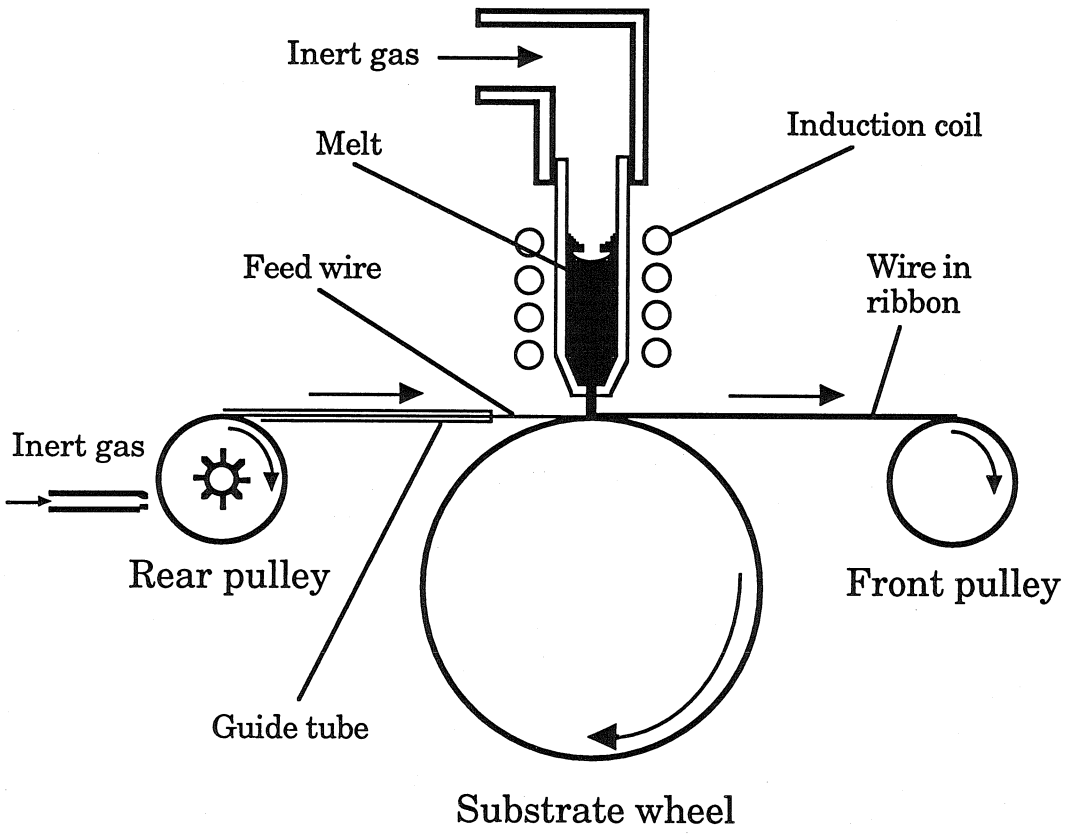

Fig. 2.2. Schematic of modified melt-spinner to make continuous-wire reinforced amorphous ribbons. Reproduced from ref. 10.

2.3 EXPERIMENTAL

This section describes a technique for successfully using a bulk glass-forming alloy as a matrix material for composites. We used exclusively the alloy $Zr_{41.2}Ti_{13.8}Cu_{12.5}Ni_{10.0}Be_{22.5}$ (trade name Vitreloy™ 1) developed by Peker and Johnson[11] as the matrix material. The low critical cooling rate of this alloy allows amorphous metal matrix composites to be made in bulk form. First, ingots of this alloy were prepared by melting together the constitutive elements in an induction furnace under a titanium-gettered argon atmosphere. The starting metals were high-purity (99.5% metals basis or better) research grade material. The metals were alloyed on a copper "boat," which is a 2 cm diameter copper tube with large indentations on one side. The sample sits atop the tube in the indentations and can then be inserted into a horizontal induction coil. The copper boat is cooled with a constant water flow inside the tube to prevent it from alloying with the sample. Because the cooling rate provided by contact with the copper boat is sufficiently high, ingots produced by this technique are mostly amorphous.

Composites were fabricated with a wide variety of reinforcements using the technique described below. Continuous ceramic fibers, such as silicon carbide and carbon, and continuous metal wires, such as tungsten, carbon steel, stainless steel, molybdenum, tantalum, nickel, copper, and titanium, were used as reinforcement. Particulate reinforced composites were made with both loose tungsten particles and sintered silicon carbide (SiC) particulate preforms. The preform was provided by the Carborundum Company.

The reinforcements used in the majority of samples were 254 μm diameter tungsten wire or 254 μm diameter high-carbon (1080) steel music wire. The tungsten wire was obtained from Thermionics Products Company (North

Plainfield, NJ). Both types of wire were straightened and cut into 5 cm lengths. To avoid clustering of wires and to ensure good distribution, the wires were bowed slightly in samples with lower fiber fractions. The tungsten wire was degreased by ultrasonic cleaning in a bath of acetone followed by the same procedure in a bath of ethanol. The steel wire was cleaned in a solution of 50% phosphoric acid and 50% water at room temperature for 3 min. This solution removes the oxide layer and deposits a thin phosphate layer.

Composite specimens were cast in the apparatus shown by the schematic in Fig. 2.3. The reinforcement material was placed in the sealed end of a 7 mm inner diameter quartz-glass tube. The tube was necked about 1 cm above the reinforcement, and then ingots of the matrix material were placed in the tube above the neck. The constriction minimizes premature contact and thus excessive reaction between the melt and the reinforcement. The open end of the quartz tube was clamped to a flexible hose connected to a three-way switching valve; the tube could thus be evacuated with a roughing pump or pressurized with argon. Prior to heating, the tube was evacuated and then flushed with argon gas. This cycle was repeated several times to remove any residual oxygen. The tube was left under vacuum on the last cycle to minimize trapped gas in the composite sample to be formed. An additional processing step was required for casting the steel wire composites. The wires were held at 973 K for 2 h under vacuum to remove any hydrogen absorbed by the steel during the acid etch; this step will hereafter be referred to as the wire bakeout.

The sample tube was heated in a resistive tube furnace with temperature feedback control. The initial heating stage was at 1228 K ± 20 K, well above the liquidus temperature (993 K)[11] of the glass-forming alloy. This initial heating stage dissolves residual oxides and other impurity phases which

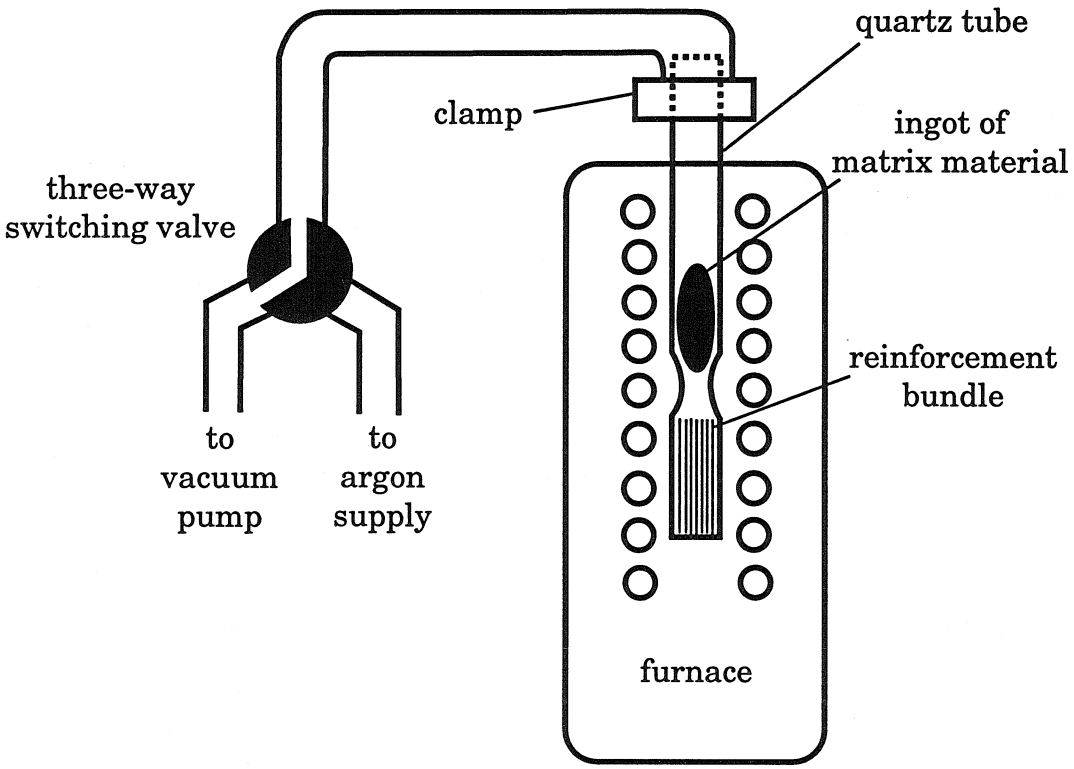

Fig. 2.3. Schematic diagram of apparatus for casting bulk metallic glass matrix composites.

degrade the glass forming ability of the alloy.[12] The error in temperature comes primarily from variations in the temperature profile in the furnace. The sample was held at this temperature for 15 min. The temperature was then lowered to 1078 K ± 5 K and allowed to stabilize. When the furnace reached this target temperature, a positive pressure of 207 kPa of argon gas was applied above the melt. These conditions were held for 30 min to allow infiltration of the molten matrix material into the reinforcement. Then the sample was quickly removed from the furnace and quenched in brine (8 wt% $NaCl/H_2O$ solution). In an attempt to improve the mechanical properties of the steel, some of the steel wire reinforced samples were tempered at 588 K for 2 h following infiltration and quenching. A graph of the time, temperature, and pressure during processing is shown in Fig. 2.4.

Porosity was estimated by two methods. The first finds the apparent porosity by analysis of a micrograph of a cross-sectioned sample. The bulk sample porosity can then be extrapolated by assuming homogeneity throughout the sample. This technique has been used for other materials as described in an ASTM standard.[13]

The second method of determining porosity combines analysis of the cross section with Archimedes' principle. As a consequence of the processing procedure, the volume fraction of reinforcement cannot be inferred from the relative amounts of the starting materials. There is a substantial reaction layer between the as-processed composite and the quartz tube, as well as a layer of quartz which strongly adheres to this reaction layer. The quartz layer and the reaction layer must be ground off mechanically; unavoidably, some of the reinforcement and matrix gets removed as well. As a result, we cannot make a precise determination of the volume fractions from the amounts of the

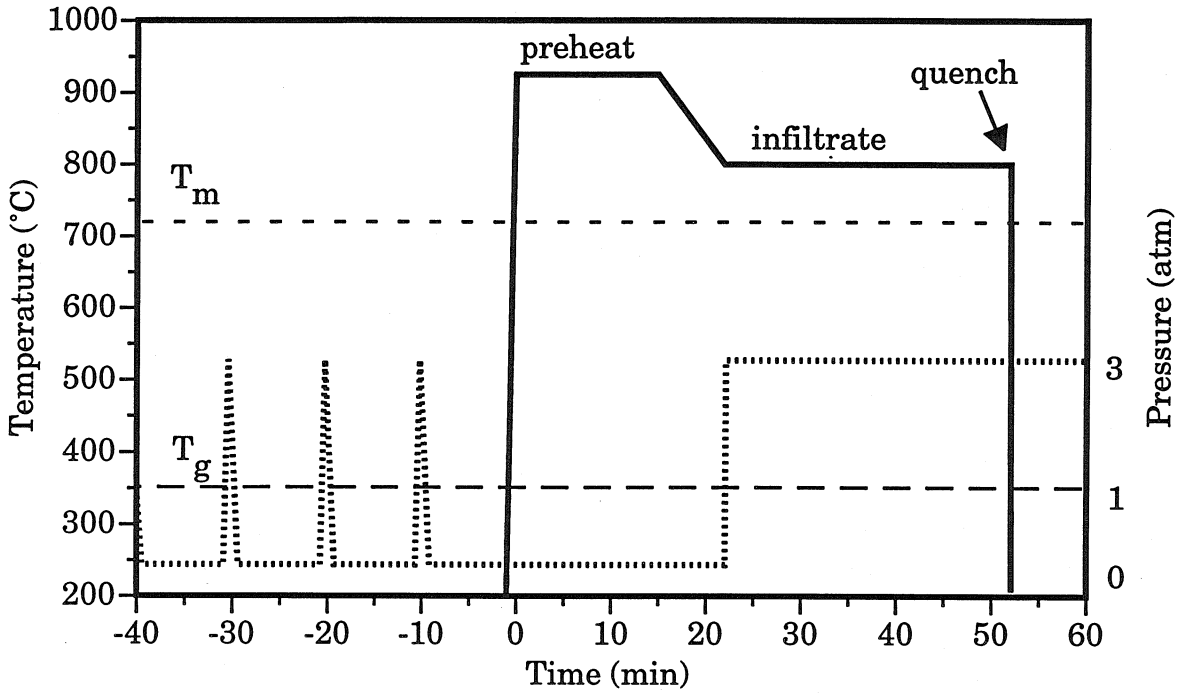

Fig. 2.4. Graph of time, temperature, and pressure during processing of the metallic glass matrix composites. Solid line represents temperature (left axis). Dotted line represents pressure (right axis). Dashed lines represent melting temperature and glass transition temperature.

starting materials.

The volume fraction of wires was computed by analyzing a backscatter SEM micrograph of the polished cross section of the sample. The relative area covered by the matrix and continuous reinforcement then gives the volume fraction of wires directly. Archimedes' principle was used to find the overall density of the sample. Then, having both the density of the sample and the volume fraction, the porosity could be calculated.

2.4 RESULTS

The quality of the composite samples produced by this technique varied with the reinforcement. At least one sample with each type of reinforcement listed in the previous section was made. The samples were judged on the extent of infiltration and the percentage of matrix which was amorphous. On this basis, tungsten and carbon steel continuous wires were chosen for more extensive study; a number of samples of each with nominal reinforcement volume fractions of 20, 40, 60 and 80 percent were made. Fig. 2.5 shows a photograph of typical samples produced. The samples shown from top to bottom are: a steel-reinforced sample as cast, a tungsten reinforced sample after grinding off the surface layer and being cut to length, a tungsten-wire reinforced sample as cast.

The porosity of two samples were measured: one with nominally 60 vol % tungsten wire reinforcement and the other 80 vol %. Upon evaluation of SEM micrographs of polished cross sections, the apparent porosity of the composites was found to be less than 1%. By calculating the volume fraction and using Archimedes' principle as described in the previous section, we determined a porosity of $3\% \pm 2\%$.

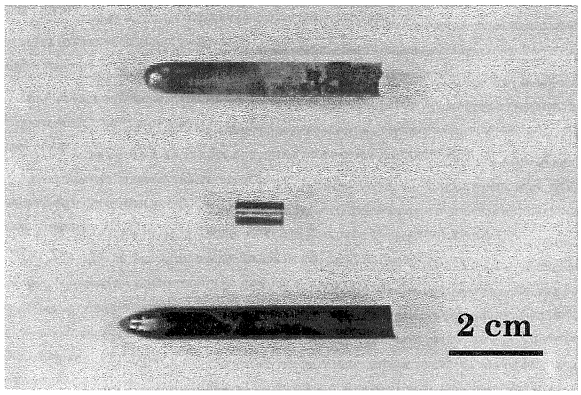

Fig. 2.5. Photograph of metallic glass matrix composite samples. From top to bottom: an as-cast steel-wire-reinforced sample, tungsten wire reinforced sample after grinding and cutting, and an as-cast tungsten-wire-reinforced sample.

The quality of the tungsten-reinforced composites was very consistent; more complications arose in making the steel wire reinforced composites. Prior to using the bakeout step, there was evidence that gases were released from the steel wires during processing. The samples with nominal 20 and 40 vol % steel wire were made before the problem was found, and thus without the bakeout procedure. To avoid possible trapped gas porosity and hydrogen embrittlement of the steel, the bakeout procedure was added prior to processing the composite samples in the 60 and 80 vol % steel samples.

2.5 DISCUSSION

Different reinforcements were chosen for initial trials for a number of different reasons. Properties under consideration included high melting point, low reactivity, ductility, toughness, strength, elastic modulus, availability, price, or some combination thereof. The reinforcement systems which worked exceptionally well initially were chosen for further studies.

To take advantage of the mechanical properties of the metallic glass in the composite, it is important to avoid crystallization of brittle intermetallics.[14] Clearly, for quenching a sample from the melt, a low critical cooling rate is advantageous and allows larger samples to be easily processed and fabricated. Vitreloy™ 1 has one of the lowest reported critical cooling rates of any metallic glass forming alloy. In addition, the low liquidus temperature of the alloy allows processing of the molten alloy at a relatively low temperature, and, accordingly, results in a minimal reaction between the matrix and reinforcement.

The extremely high melting point of tungsten (3680 K) is consistent with both a small thermal effect on the microstructure of the wire during processing

and limited reactivity with the melt. Although the microstructure of steel is not as stable at the processing temperatures, the glass is tolerant of small additions of iron[15], which partially explains the ease with which steel-reinforced composites are made.

Nevertheless, addition of reinforcements to a bulk metallic glass can allow samples to be made larger than with the glass alone. The amorphous matrix material has a thermal conductivity of about 0.035 W $cm^{-1}K^{-1}$ at room temperature. We would expect a somewhat lower thermal conductivity for the undercooled melt, which is the material of interest in determining critical cooling rates. Tungsten and carbon steel have thermal conductivities of 1.74 W $cm^{-1}K^{-1}$ and 1.0 W $cm^{-1}K^{-1}$ respectively[16], and remain solid during the processing. The addition of higher thermally conductive materials in the composite allows heat to be removed from the composite more efficiently than in the unreinforced amorphous alloy, thus allowing the critical cooling rate to be reached in larger samples.

During the initial stage of processing, prior to infiltration, the metallic glass is preheated to the minimum temperature required to remelt any residual crystalline particles present in the starting ingots. Lin et al. found in another bulk glass-former that preheating a few hundred degrees above the melting temperature is necessary to achieve maximum undercooling.[12] The conclusion from that study is that crystallization of the melt is controlled by nucleation of oxide particles; the preheat must exceed the liquidus temperature of the oxides to get maximum undercooling. We expect a similar phenomenon in the Zr-Ti-Cu-Ni-Be system. This study provided the motivation for the initial preheating step discussed earlier. Ongoing research in this area, including preliminary

results from the TEMPUS facility aboard the space shuttle flight MSL-1, indicate that this is indeed an important consideration.

Under the given processing conditions, unreinforced metallic glass samples are fully amorphous under x-ray diffraction analysis. At higher temperatures, the viscosity of the melt drops and the likelihood of exposing the reinforcement to the melt during the preheat step increases. At the temperature of the preheat step, we found significantly more reaction between the reinforcement and matrix. In addition, even if the neck in the quartz tube succeeds in preventing contact between the melt and the reinforcement, there is reaction between the melt and the quartz. Titanium, zirconium and beryllium all form very stable oxides; all three are more thermodynamically stable than silicon dioxide per mole of oxygen. Thus, we expect the quartz to be reduced by contact with the melt. This reaction is obvious in the final sample and is responsible for the observed interlayer between the composite and the quartz. This is unavoidable to some extent with this technique, but because we suspect that oxygen is detrimental to the glass-forming ability of this alloy, we try to minimize this silica reduction reaction.

We chose the processing conditions to minimize the total reaction between the reinforcement and the matrix. In some cases, it is possible that some reaction is desirable for optimal interfacial characteristics. For insufficient interfacial reactions, reaction time can simply be extended. Far more common is the problem of excess reaction between matrix and reinforcement.

Conditions for the final stage of processing were chosen to allow sufficient time for full infiltration of the reinforcement by the melt with minimal reaction. Because of its higher viscosity, the glass-forming alloy takes longer to infiltrate the reinforcement than conventional metal matrix materials do. At the

temperature of this processing step, the viscosity of the molten alloy is about 4 Pa·s.[17] By comparison, aluminum at its melting point is about 1 mPa·s.[18] Lower viscosities at higher temperatures would allow shorter infiltration times, but with increased reaction between the matrix and reinforcement. We found that there was more reaction between matrix and reinforcement at higher temperatures, despite shorter processing times.

Although the two samples measured have low porosity, we suspect this value may not be representative of all samples, particularly those of lower volume fractions. The porosity of samples with lower volume fractions of reinforcement is also more difficult to measure with the techniques listed in this chapter. In these samples, the wires have a greater off-axis misalignment; the assumption of homogeneity in the cross section of the composite rod becomes a less valid one. Also, porosity did not generally seem to be well distributed throughout the samples. Often, there would be a relatively large void present which became apparent after mechanical testing, or else there would seem to be no voids at all.

2.6 CONCLUSIONS

Composites with a bulk metallic-glass matrix can successfully be made by slow melt infiltration of the reinforcement. Under the right processing conditions, very little reaction occurs between the matrix and reinforcement, and the matrix freezes to an amorphous structure. Many reinforcement materials and geometries can be used successfully. The best results were with uniaxial tungsten and steel wires, and silicon carbide particulate preforms. The matrix material used was $Zr_{41.2}Ti_{13.8}Cu_{12.5}Ni_{10.0}Be_{22.5}$, but this technique should be applicable with other bulk metallic glass alloys.

Further work can improve the composite in a number of ways. Simple changes could easily be made, such as processing with other types of tubes which would not react and introduce silicon and oxygen into the melt. Preliminary work has shown that stainless steel tubes can be used for processing in this manner. Materials other than quartz may be cheaper, more easily handled without breakage, and even reusable. Also, different container materials might allow other bulk metallic glasses to be used, in particular, ones without beryllium. Beryllium oxide is toxic as an airborne particulate; beryllium-free alloys would alleviate related safety concerns and eliminate the need for special handling procedures during processing. Most of the other good glass forming alloys do not wet quartz during processing; as a result, they tend to not maintain good thermal contact with the container during the water quench and cannot achieve the critical cooling rate for bulk samples.

Another obvious path of further work is to experiment with other reinforcements in an effort to achieve specific properties in the composite. This could include materials such as carbon fibers for low density and high stiffness, or tantalum and tungsten-rhenium for more plastic strain. Also, particulate, multiaxial continuous fibers and multiaxial discontinuous fiber reinforcements have the potential to have properties better suited to certain applications.

REFERENCES

1. T. W. Clyne and P. J. Withers, *An introduction to metal matrix composites*, Cambridge University Press, Cambridge (1993).

2. T. S. Srivatsan, T. S. Sudarshan and E. J. Lavernia, *Prog. Mater. Sci.* **39**, 317-409 (1995).

3. P. Duwez, *Trans ASM* **60**, 607-633 (1967).

4. S. J. Cytron, *J. Mater. Sci. Let.* **1**, 211-213 (1982).

5. M. Narasimhan, US Patent 4,330,027 (1982).

6. H. Kimura, B. Cunningham and D. G. Ast, *Proc. 4th Int. Conf. on Rapidly Quenched Metals* (edited by T. Masumoto and K. Suzuki), 1385-1388, Japan Instit. Metals, Sendai (1982).

7. D. G. Ast, US Patent 4,523,625 (1985).

8. P. G. Zielinski and D. G. Ast, *MRS Symposia Proc.: Rapidly Solidified Metastable Materials* (edited by B. H. Kear and B. C. Giessen), 189-195, Elsevier, New York (1984).

9. J. F. Williford and J. P. Pilger, US Patent 3,776,297 (1973).

10. G. Nussbaum and D. G. Ast, *J. Mater. Sci.* **22**, 23-26 (1987).

11. A. Peker and W. L. Johnson, *Appl. Phys. Lett.* **63**, 17, 2342-2344 (1993).

12. X. Lin and W. L. Johnson, *subm. Mater. Trans. JIM* (1997).

13. *Annual book of ASTM standards*, Vol. 02.05, ASTM, Philadelphia (1991).

14. W. L. Johnson, *Materials Science Forum Proc. ISMANAM-95* (edited by Robert Schultz), **225-227**, 35-50, Transtec, Switzerland (1996).

15. A. Peker and W. L. Johnson, US Patent 5,288,344 (1994).

16. *Handbook of Chemistry and Physics*, 12-120, 72nd edition, CRC Press, Boca Raton (1991).

17. R. Busch, A. Masuhr, E. Bakke and W. L. Johnson, *MRS 1996 Fall Symp. on Glasses and Glass Formers* (1997).

18. *Handbook of Chemistry and Physics*, 6-169, 72nd edition, CRC Press, Boca Raton (1991).

CHAPTER 3
MICROSTRUCTURE OF THE BULK-METALLIC-GLASS MATRIX COMPOSITE

3.1 RESULTS OF MICROSTRUCTURAL ANALYSIS OF COMPOSITES REINFORCED BY TUNGSTEN AND STEEL

3.1.1 X-Ray Diffraction

Samples of the composite were characterized by x-ray diffraction. Both tungsten-wire and steel-wire uniaxially reinforced samples were tested with this technique. Unless specified, all samples were made with the processing parameters specified in Chapter 2 (15 min preheat at 925 °C, 30 min infiltration at 800 °C). After a sample was made, a cross-sectional slice was cut perpendicular to the axis of the wires. The edge of the slice was ground off to remove the reaction layer between the metallic glass and the quartz tube.

Two different x-ray diffractometers were used for the results reported here. One was manufactured by Inel, and uses a 120° position-sensitive detector. This instrument is particularly useful because diffraction peaks over a broad angular range can be simultaneously detected. Cobalt Kα radiation with wavelength of 0.1790 nm was used with this apparatus. The other instrument used was a Siemens D-500 diffractometer with a copper x-ray tube (for Kα radiation, λ= 0.1542 nm). This apparatus uses a θ-2θ goniometer configuration for the sample and the x-ray detector to mechanically scan through a range of angles. This diffractometer provides better resolution capability compared to the Inel machine. For calibration, peaks from a silicon powder sample were measured and compared to tabulated values; this gave a correction function for the diffractometer.

Samples of various fiber volume fractions were tested. The results are show in Fig. 3.1. Composites with steel wire reinforcement and ones with tungsten wire reinforcement are shown in this figure. The percentage refers to the nominal volume fraction of reinforcement. In the middle, there is also a diffraction pattern from an unreinforced metallic glass rod prepared in the same manner as the composites. The boxed annotations denote the reflections from the reinforcement material. These patterns were taken on the Inel diffractometer with position-sensitive detector.

Both tungsten and iron have body-centered-cubic (BCC) structures. The diffraction peaks with boxed labels from the tungsten reinforced composite correlate well with tabulated interplanar spacings of tungsten. In the steel-reinforced composites, considering the composition of the steel and the heat treatment it receives during processing, we expect a mixture of bainite and martensite to form. Bainite is a two-phase structure of ferrite (α-Fe) with cementite (Fe_3C). Martensite has a tetragonal structure; the c-axis lattice parameter is slightly different than the other axis. This difference creates a splitting in the diffraction peaks. The magnitude of the splitting is quite sensitive to carbon content. We shall see later than the matrix-reinforcement interface is carbon-rich, probably from diffusion of carbon from the wire; thus there will be a lower carbon concentration in the steel than expected from the starting composition.

The diffraction patterns from Fig. 3.1 show that the matrix is mostly amorphous, with small crystalline peaks which do not correspond to the wire reinforcement pattern. The pattern from the unreinforced samples display only the broad bands characteristic of glassy structures. Experience has shown that this generally indicates that the sample is at most about 2 vol%

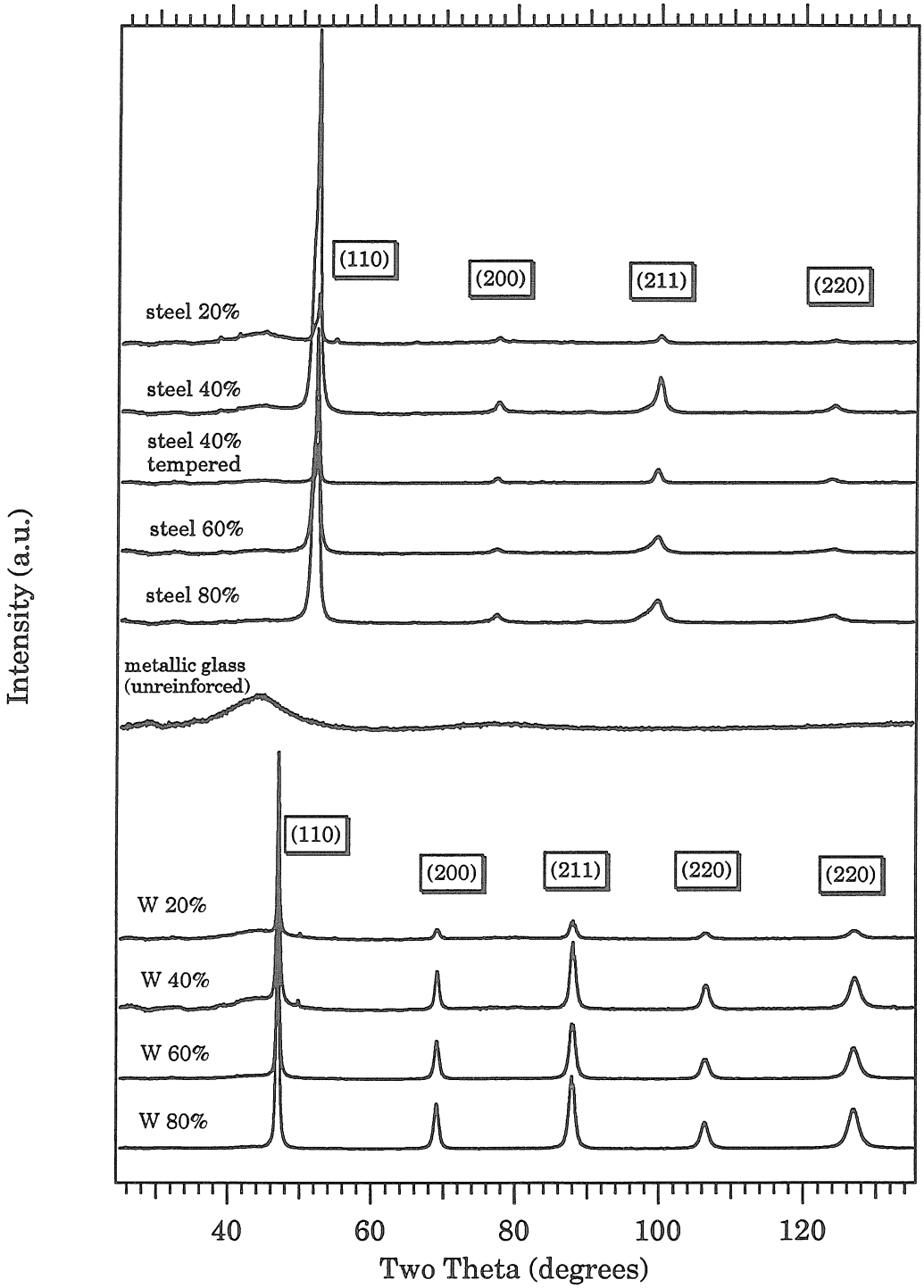

Fig. 3.1. X-ray diffraction patterns of metallic glass matrix composites. Cobalt Kα radiation (λ=0.1790 nm) was used.

crystalline; any smaller fraction is not detected by x-ray diffraction techniques of this type. The small crystalline peaks only appear in samples with low volume fractions of wires, for both types of reinforcements. In the samples with higher volume fractions of reinforcement, the pattern from the wire obscures the lower intensity patterns from the amorphous matrix and the crystallized portions of the matrix.

Fig. 3.2 shows x-ray diffraction patterns of a 20 vol% steel reinforced sample, a 20 vol% tungsten wire reinforced sample, and a pure metallic glass sample for reference. The y-axis plots intensity as usual, but the x-axis is scaled using Bragg's Law to plot the interplanar spacing. Thus, the appearance of the patterns is slightly distorted compared to a plot versus 2θ. Numbers next to each crystalline peak correspond to the interplanar spacing. Numbers in boxes correspond to the diffraction peaks from the reinforcement material. Each boxed number also has a set of coordinates referring to the family of planes responsible for the given diffraction peak.

Fig. 3.3 shows two x-ray diffraction patterns from a sample of 20 vol% steel wire composite. Like the pattern in Fig. 3.2, the peak intensities are plotted versus interplanar spacing. Labels with both an interplanar spacing and a specific family of crystallographic planes refer to the BCC peaks from the reinforcement. Both patterns were taken by the Siemens D-500 machine. Again, there are small crystalline peaks visible, but different sets of peaks are visible in each of the patterns for the same sample. This is because the distribution of these crystalline phases are inhomogeneously distributed throughout the cross-sectional slice. All three patterns from steel reinforced samples share the peaks located at 1.65 Å, 2.34 Å, and 2.70 Å. These peaks match the three highest intensity peaks of ZrC.[1] Later in this chapter, we will

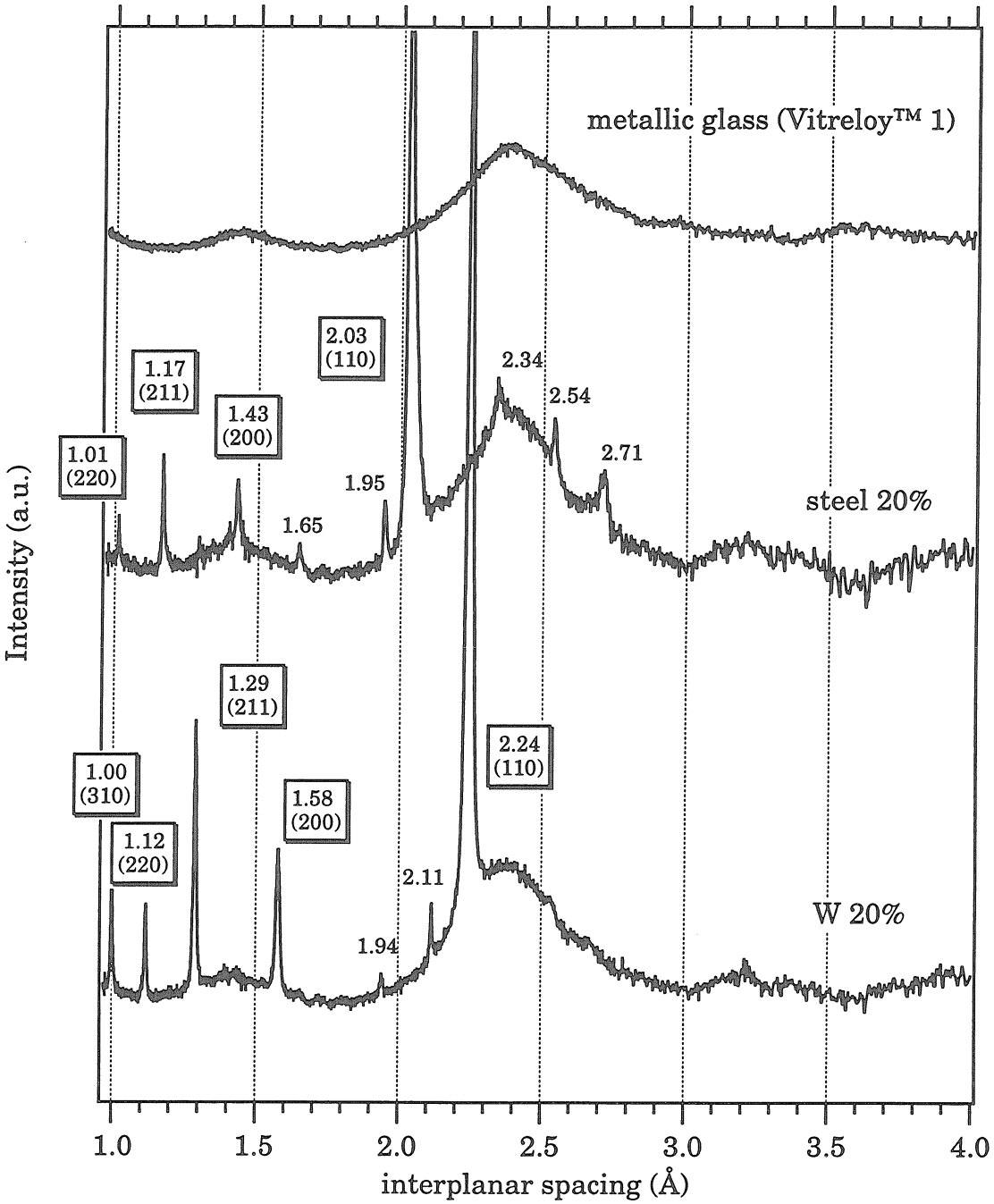

Fig. 3.2 X-ray diffraction patterns of unreinforced metallic glass and metallic-glass-matrix composites with low fiber fractions. Measured on Inel diffractometer with Co Kα radiation (λ=1.790 Å). X-axis converted to interplanar spacing from 2θ using Bragg's law.

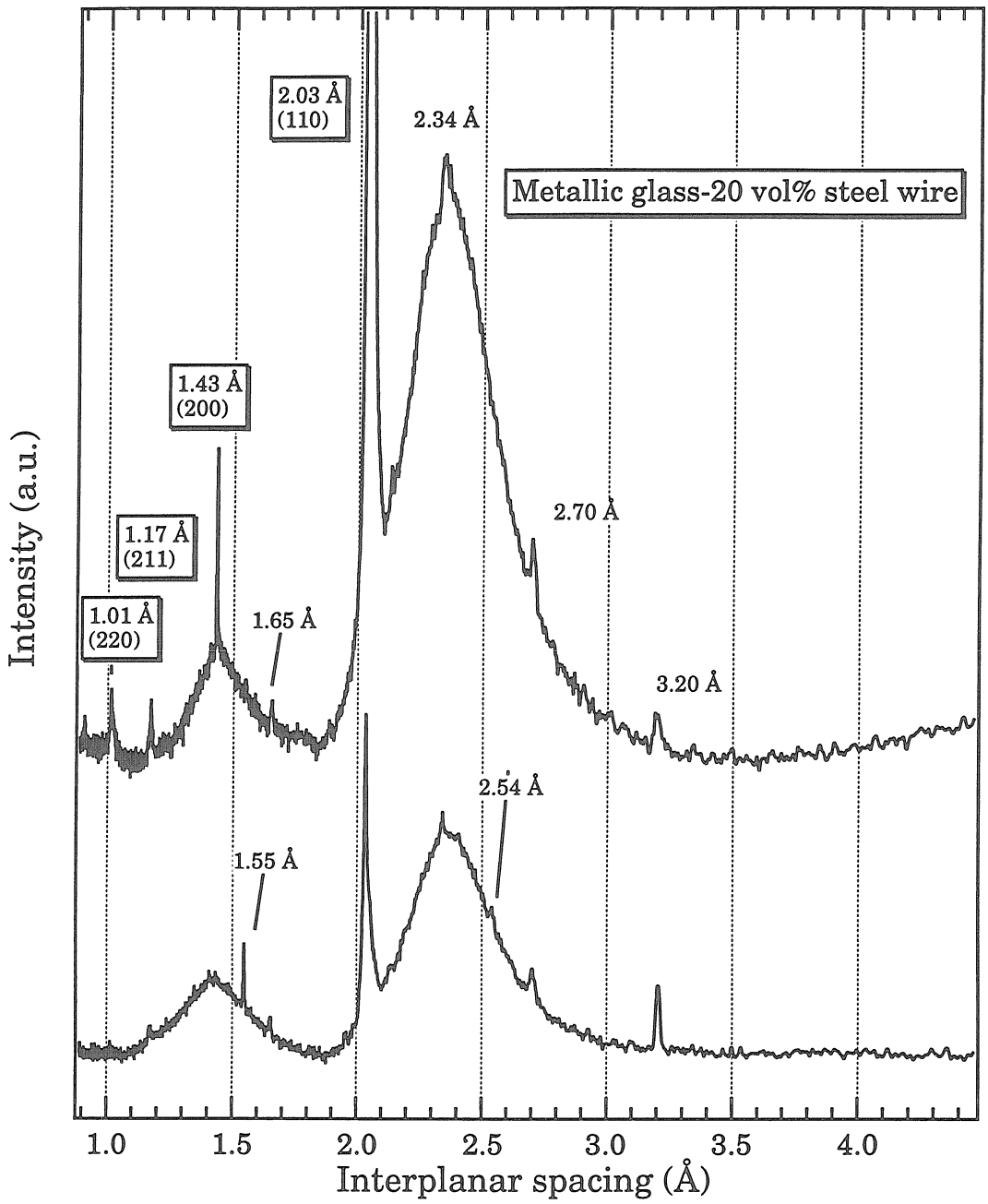

Fig. 3.3 X-ray diffraction pattern of 20 vol% steel music wire composite. Siemens D-500 was used on the same sample for both patterns.

see that this is most likely from the interfacial layer between the matrix and steel reinforcement.

3.1.2 Scanning Electron Microscopy

Scanning electron microscopy (SEM) is a useful tool for microstructural analysis of the composites. The SEM gives high resolution images of details from millimeters to microns in size. In general, backscatter images contain contrast effects from both surface topography and the average atomic number of the material. All of the samples analyzed in this section were sliced normal to the wire orientation and polished down to 0.25 μm diamond grit. A final polish was also applied using a colloidal silica suspension. Polishing sections removes topographical differences; in these samples, image contrast comes only from compositional variations.

Fig. 3.4 shows an SEM micrograph of a nominally 80% tungsten wire reinforced composite with a metallic glass matrix. Since tungsten has a higher atomic number than the average atomic number of elements composing the matrix, the wires appear lighter than the matrix. A few dark blemishes are visible in the image, particularly along the bottom edge; these are contaminants on the surface of the sample. The contamination is composed of low-atomic-number material, so it appears dark. The array of wires is seen in cross section, and is nearly close-packed. From measurement of the image, the exact fiber fraction can be calculated from the number of wires in the image, the diameter of the slice, and the diameter of the wires. Partial wires on the edges can be counted by measuring their area with a digital image processing program (NIH Image). This sample was measured to be 87 vol% wire reinforcement. This is approaching the theoretical density limit of two-

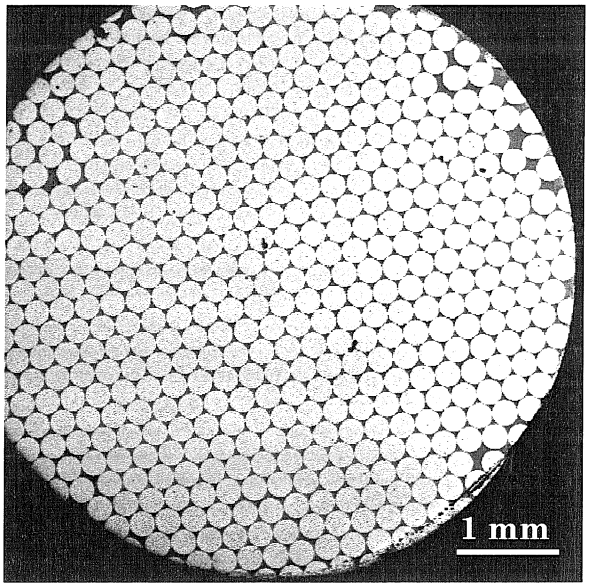

Fig. 3.4. SEM micrograph of metallic glass matrix composite. Reinforced with 80 vol% W wire. Light areas are wires. Image taken with backscatter detector.

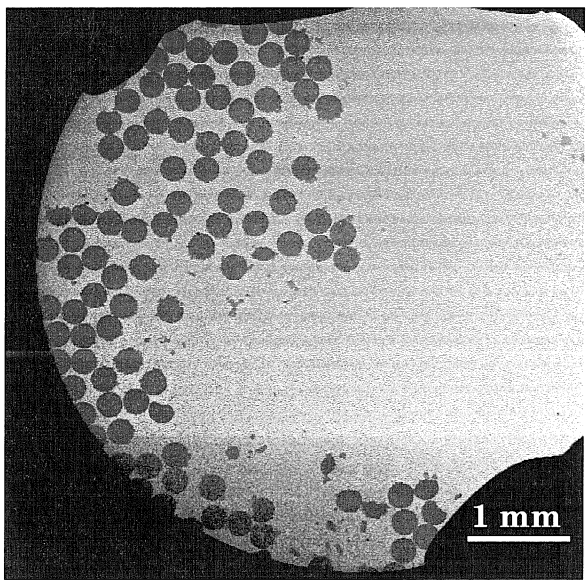

Fig. 3.5. SEM micrograph of metallic glass matrix composite. Reinforced with 20 vol% steel music wire. Dark areas are wires. Image taken with backscatter detector.

dimensional close-packing of 90.7 vol%. The nominal fiber fractions were calculated from the number of wires put into the casting tube before processing and the diameter of the tube. Apparently, many of the packing defects occur near the wall of the tube, and are subsequently ground off, leaving a higher volume fraction of reinforcement. Hereafter, all fiber fractions will be nominal values unless otherwise stated.

Fig. 3.5 shows a SEM micrograph of a metallic glass matrix composite reinforced by 20 vol% steel music wire. Again, a backscatter detector was used to acquire the image. In this figure, the reinforcement wires appear darker than the matrix. The slice appears non-circular because some carbon paint, which is used for mounting the samples on stubs for viewing in the microscope, was drawn up onto the edges of the sample. It is clear from this micrograph that the fiber distribution is quite irregular. Many of the wires are on one side of the sample. This is unfortunately typical of the samples with low fiber fractions. Because of the slight bends introduced into the wires in low fiber fraction samples, the fiber distribution does vary along the length of the sample; this provides better spatial distribution than with straight wires alone. However, there is a trade off: there is also more angular misalignment. The lower fiber fraction samples are consequently less nearly uniaxial than the high fiber fraction samples. Crystallized regions of the matrix appear as small irregularly-shaped dark regions smaller than a wire diameter distributed around the sample.

Fig. 3.6 is a backscatter SEM image of the same sample as in Fig. 3.5 at higher magnification. The round cross section of the wires are clear, although one of the wires has an oblong cross section. This may be due to dissolution of the steel into the matrix during processing, damage to the wire, or a

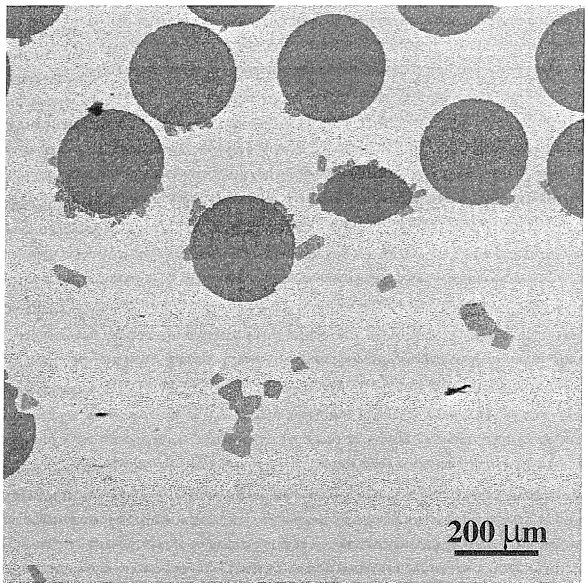

Fig. 3.6. Metallic glass matrix composite. Reinforced with 20 vol% steel music wire. Round dark areas are wires. Dark faceted regions are crystallized portions of the matrix. Image taken with backscatter detector in SEM.

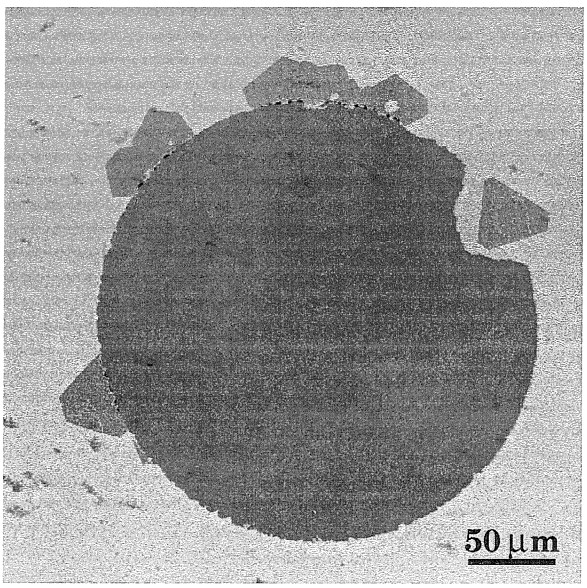

Fig. 3.7. Close up view of metallic glass matrix composite. Large round dark area is single steel wire. Crystals are visible at some locations along the wire-matrix interface. Image taken with backscatter detector in SEM.

manufacturing inhomogeneity prior to processing. Matrix crystals are visible around the wires, and alone in the matrix in the bottom center of the micrograph. Facets in these areas are clearly visible. These crystals appear darker than the matrix, indicating that they have a lower average atomic number.

An interesting fact is that the faceted crystals in the matrix seem to preferentially form on the interface with the wires, although not exclusively so. A cluster of crystals in Fig. 3.6 are a fiber diameter or more away from any wires. Since the wires are approximately normal to the polished surface, we can be reasonably sure that there is no reinforcement very close to this crystalline cluster. In Fig. 3.5, there is another cluster of crystals on the very right edge of the micrograph, which is millimeters from the nearest reinforcement wire. These crystalline clusters do not appear in the unreinforced Vitreloy™ 1 samples formed by the same processing techniques; thus we conclude that they are caused by the addition of the wires.

Fig. 3.7 shows a high magnification micrograph of the interface between a steel wire and the amorphous metal matrix. The sample is nominally 60 vol% wire reinforcement. Preferential crystallization on the interface is quite obvious. Small, very dark regions are beginning to be visible along the interface; they seem to correlate with the presence of the larger faceted crystals growing into the matrix on the interface.

Fig. 3.8 shows an interfacial region in a tungsten-wire-reinforced sample. Three wires are visible, along with the matrix material between them. Crystals in the matrix are visible both in the middle of the matrix region and directly on the interface. Nevertheless, the crystals on the interface appear larger and seem to have nucleated on the interface.

Fig 3.9 is a higher magnification SEM image of the interfacial region between a tungsten wire and the amorphous matrix. This sample was processed for a longer time; it was held at 800 °C for 160 min instead of only 30 min. Dark crystals about 5 μm in diameter appear along the interface, but not directly on the interface. This image was taken on a demonstration Philips SEM with a field-emission gun by the Philips representative. The grain structure of the tungsten wire is also visible in the micrograph. The matrix seems to penetrate between the grains of the tungsten. A few grains right on the interface appear to be completely surrounded by matrix material. In addition, the grains near the interface are significantly smaller than those deeper inside the wire. This is our first evidence of grain boundary attack on the wire material by the melt.

Fig. 3.10 shows a high magnification image of an interfacial region between a steel music wire and the amorphous metal matrix. Again, the dark faceted crystals are visible near the interface. However, they do not appear to nucleate directly on the wire-matrix interface. Smaller, extremely dark regions are visible in between the larger crystals and the wire. In Fig. 3.11, we can see these smaller crystals even more clearly, which are clustered between the wire and the large matrix crystal.

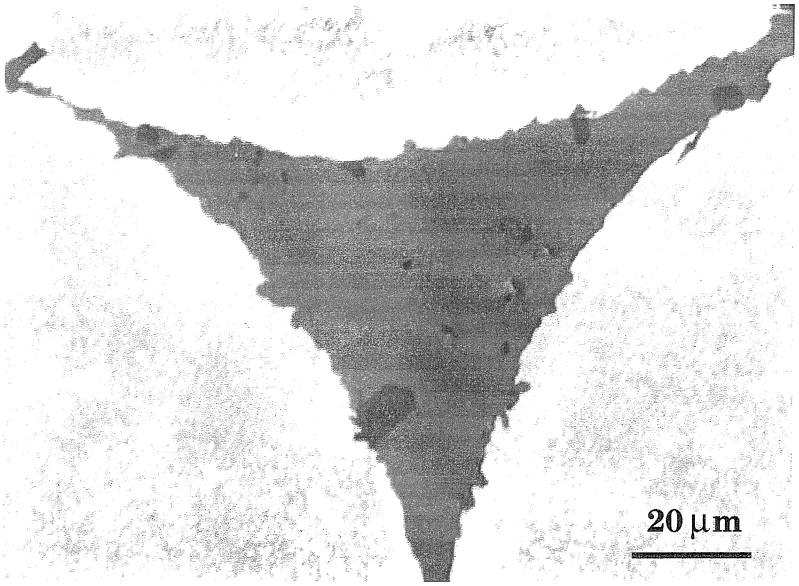

Fig. 3.8. SEM micrograph of metallic glass matrix composite. Lighter areas are tungsten wires. Dark, faceted crystals are visible at some locations along the wire-matrix interface. Image taken with backscatter detector.

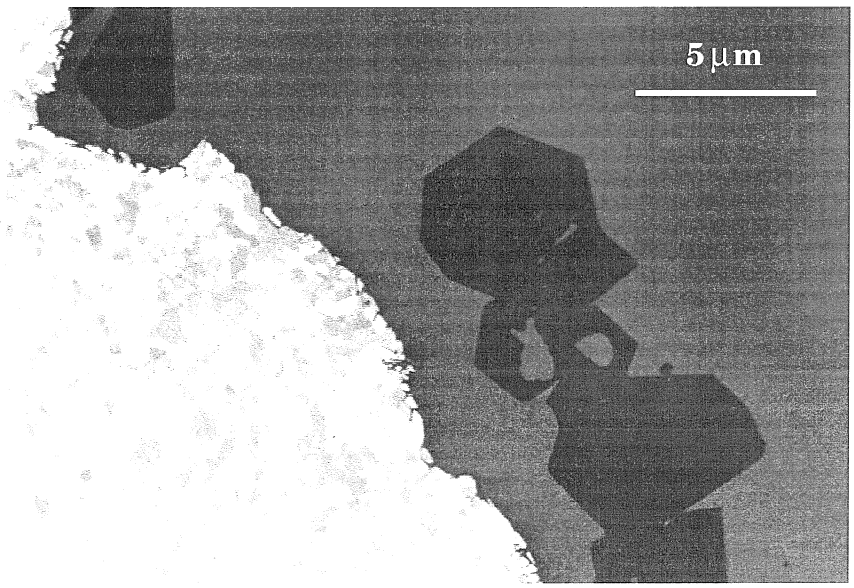

Fig. 3.9. SEM micrograph of metallic glass matrix composite reinforced by 40 vol% tungsten wire. Matrix allowed to infiltrate wires for 160 min. Light area is tungsten wire. Light gray area is matrix, and dark gray area are regions of crystalized matrix. Image taken in backscatter mode with Philips field-emission electron gun by Philips representative.

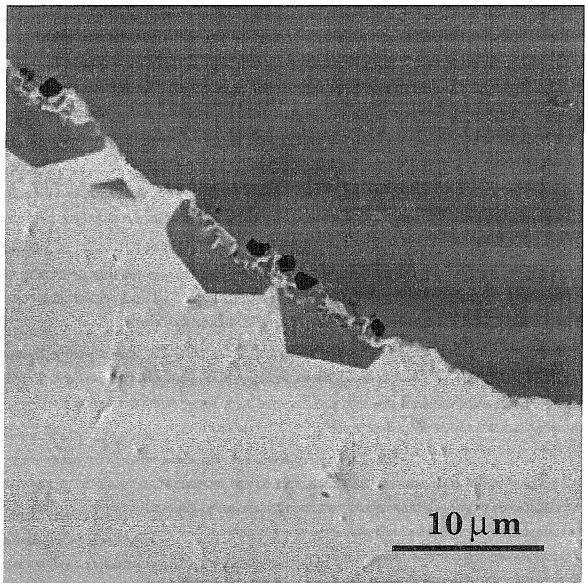

Fig. 3.10. Close up view of metallic glass matrix composite. Darker area on the top is single steel wire. Crystals are visible at some locations along the wire-matrix interface. Image taken with backscatter detector in SEM.

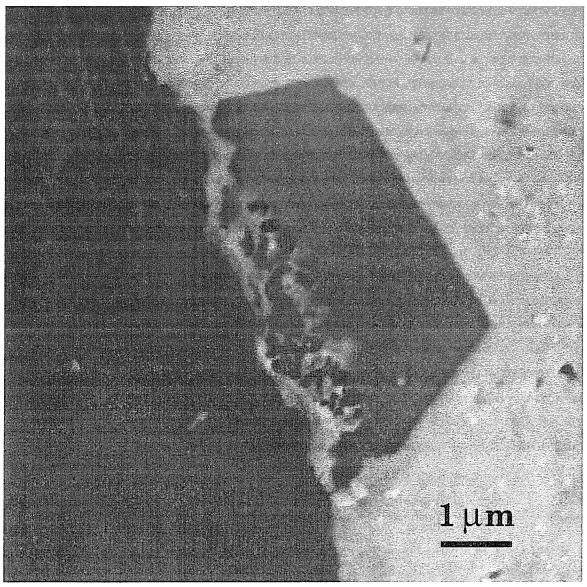

Fig. 3.11. Close up view of metallic glass matrix composite. Darker area on the left is single steel wire. Crystals are visible at some locations along the wire-matrix interface. Image taken with backscatter detector in SEM.

3.1.3 Scanning Auger Microscopy

The scanning Auger microscope (SAM) is very similar to the SEM. Both have electron guns and are used on bulk samples. However, the SAM has a detector for Auger electrons which are emitted during relaxation of ionized atoms in the sample. This is an alternate mode of relaxation to emission of x-rays, which are detected by energy dispersive x-ray spectroscopy (EDS or EDXS). However, the preferred relaxation mechanism depends upon atomic number, and thus different elements are detected more easily by one technique than the other. In particular, the Auger technique is much more sensitive to light elements such as carbon and beryllium. However, since Auger electrons can escape only from within a few angstroms of the sample surface without loss of energy, the depth of material analyzed by Auger is much less than that by EDXS; Auger is best used as surface technique. As a result, a much better vacuum is required for the SAM; the instrument used in this work was held at 10^{-9} torr. There was also an argon ion gun used for cleaning the surface of the sample in situ.

Fig. 3.12 is an image of the interfacial region of a tungsten reinforced sample taken by the secondary electron detector. Even though the contrast effect from compositional variation is not as large in secondary mode as in backscatter, there are still sufficient differences to distinguish different phases. At the top of the micrograph is the tungsten wire, which appears bright. Each white dot near a number represents a point of elemental analysis by Auger spectroscopy. The accelerating voltage of the electron gun was 10 kV. Points 1 through 3 are in the tungsten wire, progressively nearer the interface. Points 4 though 6 are in the amorphous matrix, progressively farther away from the interface. Points 7 and 10 are in two different larger, dark faceted crystals.

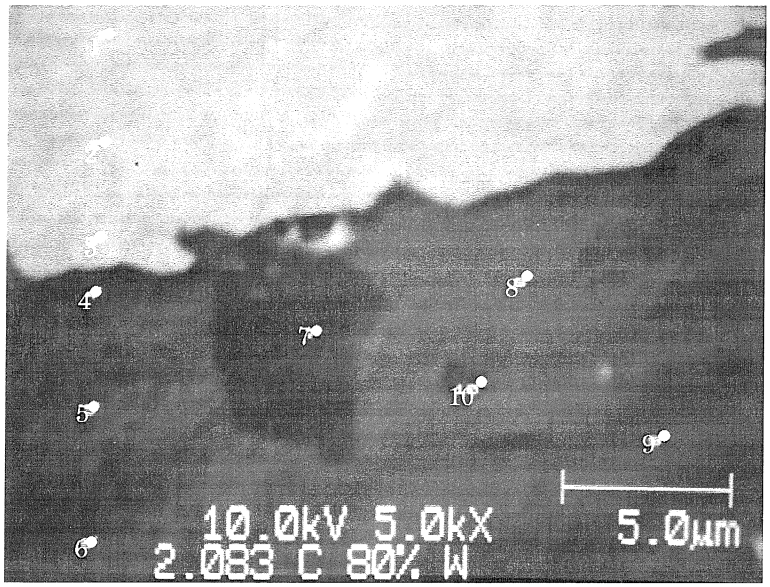

Fig. 3.12. Backscatter electron image of tungsten/metallic glass interface in composite. Each white dot and number corresponds to a point of elemental analysis in Table 3.1 with Auger spectroscopy.

Area	Zr	Ti	Ni	Cu	Be	W
#1						100
#2						100
#3						100
#4	39.5	18.4	9.1	5.4	27.6	
#5	37.8	19.6	9.5	5.5	27.6	
#6	41.0	18.9	8.7	6.0	25.4	
#7	16.6	5.1	6.5	5.9	65.9	
#8	41.6	17.0	8.7	6.6	26.1	
#9	40.0	19.2	9.5	6.4	24.9	
#10	20.9	8.2	6.3	6.7	57.9	

Table 3.1. Atomic concentrations at different points of interfacial region of tungsten wire reinforced metallic glass matrix composite. Location of points is given in Fig. 3.12. Oxygen content was excluded from analysis (see text).

Points 8 and 9 are also in the matrix, in areas with a slightly different, smoother appearance than the area analyzed in points 4 through 6.

The initial analysis performed yielded about 10 atomic percent oxygen at each of the points in the matrix. Analysis 15 minutes later yielded significantly more oxygen at the same points. This indicates that despite the precautions of sputter cleaning the surface and maintaining ultra-high vacuum (UHV) conditions in the chamber, oxygen contamination was significant. When a specific area was under analysis, the localized heating from electron bombardment probably served to getter oxygen at that spot. This effect only occurred in the matrix because of the easily oxidized constituents, particularly beryllium, zirconium, and titanium. As a result, it is impractical to measure oxygen content in this sample with this technique, and is thus excluded from analyses in this section.

Areas 1, 2, and 3 in Fig. 3.12 and Table 3.1 are pure tungsten according to the compositional analysis. At the elevated temperatures used in processing the composite, atomic diffusion into the wire was a possibility. Due to its small atomic radius, beryllium is a likely candidate as a diffusing species; fortunately, Auger analysis is quite sensitive to beryllium. As close as 1 μm away from the matrix/wire interface, to the limits of detection of the Auger analysis, there was no detectable diffusion into the tungsten. This is valuable to know, since a diffused species can drastically change mechanical properties of a material. The most salient example is hydrogen diffusion causing embrittlement in steel.

At areas 7 & 10, which are located in the large crystals, we notice a huge increase in beryllium concentration, and decreases in the relative amounts of zirconium and titanium. Points 4, 5, 6, 8 & 9, which were at various points in the amorphous matrix, all have comparable elemental compositions. These

are within the nominal composition of the alloy by about 5 atomic percent, which is within the experimental error for this technique.

Table 3.2 below shows the results of elemental analysis by Auger for a composite with steel music wire reinforcement and a metallic glass matrix. Points 1 and 2 in Fig. 3.13 were in the wire, about 12 μm and 2 μm from the interface, respectively. As we expect, both show the wire is mainly iron with some carbon. However, the measured carbon concentration is higher than we might normally expect for this alloy; it is nominally 3.6 atomic percent carbon. Again, the experimental error is large enough that we cannot make any conclusions about changing carbon concentration within the wire itself. However, we can conclude that there was no detectable amount of diffusion of any matrix species any greater than 2 μm into the wire. In addition, there was no detectable difference in composition between these two different points inside the wire.

There are a number of small dark regions appearing in Fig. 3.13 which did not occur in the image of the other composite sample. Some, such as the one analyzed in area 3 in Fig. 3.13 and Table 3.2, are directly on the interface between the steel wire and the matrix; others, such as in Area 5, occur out in the matrix, but in the vicinity of the interface. Area 3 is approximately BeC, and Area 5 has composition approximately SiC. These measured compositions are consistent with the contrast in the image. The steel wire would be the likely carbon source for the BeC on the interface. There is often a small amount of BeC present in commercially available beryllium metal; it is unlikely, however, that this would then migrate to the interface. The silicon carbide arises from some impurity, since neither the reinforcement nor the matrix nominally contains a significant amount of silicon. It is possible during

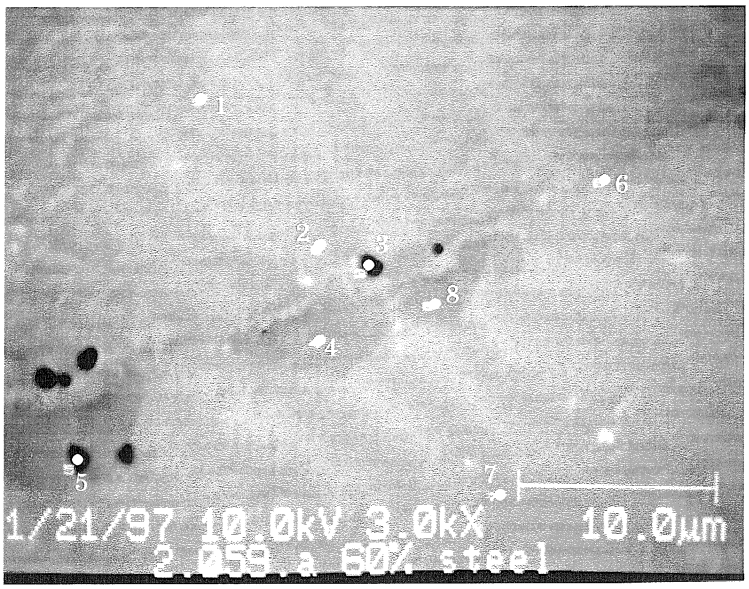

Fig. 3.13. Backscatter electron image of steel/metallic glass interface. Each white dot and number corresponds to a point of elemental analysis in Table 3.2 with Auger spectroscopy.

Area	Zr	Ti	Ni	Cu	Be	Fe	Si	C
#1						91.5		8.5
#2						90.3		9.7
#3					56.3			43.7
#4	15.5	7.9	5.8	5.6	65.2			
#5							58.9	41.1
#6	28.9	5.4					8.2	57.5
#7	44.8	23.9	11.5	7.9	???		12.0	
#8	17.0	5.8	6.1	5.6	65.5			

Table 3.2. Atomic percent concentrations at different points of interfacial region of steel music wire reinforced metallic glass matrix composite. Location of points is given in Fig. 3.13.

some stage of polishing that silicon carbide particles used as an abrasive could have become embedded, but there has been no evidence for this occurring in the metallic glass previously. It is more likely that the silicon entered the matrix from the silica tube used as a processing container. From the analysis of Area 7 in Fig. 3.13, we see also that there is substantial silicon contamination even in the non-crystallized matrix. The beryllium concentration, however, was not quantified due to overlap of its main peak with a silicon peak. The silicon, however, had another isolated peak which could be used for analysis. Thus, the beryllium concentration for this area was omitted, although there is beryllium present.

Areas 4 and 8 in Fig. 3.13 are the same phase that crystallizes in similar locations in the tungsten reinforced composites. We see from Table 3.2 that the composition is roughly the same as areas 7 and 10 in Fig. 3.12. Area 6 in Fig. 3.13 is directly on a part of the interface which is free of large crystals. The results in Table 3.2 show that it is most likely composed of a mixture of zirconium carbide, titanium carbide, and silicon carbide.

3.1.4 Transmission Electron Microscopy and Scanning Transmission Electron Microscopy

Transmission electron microscopy (TEM) studies of the composite microstructure offer a number of advantages. For one, the magnification capabilities are usually much greater than other forms of microscopy. Thus, we can image the interfacial region between the reinforcement and matrix in much finer detail. Also, since electrons are transmitted through the sample, the structure of individual phases can be analyzed, rather than only the composition. Further, the use of thinned samples in TEM allows much higher

resolution analysis by EDS. Scanning transmission electron microscopy (STEM) units can provide a spot size of 100 Å or less for compositional analysis. Unfortunately, the sensitivity of EDS to light elements is quite low. In fact, in standard EDS detectors, a beryllium window filters out all x-ray signals from elements with lower atomic numbers than aluminum. The concentrations of light elements can be measured in a detector with a specially made thin window, but getting good signal to noise ratios even with this type of equipment is difficult. Thus, all EDS data presented in this work will neglect beryllium concentrations. All the TEM work presented here was performed on a Philips EM430 electron microscope at 300 keV. It is also equipped with a EDAX 9900 energy-dispersive x-ray analyzer and a single crystal lanthanum hexaboride filament.

Fig. 3.14 is an electron micrograph of a tungsten wire/amorphous metal matrix region. The amorphous matrix lies to the upper left, and the tungsten wire to the lower right. There is a partially crystalline reaction layer about 240 nm thick between the wire and the amorphous region. It lies between the white marker lines in the bright field image (A). Diffraction patterns (B) through (E) are shown from different regions. A selected area diffraction (SAD) aperture with effective diameter of 1.6 μm was used to obtain the patterns in (B) and (E), while an aperture 0.5 μm in effective diameter was used for (C) and (D). The interfacial reaction layer was too narrow to obtain a diffraction pattern from it alone.

The diffraction spots in (B), (C), (D), and (E) in Fig. 3.14 all can be indexed to tungsten, with the exception of the smallest ring in pattern (E). This ring is most likely an artifact produced from the SAD aperture; it is too sharp to be diffraction from small crystals. See Appendix 1 for details of this analysis. The

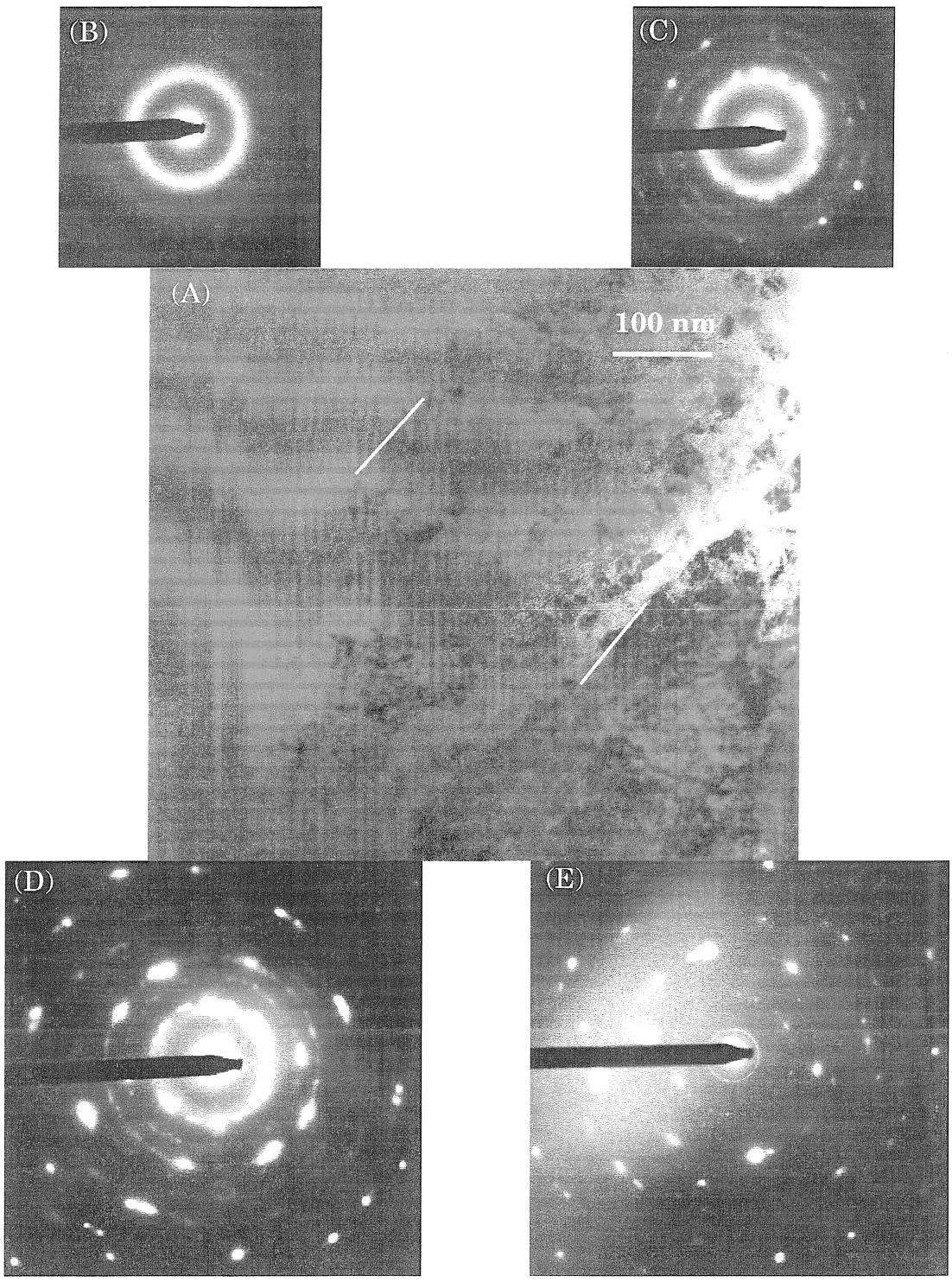

Fig. 3.14. Transmission electron micrographs of interfacial region between tungsten wire and metallic glass matrix. (A) BF image; diffraction patterns from (B) matrix, (C) reaction layer plus matrix, (D) reaction layer plus tungsten, and (E) tungsten.

presence of the broad amorphous ring in (D) indicates that the reaction layer is partially amorphous. Since the spots in patterns (C) and (D) all correlate, we can conclude that the reaction layer is simply small crystals of tungsten about 30 nm in diameter in the amorphous matrix. The faint <110> tungsten diffraction ring in pattern (B) shows that there are some tungsten crystals as far as 3 μm into the amorphous matrix away from the interface, the region from where the pattern was taken.

Fig. 3.15 shows a graph of composition versus position across a wire/matrix interface. The composite under analysis was 60 vol% tungsten wire in a Vitreloy™ 1 matrix, processed as described in Chapter 2. The analysis was performed in STEM mode, with a spot size corresponding to a 4 nm probe diameter. Along the x-axis, 0 corresponds to the boundary between the tungsten and the reaction layer, and 240 corresponds to the boundary between the reaction layer and the amorphous matrix. One fact to notice is that there is no detectable diffusion of zirconium, titanium, nickel, or copper 30 nm off the interface into the tungsten wire. We find that the reaction interlayer is composed of all the detectable components of the amorphous matrix, plus 10 to 20 atomic % tungsten, depending upon the proximity to the wire. Outside the reaction layer in the amorphous matrix there is no detectable tungsten. The actual atomic concentrations would be slightly less to account for the presence of the beryllium. There are slight variations in the measured concentrations of the four components of the glass within the reaction layer, but these do not appear to be significant. These data are consistent with the hypothesis that the reaction interlayer is composed of small tungsten crystals in a metallic glass matrix.

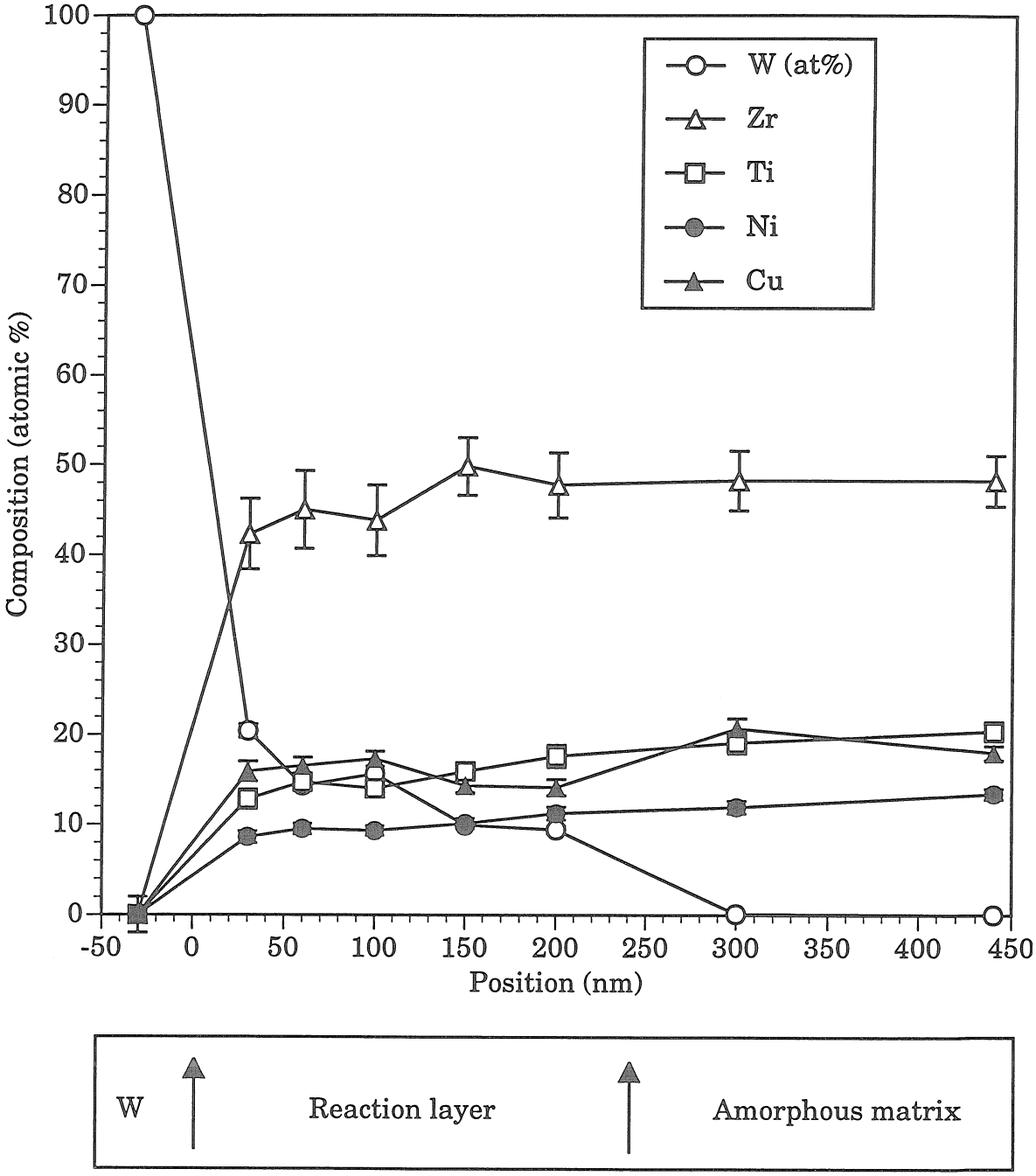

Fig. 3.15. Compositional profile across tungsten wire/matrix interface in tungsten wire reinforced composite. Measured by EDS in STEM. Beryllium concentration omitted from analysis (see text).

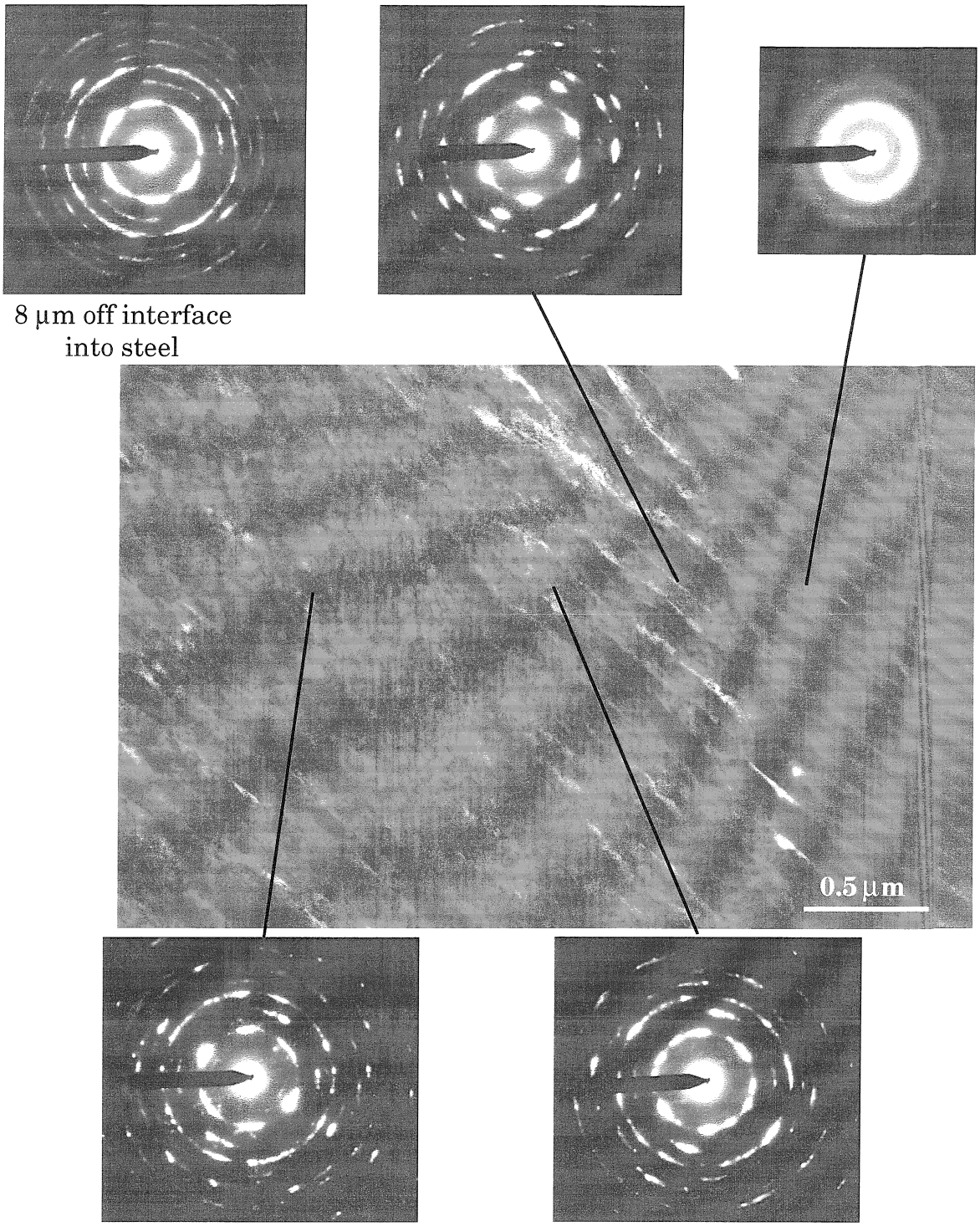

Fig. 3.16. Transmission electron micrograph (bright field) of interface between steel music wire and amorphous Vitreloy™ 1 matrix. Amorphous region on right, and steel on left. Diffraction patterns taken with 0.5 μm diameter selected area aperture, except for pattern from 8 μm into steel, which was taken with 1.5 μm aperture.

Fig. 3.16 is a transmission electron micrograph of the corresponding interfacial region for a steel music wire reinforced composite. Diffraction patterns from selected areas along the interface are shown. There is a slight texture change in the image about 1.4 μm away from the interface into the steel wire, but upon analysis of the diffraction patterns, there is no detectable difference. The only diffraction spots are from the steel. There are some faint diffraction spots from the diffraction pattern from the matrix, but these can be indexed to BCC iron. Possibly some of the wire was included in the selected area, which was chosen right next to the interface. The details of the analysis are given in Appendix 2. This difference in appearance is possibly due to a change in the microstructure of the steel near the interface.

Fig. 3.17 shows a bright field/dark field pair of electron micrographs of a steel wire/metallic glass interface. The interface is clean and with no visible reaction layer. Fig. 3.18 shows another bright field/dark field pair of electron micrographs of a steel/metallic glass interface. This region was the one used in taking the EDS compositional linescan shown in the next figure. Diffraction patterns from each area are also shown and were taken with 0.5 μm diameter SAD apertures about 1 μm away from the interface on either side. The pattern from the steel wire shows only spots from steel (Appendix 2). Note the crystal which appears in the dark field image (Fig. 3.18 (B)) in the matrix slightly off the interface. Nevertheless, in all these images taken using selected area apertures, we must remember that exact correlation between image and diffraction pattern is not guaranteed.

Fig. 3.19 is a graph of the compositional profile across this region taken by EDS in STEM mode. Like beryllium, carbon is too light to be effectively detected by this technique. There are also problems with carbon

(A)

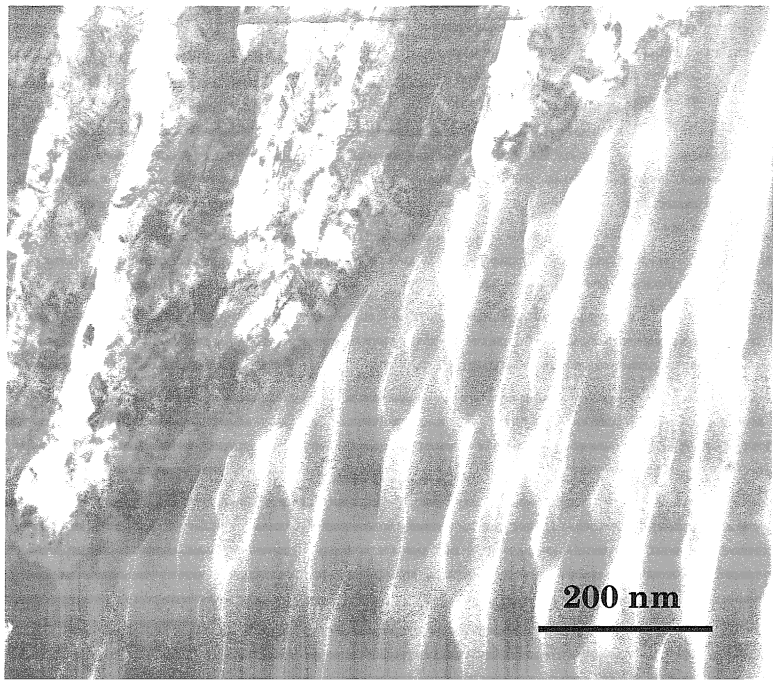

(B)

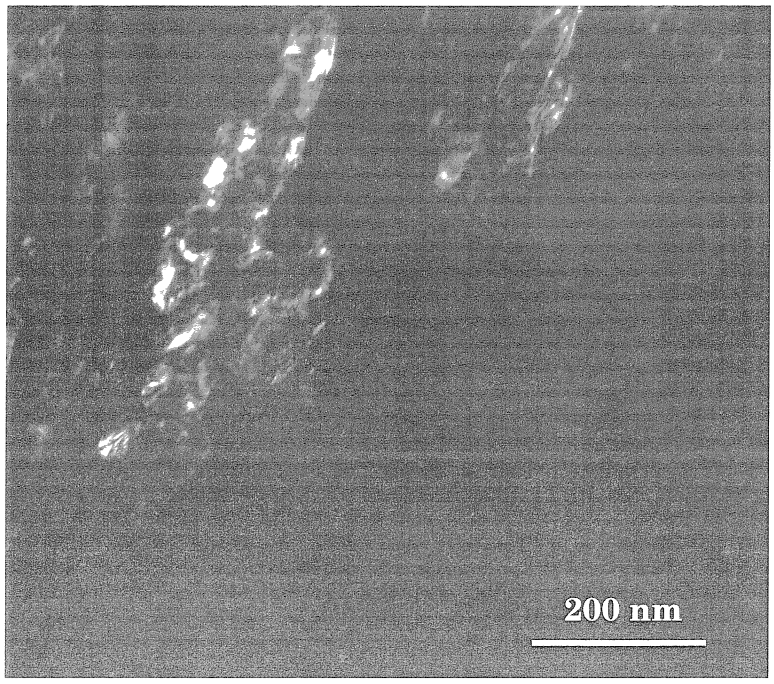

Fig. 3.17. Transmission electron micrographs of interfacial region in steel-wire-reinforced metallic glass. (A) bright field and (B) dark field. Lower right area is amorphous matrix, and upper left is crystalline wire.

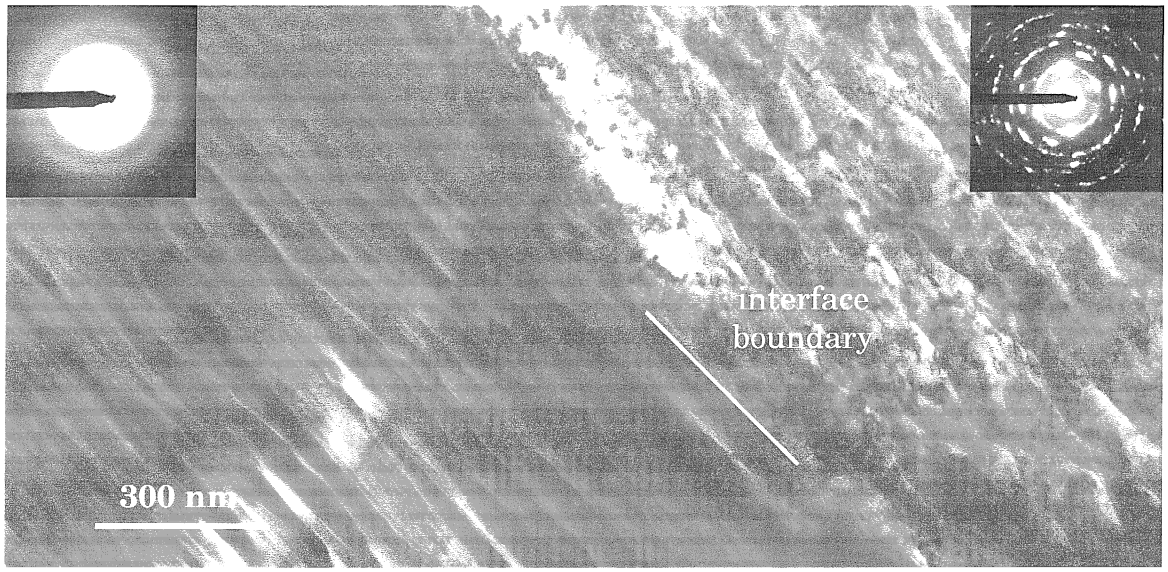

(A)

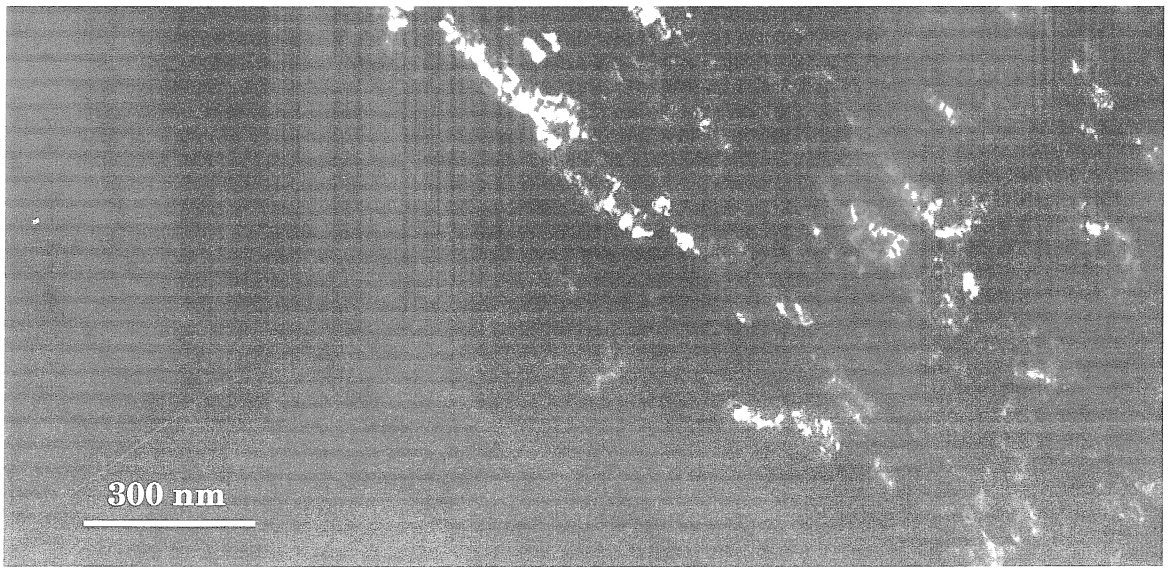

(B)

Fig. 3.18. Transmission electron micrographs in (A) BF and (B) DF of steel wire/metallic glass interface. Region used for EDS analysis profile shown in Fig. 3.19.

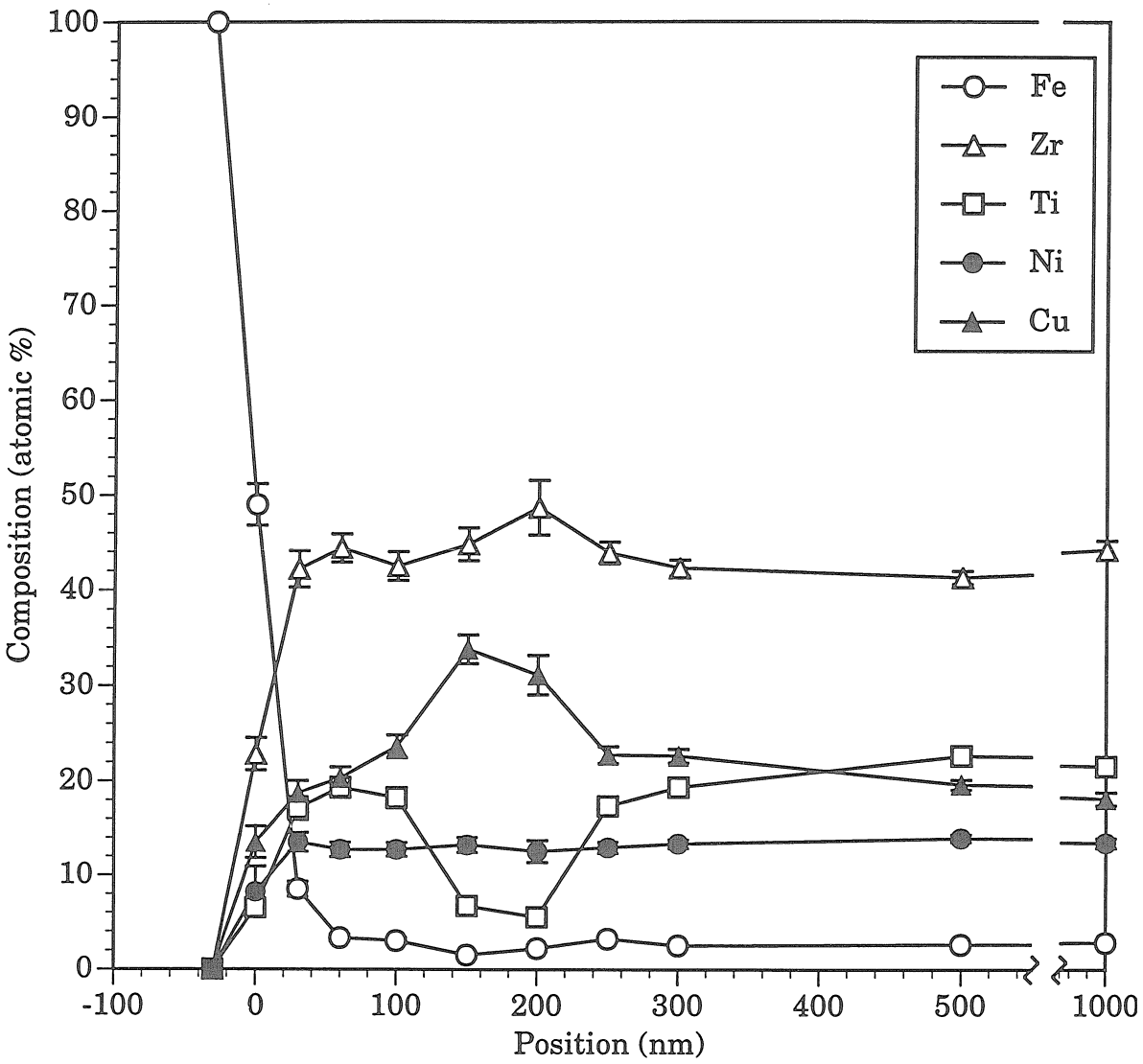

Fig. 3.19. Compositional profile across steel wire/matrix interface in steel wire reinforced composite. Measured by EDS in STEM. Beryllium and carbon concentrations omitted. Location of wire/matrix interface at 0 on x-axis.

contamination at the location of the electron beam. Like in the tungsten wire reinforced samples, there is no detectable diffusion of matrix elements into the steel 30 μm from the interface. However, there is some diffusion of iron into the amorphous matrix. The concentration drops off very quickly, to a few percent within 60 nm of the interface. This concentration appears to remain level up to 1 μm away from the interface. There is a change in composition in the matrix between 100 nm and 250 nm away from the interface. In this layer, the concentration of copper increases and that of titanium drops. This is probably due to a slightly different composition of the small crystal visible in Fig. 3.18 (B) in the matrix. The crystal is of the right size and position from the interface to correlate to this compositional change.

3.2 ANALYSIS OF RESULTS

The crystals in the matrix are most likely due to impurities on the surface of the reinforcement. Although these crystals sometimes are not directly on the interface but only in the vicinity could be simply a consequence of only viewing a single plane of material. The crystals could have nucleated on the wire below or above the surface which is being analyzed. Preliminary analysis shows that dissolved reinforcement material is not a significant constituent of the crystals; however, Figs. 3.6 and 3.8 clearly show more crystallization near the matrix-reinforcement interface. The first crystallization event which occurs upon heating in unreinforced Vitreloy™ 1 which can be detected by x-ray diffraction is the formation of a Laves phase.[2] From the Auger analysis, we find that the large crystals visible in SEM are primarily beryllium, with an approximate composition of $Be_{12}Zr_3TiNiCu$. Measurements of the relative areas in SEM images show that these crystals make up 1 to 5 percent of the

composite samples by volume. The composition can also be expressed in the form Be_2X; X is Zr, Ti, Ni, or Cu in the ratio 3:1:1:1. Again, we suspect a Laves phase structure from this composition. Beryllium forms the binary cubic C14 Laves phases Be_2Cu and Be_2Ti. This Laves phase is also known as the $MgCu_2$-type structure. A detailed description of this structure is given in ref. 3. From the results of microscopy, this Be-rich phase appears the most prevalent, and is probably a Laves phase, but further work must be performed to determine the exact structure.

In both the tungsten reinforced and steel reinforced composites, none of the elements of the matrix alloy were found within the reinforcement. It is still possible, however, that amounts below the detection limit of SAM or EDS could still affect the properties of the reinforcement.

Upon closer inspection of the x-ray diffraction pattern in the steel-reinforced samples, there is splitting in the steel peaks. The position of the second peak in the (110) reflection at 2.898 Å allows us to estimate the c lattice parameter in the martensite structure. Correlating this with tabulated results, the diffraction pattern indicates a carbon content of 0.27 wt% carbon.[4] Since the initial composition was 0.80 wt%, and additional carbon at the interface is observed, this is a reasonable estimate of the final carbon content of the steel. The cause for the larger amount of silicon in the steel reinforced sample is unclear. Embedded abrasive particles would not explain the silicon distributed in the amorphous portion of the matrix. The best explanation is that the region analyzed by SAM was closer to the quartz container during processing, and thus has a higher concentration of silicon from reducing SiO_2. It is also possible that the silicon diffused out from the steel wire reinforcement.

In considering the tungsten-reinforced composites, we can infer from estimating diffusion constants that the interfacial reaction layer was solid during processing. The following argument assumes the opposite and leads to a non-rigorous proof by contradiction. If we assume that the matrix was liquid and the tungsten atoms were dissolving and diffusing through a liquid medium, and then precipitating out upon quenching, what would be the approximate length scale of that process? For most metals near their melting point, the diffusion can be estimated at about 10^{-4} cm^2/s. However, we must recall that the viscosity of Vitreloy™ 1 at its melting point is much higher than elemental metals, as first indicated in Chapter 2. We can approximate the diffusion constant of tungsten in the molten matrix by using the Stokes-Einstein equation:

$$D = \frac{kT}{6\pi\mu r} \tag{3.1}$$

where D is the diffusion constant, k is Boltzmann's constant, T is the absolute temperature, μ is the viscosity, and r is the radius of the diffusing species. Equation 3.1 assumes that the diffusing particle is much larger compared to the particles of the medium, which is not precisely true. However, even in the case of the Sutherland-Einstein formula where the radii of the diffusing particle and the particles in the medium are equal, the diffusion constant simply increases by a factor of 3/2:[5]

$$D = \frac{kT}{4\pi\mu r} \tag{3.2}$$

If we plug in reasonable numbers (T=1073 K, μ=4 Pa·s, r=2.02 Å) to Eqn. 3.2, we find $D \approx 1.5*10^{-8}$ cm^2/s. Using a processing time of 30 min, and taking the diffusion length scale to be given by:

$$x \approx \sqrt{Dt} \tag{3.3}$$

we find x≈52 μm, which is much larger than the observed diffusion of tungsten in the reaction layer. Thus, we conclude that the reaction layer is solid during processing of the composite.

If we then assume that the particles are removed from the wire as grains, and then diffuse off from the interface into the matrix, we can again estimate the characteristic length. If we try to model the situation in Fig. 3.9, we can use a time of 160 min, and a particle (grain) size of 0.5 μm. We then get a length of about 2 μm, which is still larger than what is observed in micrographs. It is possible that the particles become completely dissolved in the matrix by the time they have diffused on the order of 240 nm from the interface. This would explain the absence of any particles farther than this from the interface.

The electron diffraction patterns and the EDS data show that the interfacial reaction layer about 240 nm thick is composed of small tungsten crystals about 30 nm in diameter in an amorphous matrix. Tungsten composes about 10 to 20 atomic % of this interlayer depending on the distance from the interface. A possible mechanism for creation of this interface is the diffusion of molten matrix material into the grain boundaries of the tungsten wire. The grains could then break apart and become interspersed in the amorphous matrix. Some dissolution of the tungsten into the matrix would also occur, yielding the smaller grain size in the reaction layer than is found in the original tungsten wire.

In the steel reinforced samples, the portions of the interface without large crystals seem to be mixed carbide layers. Diffraction data and SAM analysis indicate ZrC is the most prevalent form. Using a lattice parameter of 4.693 Å for ZrC and a cubic structure, we find a peak at 2.71 Å is a (111) reflection, at

2.35 Å is a (200) reflection, and the peak at 1.66 Å is a (220) reflection. An interesting point is that this carbide layer seems to be passive with respect to further crystallization of the matrix. That is, it does not appear to act as a heterogeneous nucleation site for the metallic glass. This is consistent with other observations in the laboratory. Masuhr at Caltech has done extensive processing of Vitreloy™ 1 above the liquidus point of the alloy in a graphite crucible.[6] These experiments show that even after keeping the melt at elevated temperatures for hours, it can still be cooled to a glass; carbon and the resulting reaction layers do not seem to be detrimental to glass formation. Nevertheless, there often are small low-atomic number particles on the interface where larger crystals nucleate in steel-wire-reinforced composites. We found one example in Fig. 3.13 where this particle was determined by Auger analysis to be BeC. The role of carbides in crystallization of the matrix is unclear.

Further, in the steel reinforced samples, there does appear to be substantial dissolution and diffusion of iron into the matrix. From the data in Fig. 3.19, we see that the characteristic length for such diffusion is certainly longer than 1 μm; this is consistent with the estimation given above for the diffusion length calculated by the Sutherland-Einstein formula. Also, Peker and Johnson found that Vitreloy™ 1 remains a bulk-glass-former even with additions of up to about 10 atomic % iron.[7] So, we can expect that the concentrations of iron which were found to diffuse into the matrix would not cause the matrix to crystallize.

3.3 SILICON-CARBIDE AND OTHER REINFORCEMENTS IN METALLIC-GLASS-MATRIX COMPOSITES

In the preliminary stages of this work, considerable effort was put into trying a wide range of different types of materials to determine what reinforcements could be successfully incorporated into a metallic glass matrix. Frequently, the matrix of the samples had crystallized. Usually only a single sample was made of any given reinforcement type; since processing conditions depend upon the materials involved, the procedure was not optimized for each type of reinforcement. This initial screening process determined which reinforcements could be incorporated into a composite most easily. However, significantly different results were obtained using different processing techniques.

A number of experiments were performed in an attempt to incorporate silicon carbide fibers into the amorphous metal matrix. The first generation of these composites were made by inductively heating ingots above a fiber bundle in a sealed and evacuated quartz tube. The melt flowed down and infiltrated the fibers by capillary action. The melt was estimated to be 1500 K or higher with this technique, but there was no way to accurately control and stabilize the temperature. In the time required to infiltrate, enough of the fiber material had dissolved to destroy the glass-forming ability of the matrix.

In an effort to achieve better temperature control, the induction coil was replaced by a resistive furnace with an active temperature controller. Different arrangements were tried until one was found with a sufficiently spatially large and homogeneous temperature zone. An inert gas line was added to provide back pressure to assist infiltration. One sample was made by infiltrating polycrystalline silicon carbide fibers with Vitreloy™ 1 for 3 h at 1098 K. Fig. 3.20 shows a map of carbon concentration for a cross section of

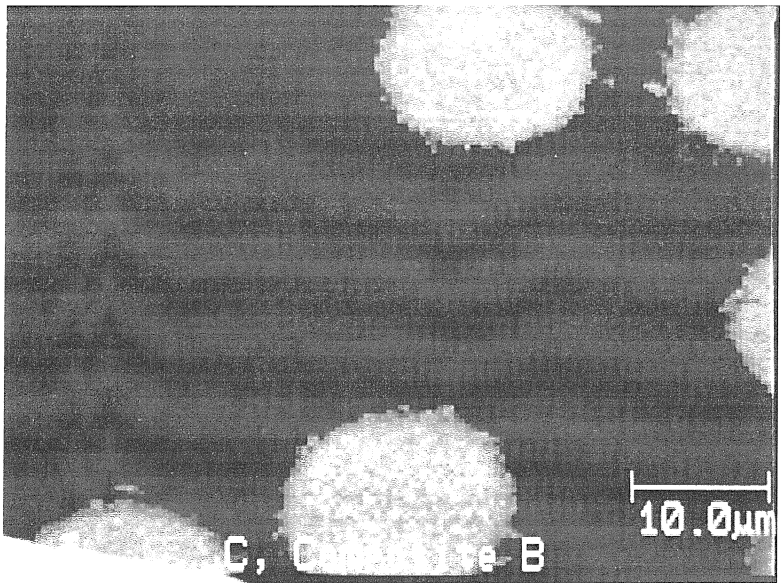

Fig. 3.20. Carbon compositional map for SiC/Vitreloy™ 1 composite. Image taken with SAM. Sample infiltrated for 3 h.

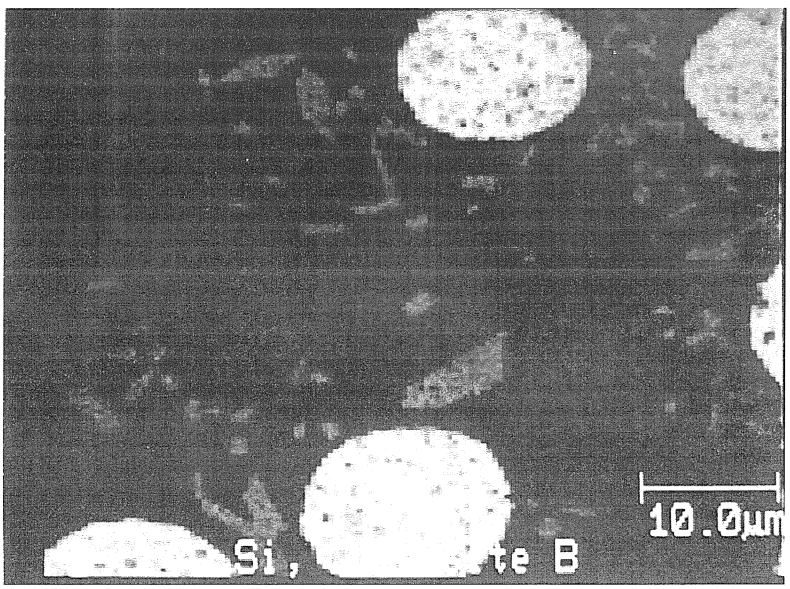

Fig. 3.21. Silicon compositional map for cross section of SiC/Vitreloy™ 1 composite. Image taken with SAM. Sample infiltrated for 3 h.

this sample from scanning Auger microscopy (SAM). The Auger analysis of the silicon carbide-reinforced composites was performed by the Carborundum Company. Areas high in carbon appear lighter. The fibers are slightly off-axis with the plane of the section, and thus appear as light-colored ovals. Fig. 3.21 shows a map of the same area for silicon. The silicon clearly plays a role in the crystallization of the matrix; these silicon-rich regions are faceted and clearly not amorphous. Even though there is an equal fraction of silicon and carbon available, the carbon does not segregate in this fashion, and does not appear to encourage crystallization.

Figs. 3.22 and 3.23 show the same type of compositional maps for a similar silicon carbide composite sample; however, this one was processed at 1098 K for only 0.5 h instead of 3 h. The compositional map in Fig. 3.22 shows no appreciable carbon in the matrix, similar to Fig. 3.20. But Fig. 3.23 also shows that for this sample there was no appreciable silicon dissolved into the matrix, either. Clearly, the processing time and the reinforcement composition play important roles in determining matrix microstructure.

However, further analysis of the silicon-carbide-reinforced samples processed for 0.5 h showed some small crystals in the matrix. These are beryllium-rich regions visible in the beryllium map shown in Fig. 3.24. These crystals are clearly not the same type as those visible in Fig. 3.21. These smaller crystals are Be-rich, and arise from impurities in the melt. To avoid this type of crystal in the matrix, the preheat stage (up to $\approx$ 1200 K) is required, as noted in Chapter 2.

Fig. 3.25 is an optical micrograph of a porous SiC preform infiltrated with metallic glass. The light areas in the photograph are regions of metallic glass, and the dark areas are the preform. The small, very dark speckles are small

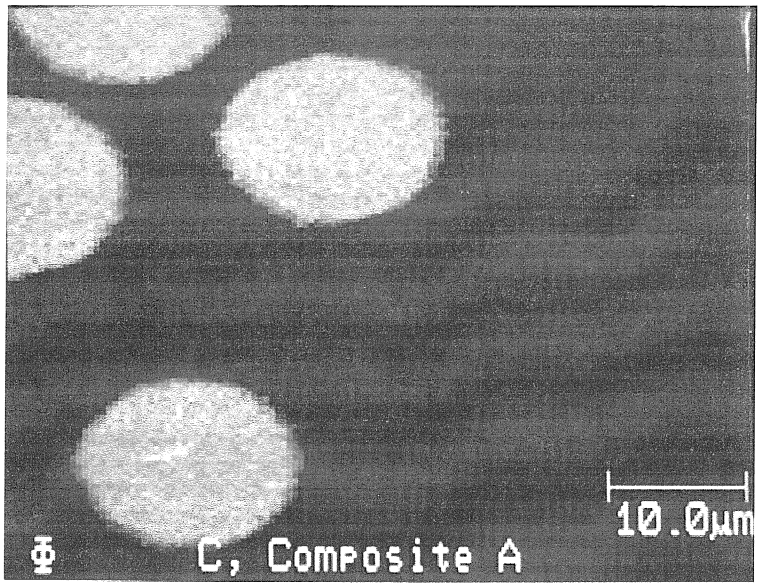

Fig. 3.22. Carbon compositional map for cross section of SiC/Vitreloy™ 1 composite. Image taken with SAM. Sample infiltrated for 0.5 h.

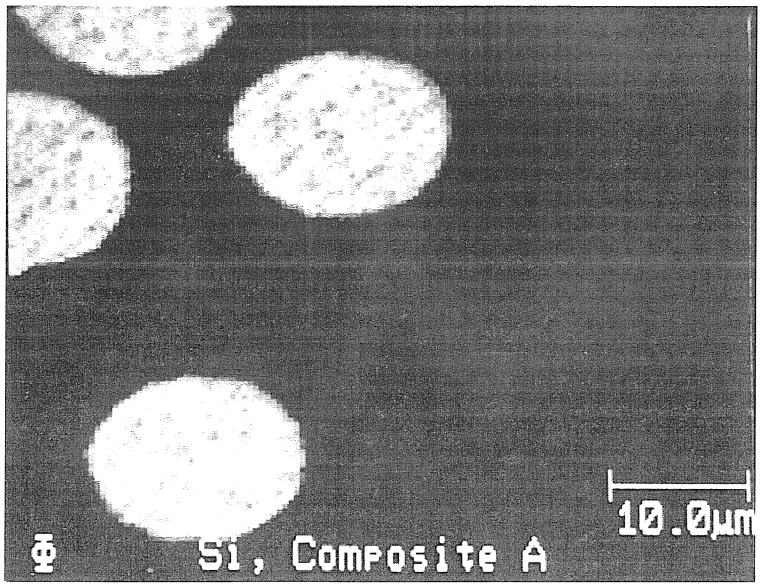

Fig. 3.23. Silicon compositional map for cross section of SiC/Vitreloy™ 1 composite. Image taken with SAM. Sample infiltrated for 0.5 h.

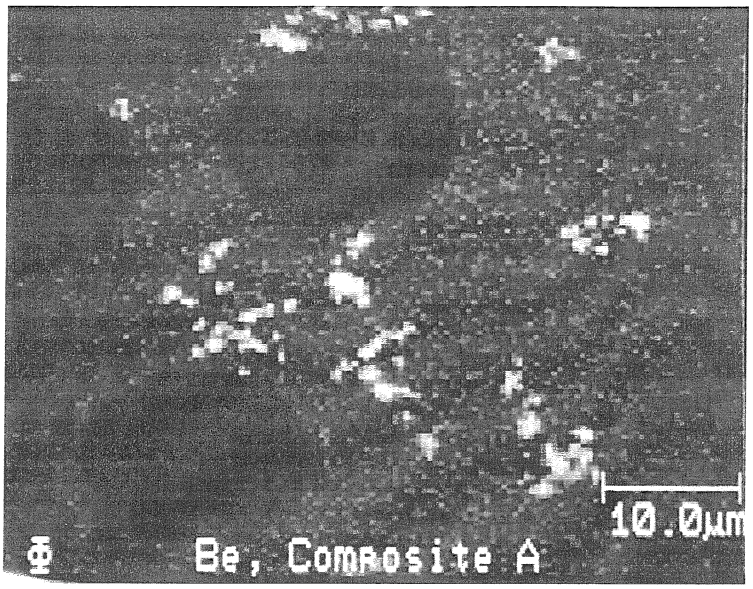

Fig. 3.24. Beryllium compositional map for cross section of SiC/Vitreloy™ 1 composite. Image taken with SAM. Sample infiltrated for 0.5 h.

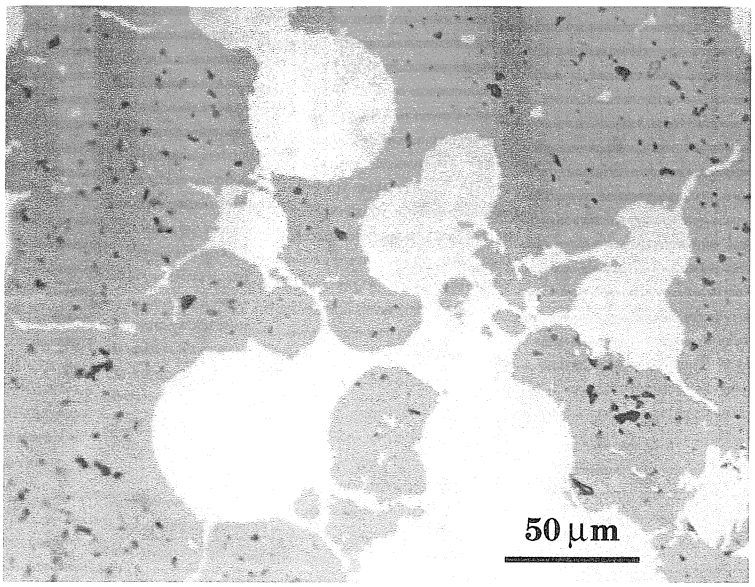

Fig. 3.25. Optical micrograph of SiC preform infiltrated with bulk metallic glass. Dark regions are SiC, light regions are amorphous metal.

pores in the preform which are closed off and unavailable to the matrix material. The preform is made of silicon carbide particles sintered to 60% density. Inspection of the micrograph shows full infiltration of the preform by the metallic glass and apparently a fully amorphous matrix. X-ray diffraction of this sample showed crystalline peaks only from silicon carbide. The sample was cast at 1098 K, and allowed to infiltrate for 5 minutes under a back pressure of argon gas. Note the extremely good wetting which has taken place; very fine details in the particulate preform have been filled by the metallic glass matrix.

As mentioned in the previous chapter, preliminary investigations also included making composite samples with a variety of metal wire reinforcements, many which were judged to be too reactive for further study. One interesting example is the composite sample reinforced with tantalum wire. Tantalum exhibits the rare combination of a high melting point (3287 K) and good ductility, both properties of interest in making metallic glass matrix composites. A composite rod of Vitreloy™ 1 and tantalum wires was cast isothermally at 1173 K; the wires were in contact with the melt for 10 min prior to water quenching. Fig. 3.26 shows an SEM micrograph of the wire/matrix interface in backscatter mode. The light area at the lower left of the image is the tantalum wire. There is a layer about 50 μm thick filled with eroded tantalum particles. Some of the tantalum is visible farther away from the interface, but the amount is small. The presence of tantalum in this interlayer was confirmed by EDS. Despite tantalum's high melting point, there was still significant reactivity with the alloy melt during processing. Clearly, the chemical compatibility between the matrix and other materials plays an important role in choosing a suitable reinforcement.

3.4 CONCLUSION

The amorphous-metal-matrix composites as processed had a mostly amorphous matrix. Crystallization of the matrix occurs preferentially on the interface of tungsten and steel wires. Some matrix crystallization occurs in the matrix away from wires, although not as frequently; the largest matrix crystals have the approximate composition $Be_{12}Zr_3TiNiCu$. There is more matrix crystallization in composite samples than in unreinforced samples made with identical processing. In neither tungsten nor steel wire reinforced samples was reinforcement material found in the largest matrix crystals. Hence, the crystallization is most likely due to heterogeneous nucleation on the surface of the wire or some contaminant on the surface. Carbides appear to be associated with crystallization near the interface in some cases, but not in others; the role of carbides is unclear. In silicon carbide reinforced samples, crystallization can occur by dissolution of excessive silicon into the matrix, changing the glass-forming abilities of the alloy.

In tungsten-reinforced composites, the electron diffraction patterns and the EDS data indicate that the interfacial reaction layer is composed of small tungsten crystals about 30 nm in diameter in an amorphous matrix. Tungsten composes about 10 to 20 atomic % of this interlayer depending on the distance from the interface. For processing conditions which held the wires and melt in contact for 30 min at 800 °C, the reaction layer was about 240 nm thick. In the composites with steel reinforcement wires, there was no detectable reaction layer in TEM, although SAM analysis suggests the formation of a carbide layer at the interface.

Other ductile reinforcement materials tested included tantalum and molybdenum, which were expected to perform well due to their high melting

points. The melting point of tantalum is 3287 K, and the melting point of molybdenum is 2890 K. Wire bundles of each of these materials were used as reinforcement for a composite sample. The wires were in contact with the melt for 10 minutes at 1173 K, and there was substantial reaction in both samples. The tantalum sample had a reaction layer approximately 50 μm thick with substantial erosion of the wire by the melt, and the molybdenum reinforced sample had a reaction layer about 10 μm thick, with large areas of crystallized material distributed throughout the melt. Similarly processed tungsten and steel reinforced composites did not show any reaction visible at this scale. Clearly, the chemical compatibility between the matrix and other materials plays an important role in choosing a suitable reinforcement.

An interesting comparison is between the interfacial layers formed in tungsten-reinforced composites (Fig. 3.9 and Fig. 3.14) and that of tantalum-reinforced composites (Fig. 3.26). We might initially expect a similar interfacial reaction, since both metals are extremely refractory. Although only SEM analysis was performed on the tantalum composites, it appears that crystals of tantalum were released into the matrix, which remained amorphous. This is basically what was found in the tungsten/metallic glass interfacial region. It is also visible on a larger scale in the tungsten-reinforced composites in Fig. 3.9. However, the tungsten reaction layer seen by TEM is 200 times thinner with proportionally smaller crystals compared to the tantalum. This certainly may be due to different chemical interactions between the reinforcement and the melt, or perhaps due to etching at surface features due to the drawing process of the wires. But it seems most likely that there is an attack on the grain boundaries of the reinforcement material. Analysis on the wire properties has not been performed, but the tantalum wire was larger diameter (500 μm) and

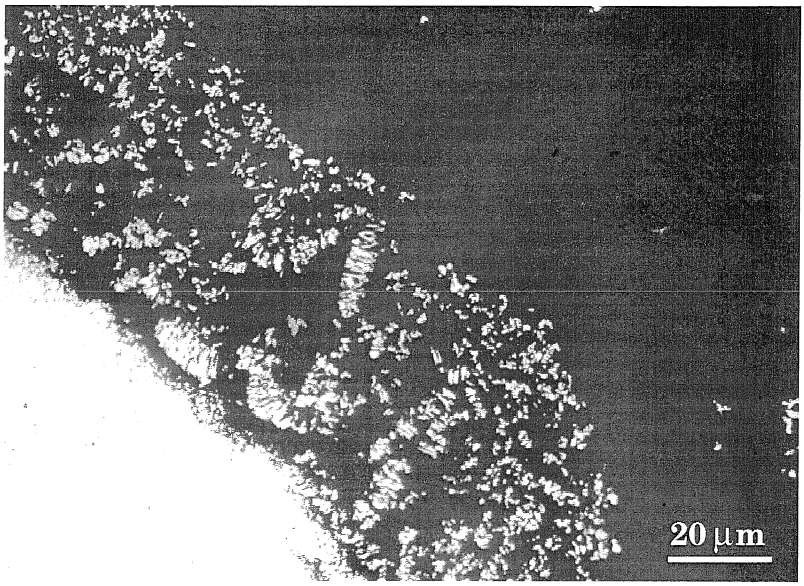

Fig. 3.26. SEM micrograph of composite interface. Light area at lower left is tantalum wire reinforcement, and dark area at upper right is metallic glass. Image taken with backscatter detector.

probably required much less drawing than the tungsten. Thus, we would not expect as finely refined a grain structure in the tantalum wire as in the tungsten wire. This could explain the different length scales observed in similar processes. In addition, Fig. 3.9 indicates that there is some dissolution of individual tungsten grains once they have been eroded from the wire. It appears that they reduce in size the longer they have been in contact with the melt.

These different pieces of evidence bring up at important point about comparing different types of microscopic analysis. It is nearly impossible to directly compare images of similar samples if different preparations are required. It certainly appears that different areas on the same reinforcement wire have different interfaces. Some appear to have crystallized reaction layers, while others do not. Analysis of many more samples seem to be needed to really get a good typical characterization.

A valuable direction of further study would be a systematic investigation to quantify the tolerance of the metallic glass to impurities. Use of an electrostatic levitator (ESL) would be ideal for such work. This technique is described in ref. 8. During composite processing by liquid infiltration, we would normally expect a small amount of reinforcement material to dissolve into the matrix. The quantity would depend on the matrix alloy, reinforcement material, duration of exposure, temperature of processing, and convection effects in the melt. Metallic glass alloys could be made with small known additions of other elements for testing in an ESL. The amount of undercooling could be measured for each impurity fraction, which would give a good indication of the glass forming ability of that alloy. In addition, recent work on the TEMPUS facility aboard MSL-1 has indicated that overheating the melt

plays an even larger role in achieving large undercooling than previously thought. More experimental data in this field would allow other improvements in processing to be made.

Another interesting area for future work would be the fabrication of bulk samples of similar composition and microstructure to the interfacial layer found in the tungsten-wire reinforced composites. Further investigations of the microstructure are warranted to confirm if in fact there are nanometer sized tungsten particles in an amorphous matrix. If this is the case, this material could have tremendous yield strength. It could basically provide a means to strongly bond together nanocrystalline tungsten without grain boundaries. This material could be produced by infiltrating and reacting ball-milled tungsten powder with metallic glass.

REFERENCES

1. NBS Monograph, 25, Standard x-ray diffraction powder patterns (Washington D.C., U.S. Department of Commerce/National Bureau of Standards, 1984).

2. S. Schneider, personal communication (1995).

3. C. S. Barrett and T. B. Massalski, *Structure of Metals*, Pergamon Press, Oxford (1980).

4. L. Xiao, Z. Fan, Z. Jinxiu, Z. Mingxing, K. Mokuang, and G. Zhenqi, *Physical Review B* **52**, 14, 9970-9978 (1995).

5. T. Iida and R. I. L. Guthrie, *The Physical Properties of Liquid Metals*, Claredon Press, Oxford (1988).

6. A. Masuhr, personal communication (1997).

7. W. L. Johnson, personal communication (1997).

8. W. K. Rhim, S. K. Chung, D. Barber, K. F. Man, G. Gutt et al., *Review of Scientific Instruments* **64**, 10, 2961-2970 (1993).

CHAPTER 4
KINETIC ENERGY PENETRATORS: A NOVEL APPLICATION OF BULK-METALLIC-GLASS-MATRIX COMPOSITES

4.1 TRADITIONAL KINETIC ENERGY PENETRATOR SYSTEMS

4.1.1 Background of Kinetic Energy Penetrators

Currently, a large portion of the defense industry dedicated to anti-armor applications are focused on using kinetic energy penetrators. These applications use only the kinetic energy of the projectile to defeat the target. The two primary families of materials used for this application are tungsten-based alloys, and depleted uranium (DU)-based alloys; other alloys have been excluded for reasons of high cost, limited availability, or inferior properties. DU is the U-238-rich by-product of the extraction of fissionable U-235 from uranium ore. Although DU cannot be used for nuclear fission, it still emits low-level radiation. Hence, "depleted" refers to the material's lack of the fissionable isotope rather than its lack of radioactivity. The best DU-based alloys outperform the best tungsten-based alloys by about 10% in penetrator performance.[1] As a result, DU kinetic energy penetrators are preferred for use by defense industries. Nevertheless, environmental concerns and related political pressure to stop using DU continues to spur research to find a way to improve the penetrator performance of tungsten-based alloys to match that of DU.

Significant work has been done to extensively characterize both DU and tungsten alloys in an effort to determine how to optimize penetrator performance. A number of mechanical and physical properties are considered essential for this application, such as high density and the optimum combination of hardness, strength, stiffness, and fracture toughness. High

density is required in order to focus the maximum kinetic energy for a given penetrator geometry. The design of penetrators is based on the idea of concentrating the most kinetic energy possible over the smallest area of the target. Thus, most penetrator designs are long-rod penetrators, which have a length to diameter (L/D) ratio of 10 to 20. High density is also important in reducing aerodynamic energy losses during flight and reducing flight time.[2] Alloys of DU and tungsten used in this application range in density from 16.2 to 18.6 g/cm^3.[1]

Unfortunately, it is unclear exactly how and which mechanical properties affect penetrator performance. A number of studies suggest that improvements in the quasi-static mechanical properties do not necessarily coincide with improvements in penetrator performance.[3-5] Penetration is an extremely high strain-rate event during which both the target and the penetrator undergo large amounts of deformation. There is an extremely large hydrostatic stress present at the penetrator-target interface, as shown in the diagram in Fig. 4.1. These data are from a computer simulation of a typical penetration event. Penetration continues until the penetrator is decelerated to a complete stop, the penetrator is completely eroded away, or the target is perforated.

The most salient difference between penetration tests of tungsten alloys and DU alloys is the behavior of the penetrator tip. Fig. 4.2 shows schematically the three different types of behavior during a penetration event. DU tends to slough off material as it penetrates due to its tendency to fail by adiabatic shear; the tip remains about the same diameter as the rest of the rod and stays sharp. The kinetic energy is thus focused over a smaller area of the target and the penetration depth is enhanced. This behavior is known as "self-

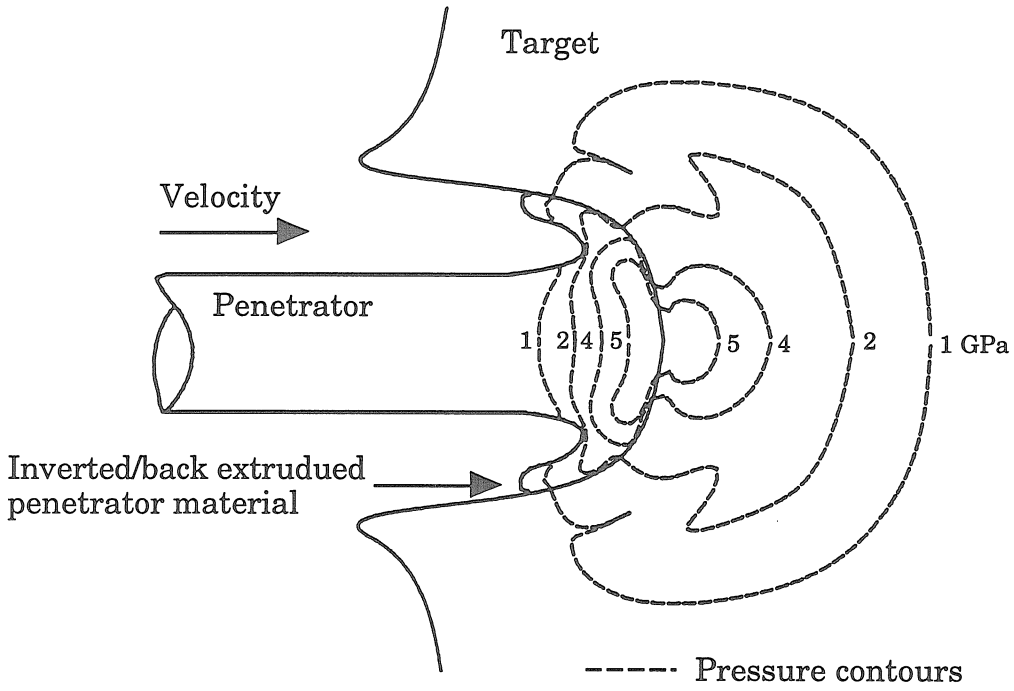

Fig. 4.1. Computer simulation of the penetration process of a long-rod kinetic penetrator into steel armor. Reproduced from refs. 1 & 6.

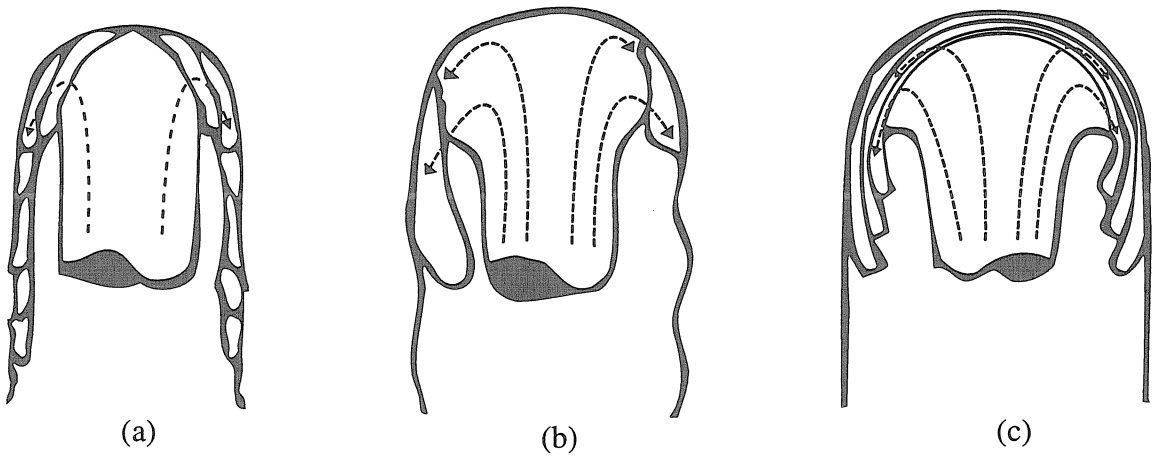

Fig. 4.2. Three types of penetration behavior for various materials that show (a) self-sharpening, (b) limited self-sharpening and (c) no self-sharpening ("mushrooming"). Reproduced from refs. 1 & 7.

sharpening." On the other hand, tungsten-based penetrators tend to expand and "mushroom" out, leaving a cavity of increasing diameter as deeper penetration is achieved. This is widely accepted to be the primary reason that DU exhibits superior penetrator performance. Some materials, such as certain tungsten heavy alloys (WHAs), exhibit a hybrid-mode behavior called limited self-sharpening.

4.1.2 Adiabatic Shear of Materials

The mechanism by which DU fails at high strain rates is known as adiabatic shear, or flow localization. In this failure mode, a material undergoes large shear strains confined to an extremely thin region. This thin region of deformation is known as a "shear band." Usually, this will occur on a plane of highest resolved shear stress. For a homogeneous material in uniaxial compression, this plane will be at 45° from the axis of compression. A large portion of the mechanical work put into deforming a material in this fashion goes to producing heat within the shear band. The speed of this process allows it to be called "adiabatic," since very little heat has been conducted away by the time the process has stopped.

There have been a number of investigations to determine which properties of a material influence its tendency to fail by propagation of shear bands. We can assume that for a material deformed under pure shear, the flow stress τ is a function only of strain γ, strain rate $\dot{\gamma}$, and absolute temperature T:

$$\tau = \tau(\gamma, \dot{\gamma}, T) \tag{4.1}$$

We can also assume that the condition which implies catastrophic shear is given by:

$$\frac{d\tau}{d\gamma} = 0 \tag{4.2}$$

Expanding the total differential, we find:

$$\frac{d\tau}{d\gamma} = \left(\frac{\partial \tau}{\partial \gamma}\right)_{T,\dot{\gamma}} + \left(\frac{\partial \tau}{\partial \dot{\gamma}}\right)_{T,\gamma} \frac{d\dot{\gamma}}{d\gamma} + \left(\frac{\partial \tau}{\partial T}\right)_{\gamma,\dot{\gamma}} \frac{dT}{d\gamma} = 0 \tag{4.3}$$

The three terms in the above equation represent the contribution from strain hardening, strain rate hardening, and thermal softening, respectively. The last term competes against the other two terms in trying to meet the condition required for catastrophic shear (Eqn. 4.2). Then, if we assume that at this high strain rate all of the energy of deformation goes into thermal energy, we can write:

$$\frac{dT}{d\gamma} = \frac{\tau}{C} \tag{4.4}$$

where C is the volume specific heat in $kJ \cdot m^{-3} \cdot K^{-1}$. Further, assuming that the strain rate is fairly constant, we find that the critical shear strain is given by:

$$\gamma_{critical} = -\frac{Cn}{\left(\partial \tau / \partial T\right)_{\gamma,\dot{\gamma}}} \tag{4.5}$$

when the relationship $\tau = \varepsilon \gamma^n$ holds for the relationship between the shear stress and shear strain (n is the strain-hardening exponent). This relationship was tested experimentally by Staker[8] on 4340 steel, and it was a good predictor of the onset of adiabatic shear band formation.

Another model described by Shockey[9] requires two critical conditions to be met for adiabatic shear band formation. They are:

1. $$\gamma > \gamma_{critical} = -\frac{nC_p}{\left(\partial \tau_y / \partial T\right)_{\gamma,\dot{\gamma}}} \tag{4.6}$$

2. $$\dot{\gamma} > \dot{\gamma}_{critical} = -\frac{2\alpha n K}{R^2 \left(\partial \tau_y / \partial T\right)_{\varepsilon,\dot{\varepsilon}}} \tag{4.7}$$

where τ_y is the yield strength, n is the work hardening exponent, C_p is the specific heat, and K is the thermal conductivity. R is a characteristic

specimen dimension, and α is a constant approximately equal to 2. Notice that Shockey's first condition is almost identical to that of Staker, with the yield strength replacing the flow stress.

Qualitatively, we see from Equations 4.5 through 4.7 that if we are to have adiabatic shear propagation, we want a material with low strain hardening, low strain rate hardening, and high thermal softening. In addition to these theoretical models, Dowding[3] found empirically through ballistic testing that adiabatic shear is encouraged in a matrix with elements with low melting points, low density, low crystal symmetry, and low average atomic numbers.

Numerous investigators have found that tungsten alone does not tend to fail by adiabatic shear during ballistic testing. In an attempt to take advantage of the high density of tungsten while encouraging adiabatic shear, the most common tungsten-based penetrator materials are metal/metal composites. Usually, a primary phase composed of packed tungsten particles is liquid-phase sintered together with a binder material. One of the most frequently used binder materials is an alloy of nickel and iron in the ratio of 7:3 in weight percent. Thus, a typical tungsten penetrator material is composed of 93 vol% W particles, with the remainder of the volume filled by an alloy of $Ni_{70}Fe_{30}$.[1]

Table 4.1 contains various physical and mechanical properties which have been found to influence the tendency to fail by adiabatic shear. The second column indicates the desired property to encourage adiabatic shear, as discussed above. The pertinent comparison is really between $Ni_{70}Fe_{30}$, the material commonly used as a matrix for tungsten composites, and Vitreloy™ 1, a potential replacement. Some data are not readily available and so a complete comparison is not possible. Nevertheless, Vitreloy™ 1 compares very favorably with $Ni_{70}Fe_{30}$ in all four categories shown in the table. In

Property	Better Adiabatic Shear	DU	$Ni_{70}Fe_{30}$	Metallic Glass-Vitreloy 1
Melting Point ($T_{liquidus}$, °C)	LOW	1132[10]	1441[11]	720[12]
Density (g/cm^3)	LOW	19.05 (α) 18.89 (β)	~8.6	6.1
Avg. Atomic Number	LOW	92	27.4	26.85
Thermal Conductivity ($W\ m^{-1}\ K^{-1}$)	LOW	28[10]	~87	3.5

Table 4.1. Comparison of various physical properties of penetrator materials.

addition, the $Ni_{70}Fe_{30}$ matrix is primarily a FCC phase; Vitreloy™ 1 is glassy, thus satisfying the condition for low crystal symmetry. Bruck[13, 14] found no strain hardening (n=0), and no strain rate hardening (m=0) in the Vitreloy™ 1 system. For most crystalline metals, the work hardening exponent n is in the range of 0.02 to 0.50, and the strain-rate sensitivity m is in the range of 0.0 to 0.1 at room temperature.[15]

It is not quite clear which temperature regime we should consider when comparing the thermal softening effect between the metallic glass and $Ni_{70}Fe_{30}$; however, investigators have shown that the viscosity of Vitreloy™ 1 follows a Vogel-Fulcher-Tamman relation:[16]

$$\eta = \eta_0 \exp\left(\frac{DT_0}{T - T_0}\right) \tag{4.8}$$

where η is the viscosity, T is the absolute temperature, D and T_0 are fitting parameters, and

$$\eta_0 = \frac{hN_A}{V} \tag{4.9}$$

where h is Planck's constant, N_A is Avogadro's number, and V is the molar volume. We also know from elementary fluid dynamics that the shear stress τ, viscosity η, and velocity gradient dv/dy can be related by:

$$\tau = \eta \frac{dv}{dy} \tag{4.10}$$

Thus, we might expect the flow stress to go linearly with the viscosity if we maintain a constant velocity gradient. Near the glass transition temperature of Vitreloy™ 1, the viscosity changes by 33% over a span of only 2 °C. For comparison, a commercially-used nickel alloy undergoes about a 20% decrease in its yield point upon heating from room temperature to 370 °C. We thus expect the thermal softening of Vitreloy™ 1 to also encourage adiabatic shear.

4.2 ADIABATIC SHEAR BANDING IN METALLIC GLASS AND METALLIC GLASS COMPOSITES

4.2.1 Failure Mode of Unreinforced Metallic Glass

Experimentally, from quasi-static mechanical testing, we know that Vitreloy™ 1, like most other metallic glasses, fails by adiabatic shear band formation. Fig. 4.3 shows a cylindrical sample of aspect ratio approximately 2:1 which was stressed in uniaxial compression along the axis of the cylinder until failure. The photograph shows that there is no perceivable deformation in the bulk of the sample. The sample failed along planes of maximum resolved shear stress at 45° to the applied compressive stress.

Fig. 4.4 shows an SEM micrograph of the fracture surface. The surface is covered with the characteristic "venous" pattern associated with metallic

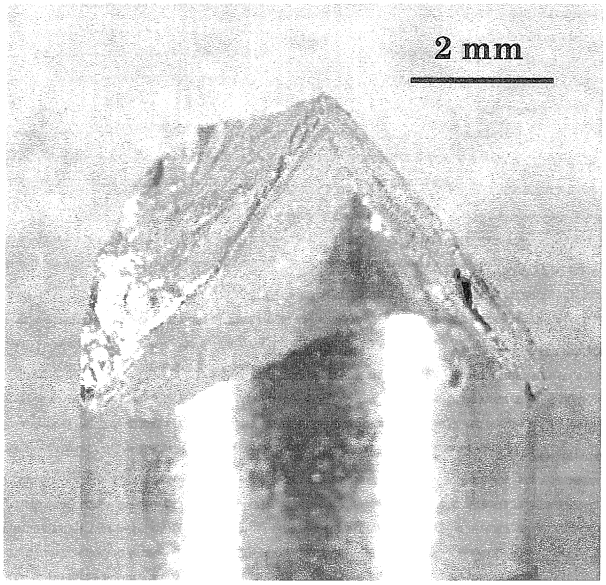

Fig. 4.3. Photograph of metallic glass (Vitreloy™ 1) cylinder after compressive failure. Applied stress was along axis of cylinder.

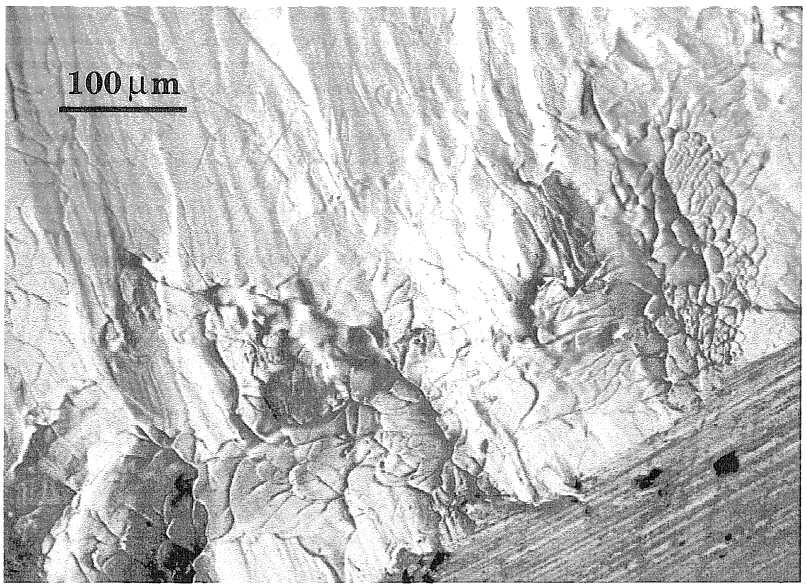

Fig. 4.4. SEM micrograph of fracture surface of metallic glass in compressive failure.

glass failures. The side of the cylinder is visible in the lower right corner of the micrograph. Figure 4.5 shows the stress-strain curve for this metallic glass sample. It is elastic up to 2% strain, and then fails with no appreciable global plastic strain. This type of stress-strain curve is typical of a material which fails in adiabatic shear. Bruck and coworkers[14] performed dynamic compression testing of Vitreloy™ 1 using the split Hopkinson bar apparatus. The results showed that at strain rates between 10^2 and 10^4 s^{-1}, the failure mechanism was also by adiabatic shear, virtually identical to results from quasi-static tests.

4.2.2 Quasi-Static and Low Strain-Rate Testing of Metallic Glass Matrix Composites

Quasi-static mechanical tests were performed on composites with a metallic glass matrix. The samples were reinforced by uniaxially aligned tungsten wires. The wires were 0.254 mm in diameter. Tests of the 20 vol% wire composites yielded fracture surfaces similar to unreinforced samples and with virtually no global plastic deformation. In the composite sample with 40 vol% wire reinforcement, the failure mode changed. The cylinder began to buckle and exhibited significant plastic deformation. It appears that shear bands were still propagating through the matrix, but global failure was being prevented by the presence of the reinforcement. Adiabatic shear was no longer the only mechanism by which the sample was deforming. For this strain rate, there appears to be a critical volume fraction of reinforcement between 20 and 40 vol% required for failure along a single adiabatic shear band.

Further compression testing was performed at higher strain rates using a Hopkinson bar apparatus. Here, strain rates achieved were on the order of

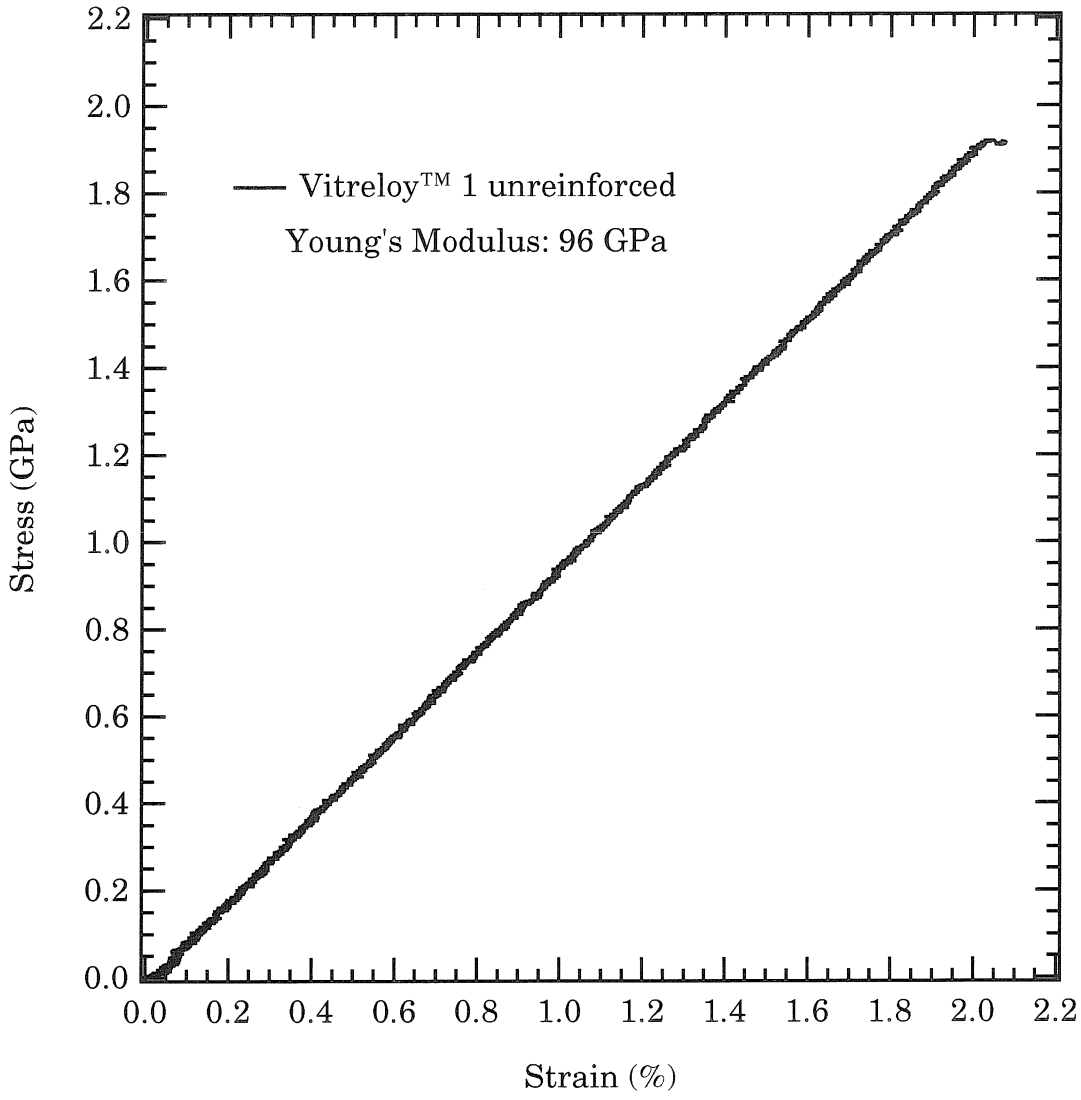

Fig. 4.5. Stress-strain curve of unreinforced metallic glass cylinder in quasi-static compression.

10^2-10^3 s^{-1}. Again, samples with lower percentages of wire reinforcement tended to fail along a plane at about 45° to the applied stress by adiabatic shear, while samples with higher volume fractions of reinforcement tended to fail by axial splitting. However, the volume fraction for which this transition occurs is different than for the quasi-static case. In this series of tests, the 60 vol% reinforcement samples showed evidence of failing in shear, while the 80 vol% sample did not. The failure surface for the 60 vol% tungsten wire sample is shown in Fig. 4.6. Again, the micrograph shows the same characteristic venous pattern on the surface, in addition to wires which have been sheared off. Note, however, that the metallic glass matrix has been smeared over the surface of the sheared reinforcement. Clearly, this smearing occurred after the wires had sheared through. The liquid-like appearance of this surface indicates that there could be a local drop in the viscosity of the metallic glass matrix, perhaps precipitated by an extreme temperature increase from the local deformation.

These mechanical tests indicate that catastrophic shear failures become the preferred mechanism at higher strain rates, even in samples with a large volume fraction of reinforcement.

4.3 PROCEDURE FOR BALLISTIC TESTING

Evidence from quasi-static and limited dynamic testing of metallic glass and metallic glass matrix composites was very promising. There is evidence to indicate that as strain rates increase, adiabatic shear becomes more pronounced and could possibly be the preferred mechanism of failure in composites with only small volume fractions of metallic glass. To further

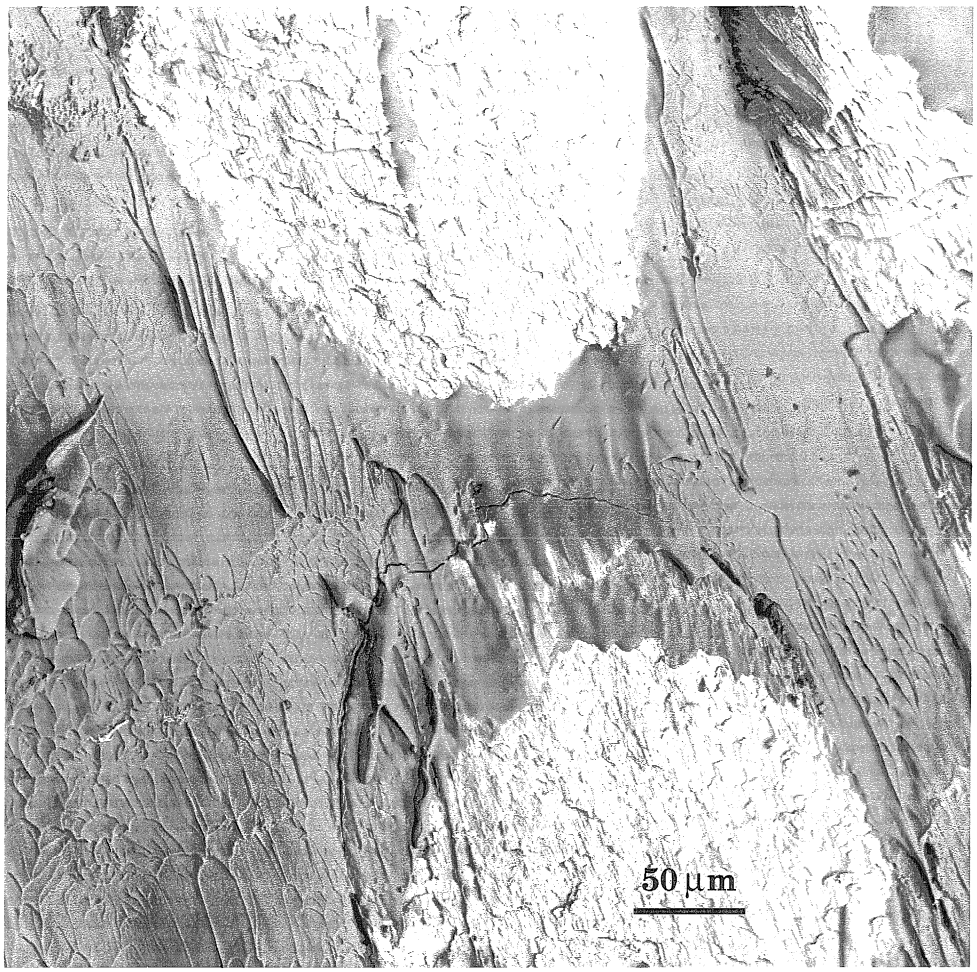

Fig. 4.6. SEM micrograph of failure surface of 20 volume percent tungsten-wire-reinforced Vitreloy™ 1 composite. Sample failed on single shear band under dynamic axial compression on a Hopkinson bar apparatus.

investigate the high strain-rate behavior of the composites, ballistic tests were performed; the experimental technique is described in this section.

Two types of testing were performed: reverse ballistic and forward ballistic. Both were intended to test the penetrating capabilities of tungsten-wire-reinforced metallic-glass-matrix composites. Both used an enclosed cannon at the California Institute of Technology. A schematic of the cannon is shown in Fig. 4.7. The cannon has a smooth-bore barrel which is 3.05 m in length and 35 mm in inner diameter. Acceleration of the projectile is provided by a hot-wire ignited gunpowder charge. The velocity of each shot is primarily controlled by the mass of the projectile, as well as by the mass and type of gunpowder used. Each type of gunpowder burns at a different rate; generally more finely divided powder burns more quickly and provides a higher final velocity. At the exit end of the barrel, there are two fiber-optic light sources separated at a known distance. Each is directly across from two other fiber-optic cables attached to optical sensors. The time between when each light path is broken is measured, and the velocity is calculated.

The projectiles were carried down the barrel in a nylon sabot, which is machined to a slip fit inside the barrel. The sabot, made of a relatively soft material, protects the barrel from damage during a shot, keeps the majority of rapidly expanding gasses behind the projectile during flight down the barrel, and stabilizes the projectile against tumbling.

4.3.1 Procedure for Reverse Ballistics

Initial testing was performed using reverse ballistics; that is, the penetrator was held stationary at the exit end of the barrel, and a flyer plate was attached to a sabot with epoxy and used as a projectile. This test was performed

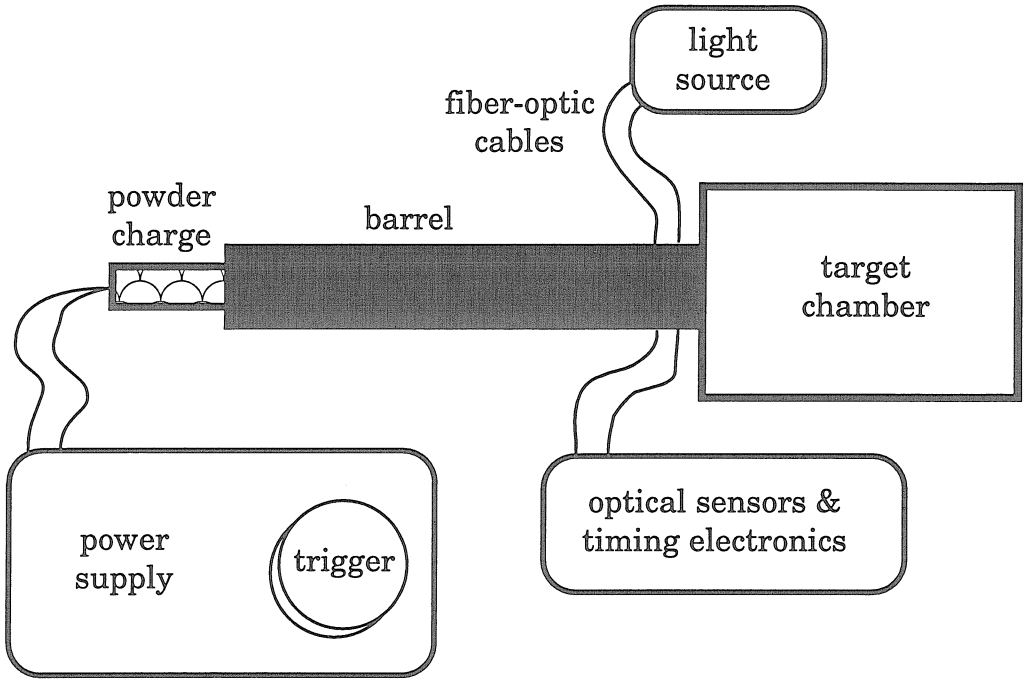

Fig. 4.7. Schematic of cannon used for ballistic testing.

initially because many of the gun parameters were already calculated for this configuration. The flyer plate was a circular disk of 0.983 cm thick C200 maraging steel. The plate was 3.152 cm in diameter, with a mass of 60.13 g. The steel was aged at 490 °C for 6 h; the reported mechanical properties for this alloy and heat treatment is yield strength of 1400 MPa, tensile strength of 1500 MPa, 10% elongation, and a fracture toughness in the range 155-200 $MPa \cdot m^{1/2}$.[17] The mass of the sabot was 24.07 g, so the total mass of the flyer plate plus the sabot was 84.20 g. The composite rod was a circular cylinder with a flat end; it was glued with epoxy into a steel mounting block with a countersunk hole. The rod was 0.635 cm in diameter, 25.38 g, 4.71 cm long, with 3.53 cm of exposed length. A schematic of this test configuration is shown in Fig. 4.8.

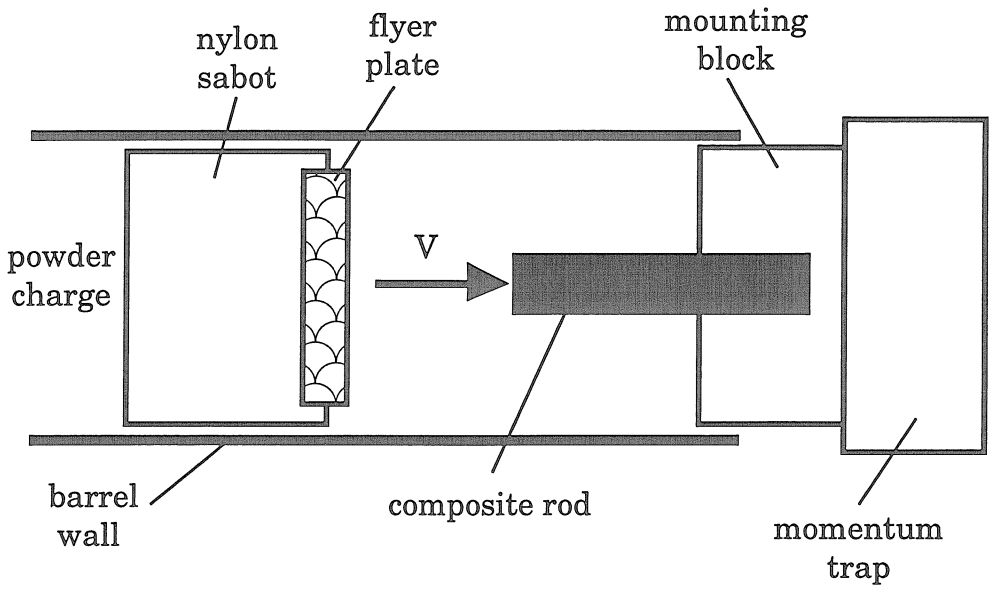

Fig. 4.8. Reverse ballistic schematic.

Only one successful test was performed in this configuration. Sufficient gunpowder was used so that the predicted velocity for this flyer mass was 1000 m/s; however, there was an error in the velocity measurement circuit during this test, so the exact speed is not certain. The composite was 80 vol% uniaxially aligned tungsten wire in a Vitreloy™ 1 matrix. The wires were 254 μm in diameter, and the composite was fabricated as detailed in Chapter 2. However, the Vitreloy™ 1 used for composites in the ballistic tests was provided by Amorphous Technologies International (Laguna Niguel, CA). The rod used in this test was a right circular cylinder; however, since the rod was solidly mounted, only a portion of the rod was exposed and available for penetration. Behind the steel mounting block was the momentum trap, an arrangement to absorb the shock of the impact. This test was also done with the barrel under rough vacuum to maintain the same testing parameters from previous experiments, although this is not necessary for the test.

4.3.2 Procedure for Forward Ballistics

In order to better simulate what an actual penetrator would experience during impact, we also tested the composite in a forward ballistic arrangement. For these tests, the penetrator was mounted in a sabot and fired at a target. This testing configuration is shown in Fig. 4.9.

Two different target materials were used. The first was an aluminum (6061 T651) cylinder aligned along the axis of the barrel. The aluminum targets were cut from a 15.2 cm (6 inch) diameter billet, and 15.2 cm thick. The second type of target was a 15.2 cm (6 inch) diameter 4130 steel. The steel targets were 10.2 cm (4 inches) thick, and heat treated to a hardness of 24 to 37 on the Rockwell C scale (HRC). Unfortunately, there was some inconsistency in the heat treatment of the steel targets, and the hardness varied from the target impact surface to the back surface over values differing by 10 or more on the Rockwell C scale. A number of tests were already performed when this was discovered, so the hardness is not consistent through the different targets. Nevertheless, our experimental data suggest that this does not create a large error.

The target was chained down to a V-block, and braced from behind by a heavy spring to act as a momentum trap. Special care was taken in aligning the block so that the composite rod impacted normal to the face of the block; the yaw for all tests reported here is 0°. Aluminum was chosen for greater penetration depth and deeper embedding of the penetrator; the penetrator would remain intact after the impact, and the behavior of the composite during the event could be studied more accurately. Steel is a better approximation for armor commonly found in real-world applications.

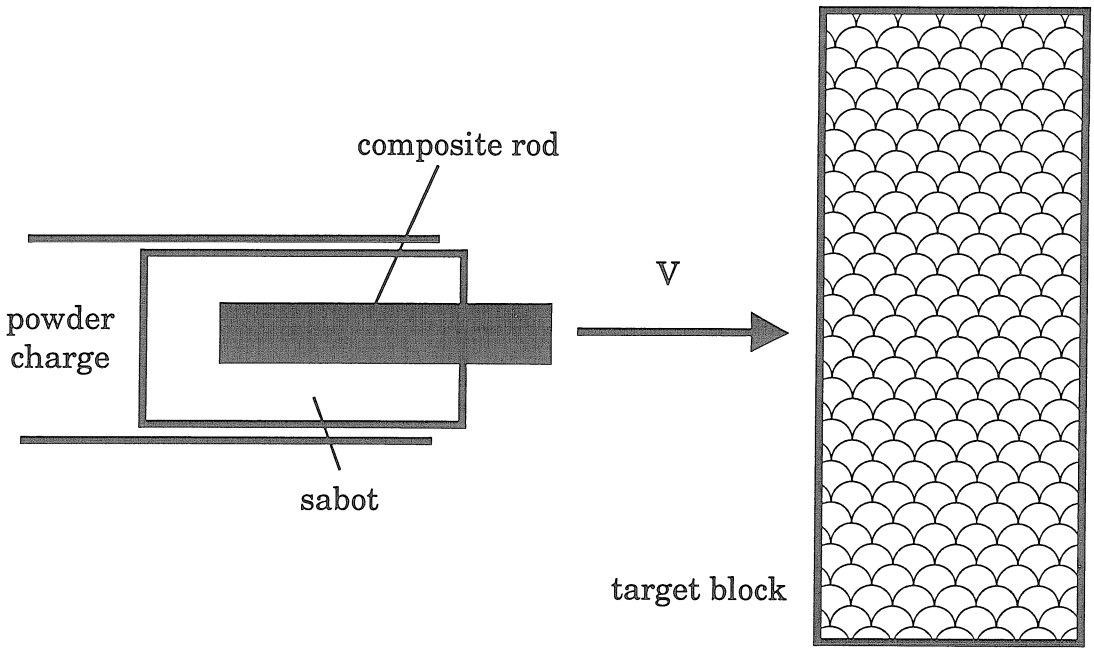

Fig. 4.9. Forward ballistic schematic.

The sabot used was longer than the one for reverse ballistics. Initially, a short sabot was used, but there were problems with stability of the rod. A number of shots using a slightly different configuration resulted in no penetration due to tumbling of the penetrator prior to impact. For tests into aluminum targets, the composite rods were 3.81 cm (1.5 inch) long, and 0.635 cm (0.250 inch) in diameter; thus the length-to-diameter ratio (L/D) was 6. For the tests against steel targets, the rods were 5.08 cm (2 inches) long and 0.635 cm (0.250 inch) in diameter; for these tests, L/D=8. The density of the composites was 17.3 ±0.2 $g \cdot cm^{-3}$. The variation in density was due to the variation in the exact fiber fraction for each piece.

The sabot remained with the penetrator until impact; it was not stripped away during flight. The sabot encased 3.05 cm of the penetrator, so that a significant portion of the rod was left exposed beyond the length of the sabot in order to allow penetration to begin before the sabot impacted the target. As in

the previous tests, the composite rod was a right circular cylinder with flat ends.

A C200 steel backing plate was added to the nylon portion of the sabot for forward ballistic testing. Later, a 17-4 hardened stainless steel was used. The particular alloy was not essential, as long as it was strong enough to support the penetrator rod during acceleration. A schematic of the sabot is shown in Fig. 4.10. The nylon portion of the sabot was split into two parts. The rear part was bored out to allow the backing plate to sit flush inside it. Then, the front nylon portion of the sabot was drilled out to a slip fit with the rod and inserted into the rear portion. It was determined that without the backing plate, during the acceleration of a shot, the rod would punch through the nylon behind it. The backing plate was made thick enough so that the composite rod would not deform it significantly during acceleration. Even if the rod only dented the backing plate, it was enough to skew the penetrator off axis and create tumbling before impact.

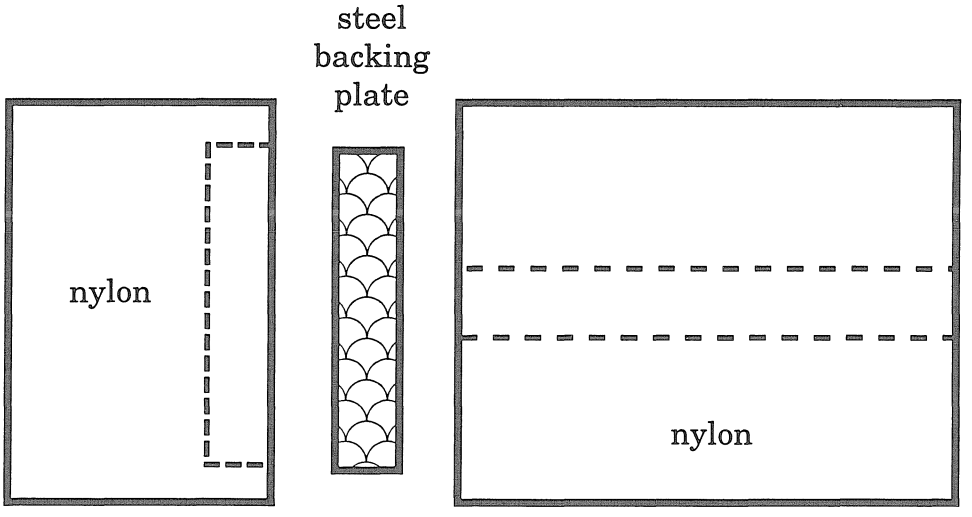

Fig. 4.10. Sabot for forward ballistics.

Another change in the forward ballistic testing configuration was the free flight of the projectile before striking of the target. There was approximately a 12 cm gap between the end of the barrel and the face of the target. At these high velocities, it did not present a stability problem; the distance of free flight did not allow sufficient time for tumbling to occur. As in the reverse ballistic tests, the forward ballistic tests were performed under rough vacuum.

The WHA penetrators used with steel targets were the same dimensions as the composite penetrators; that is, 5.08 cm (2 inches) long and 0.635 cm (0.250 inch) in diameter with L/D=8. This removes any effects from different penetrator sizes or aspects ratios in the results for these tests. The WHA used is designated X-27C and is produced by Teledyne Firth Stirling. Selected properties of this alloy are shown below in Table 4.2. The samples used were provided by R. J. Dowding of the Army Research Laboratory at Aberdeen, MD, and are used as a standard material for ballistic testing.

Property	X-27C
Composition (wt %): Tungsten	90.73
Nickel	4.55
Iron	1.97
Cobalt	2.75
Density (g/cc)	17.45
Ultimate Tensile Strength (ksi)	171
Elongation (%)	11.9

Table 4.2. Selected properties of the tungsten heavy alloy X-27C.[18]

4.4 RESULTS

4.4.1 Results of Reverse Ballistic Testing

After the shot, the steel mounting block, penetrator, and flyer plate were fused together. To analyze the penetration behavior, they were cut along their cylindrical axis, and the photograph in Fig. 4.11 was taken. In Fig. 4.11, the penetrator is upright in the center of the photo, and the flyer plate is on top. The sabot melted and disintegrated upon impact. The large horizontal crevice separates the flyer plate from the steel mounting block. Extensive deformation from the impact is visible at the outer edges of the flyer plate. Also, a hole in the middle of the flyer plate from the penetrator is visible. Following cutting, enough stresses were relieved that the pieces could be separated. A top view of half of the flyer plate alone is shown in Fig. 4.12. In this photo, the hole is more obvious, although some debris still obscures it slightly.

The most important part of Fig. 4.11 to notice is the shape of the penetrator tip. The tip appears to come to a point, and is indicative of self-sharpening behavior. In addition, the hole in the flyer plate appears to be approximately the same diameter as the original penetrator diameter; this indicates that there was no mushrooming of the penetrator head during impact. These results imply that the composite undergoes self-sharpening behavior, but they are not conclusive.

4.4.2 Results of Forward Ballistics into Aluminum Targets

Four successful shots into aluminum targets were made using forward ballistics, all at different velocities. Following the shot, the aluminum block was cut axially around the penetrator, and then split open to avoid cutting into

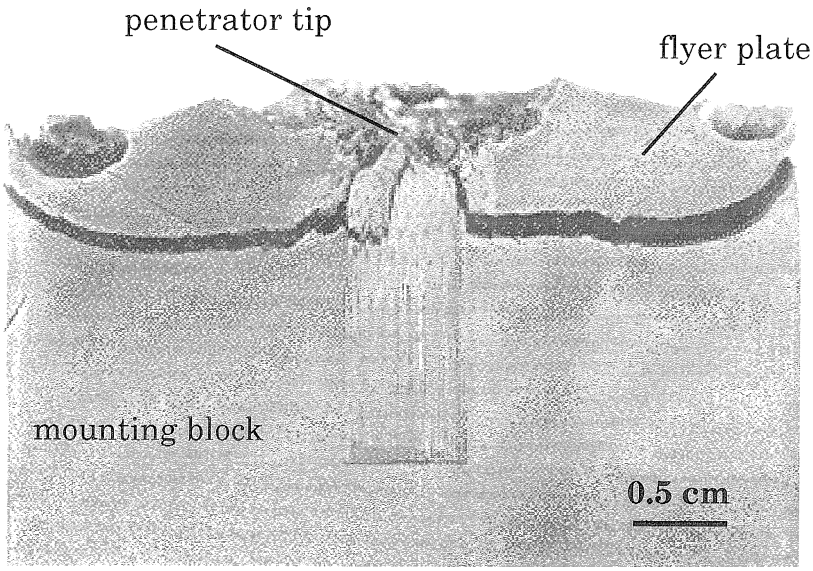

Fig. 4.11. Photograph from reverse ballistic testing of tungsten wire reinforced metallic glass composite: cut-away view of penetrator and flyer plate following reverse ballistic test.

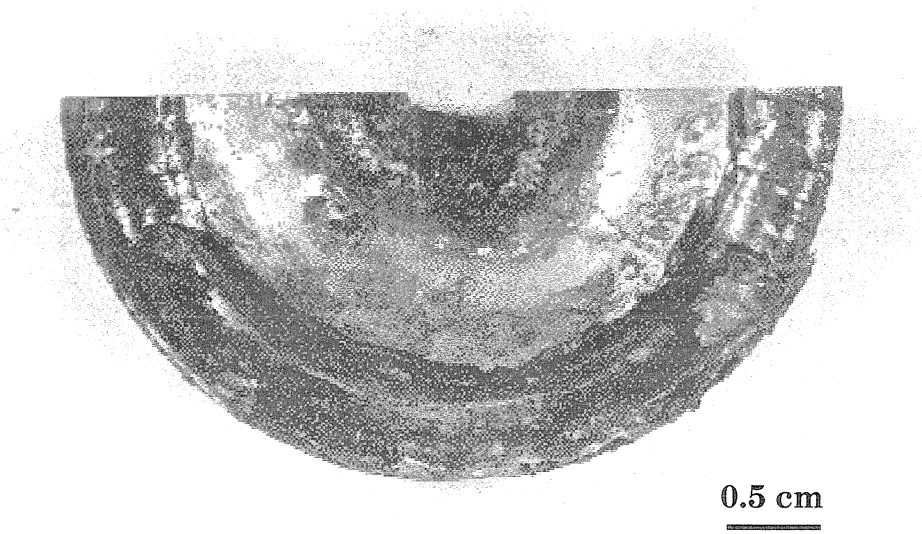

Fig. 4.12. Photograph from reverse ballistic testing of tungsten wire reinforced metallic glass composite: top view of half of flyer plate following reverse ballistic test. Hole from penetrator is visible at top middle of plate.

the penetrator or the penetration path in the target.

Fig. 4.13 shows the embedded penetrator in the aluminum target for a shot at 605 m/s. In all penetrator photographs, the initial impact between the rod and target occurred on the left side, and as the penetration occurs, the rod traveled to the right through the target material. Note the tip of the penetrator is chiseled down to a sharp point, despite starting with a flat head. The flat rear end of the penetrator rod is visible about halfway down the tunnel. Also note the constant diameter of the hole bored out by the penetrator. There is a slight indentation on the entry surface of the target from the impact of the sabot and the backing plate. The rectangular light areas to the right of the penetrator tip are artifacts from the cutting open of the block. The portion of the target immediately around the penetration tunnel appears lighter and rougher because it was split by force rather than cut.

Fig. 4.14 shows the embedded penetrator in the aluminum target for a shot at 749 m/s. Also, this photograph is only of one quarter of the target block; two cuts had to be made to actually find the tip of the penetrator. Thus, the penetration tunnel appears smaller than it actually is. Again, the tip of the penetrator is chiseled down to a sharp point. The penetration channel is not as smooth as the previous case, but there is still no evidence of mushrooming of the head. Significantly more of the penetrator has been eroded away, as we expect for the higher velocity. In addition, near the end of the penetration, the rod began to travel off axis. This probably reduced the total penetration depth in this sample, and is not surprising that the stability against yaw is reduced when the penetrator has been eroded down to a short rod. Penetration studies using a tungsten-heavy-alloy rod showed similar results in a number of cases; these tests will be further discussed later in this section. The penetrator is less

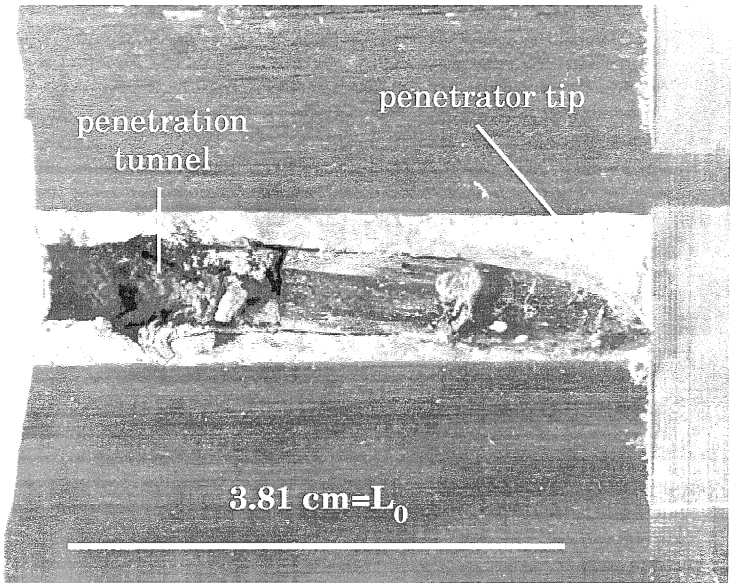

Fig. 4.13 Photograph of composite penetrator embedded in aluminum target block. Shot in forward ballistic configuration at 605 m/s. L/D=6. P/L=1.29.

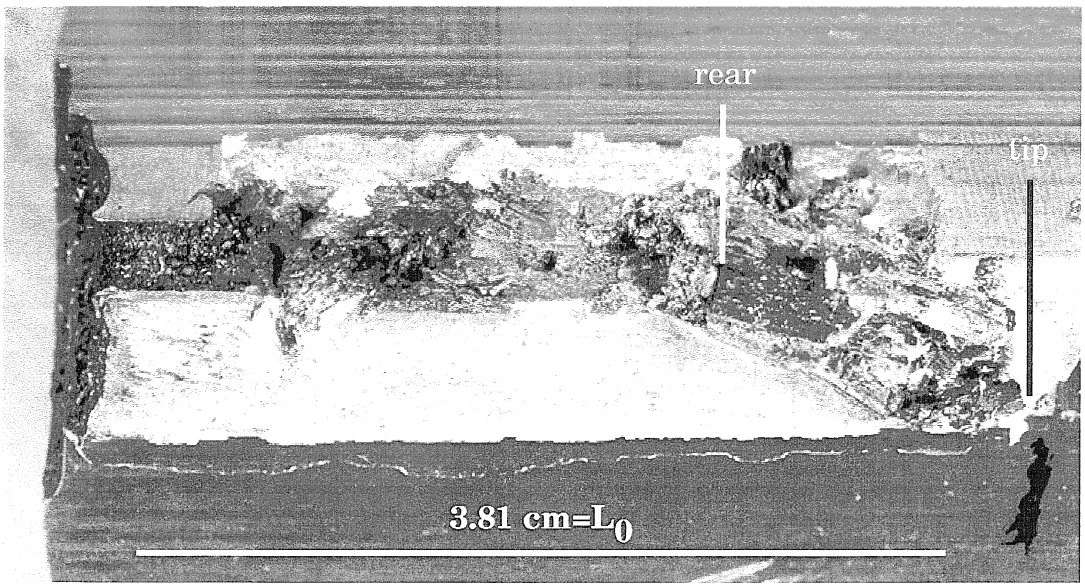

Fig. 4.14 Photograph of composite penetrator embedded in aluminum target block. Shot in forward ballistic configuration at 749 m/s. L/D=6. P/L=1.21.

intact than for the previous case, probably because of the higher velocity and the greater amount of yaw during penetration.

Fig. 4.15 is a photograph of penetration of a composite rod at 1032 m/s into an aluminum target. Again, the penetrator tip is sharp, and some tilting off-center has occurred, but it appears only at the end of the penetration. Note that the rod is almost completely eroded away; the back of the rod can be seen about 7/8 of the way down the penetration tunnel. Small bits of the penetrator can be seen embedded in the side of the tunnel.

Fig. 4.16 shows a rod fired at 1257 m/s. Virtually all of the penetrator has been eroded away; a small bit can be seen at the very bottom, and it has tilted at the very end of penetration so that it sits almost 90° from its entry angle. A substantial crater is visible from the sabot, as well as an even deeper one from the backing plate. The penetration channel is not as clean and smooth as for the lower velocity shots. In fact, about halfway down the channel, there are four large gouges approximately evenly spaced around the axis. In each of the gouges is a significant amount of composite material. It appears that outer portions of the penetrator split off at this point, and the inner core continued to burrow deeper. Judging from the amount of penetrator left from this sample, this is probably very near the maximum penetration depth achievable with this initial rod length; increasing the velocity will not be effective with no penetrator left intact.

As a comparison, Fig. 4.17 shows the penetration of a rod of the tungsten heavy alloy (WHA) W-$Fe_{5.6}$-$Ni_{1.4}$ into an aluminum target. This sample was one of a number of tests performed by Sunil Yadav at Caltech. The behavior of the tip is clearly different than that of the composite penetrators. The tip of the embedded penetrator is much larger than it was initially, and extremely

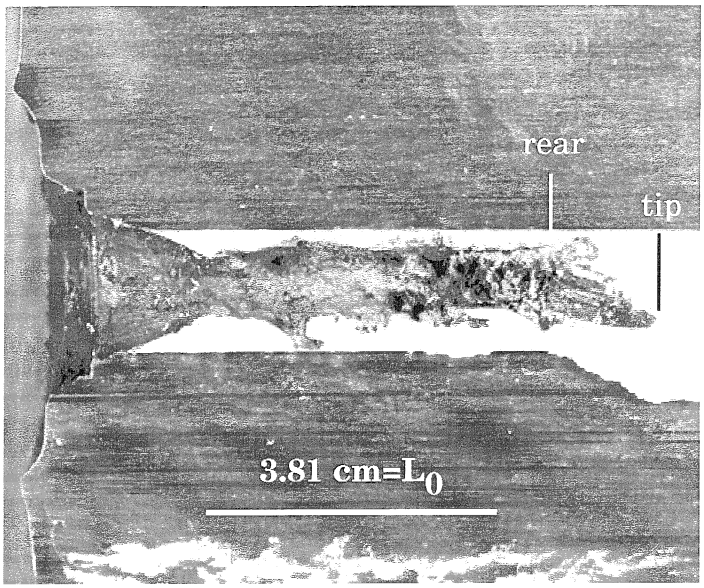

Fig. 4.15. Photograph of composite penetrator embedded in aluminum target block. Shot in forward ballistic configuration at 1032 m/s. L/D=6. P/L=2.17.

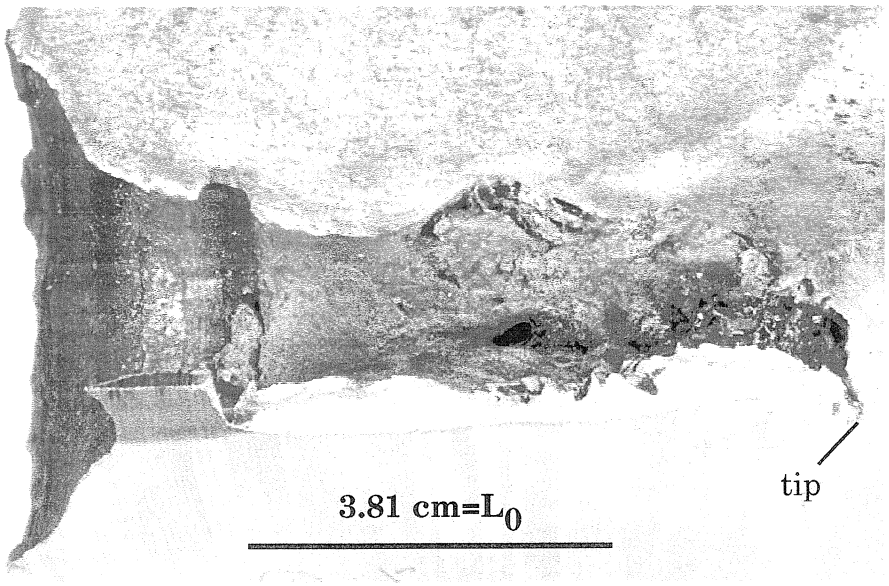

Fig. 4.16. Photograph of composite penetrator embedded in aluminum target block. Shot in forward ballistic configuration at 1257 m/s. L/D=6. P/L=2.33.

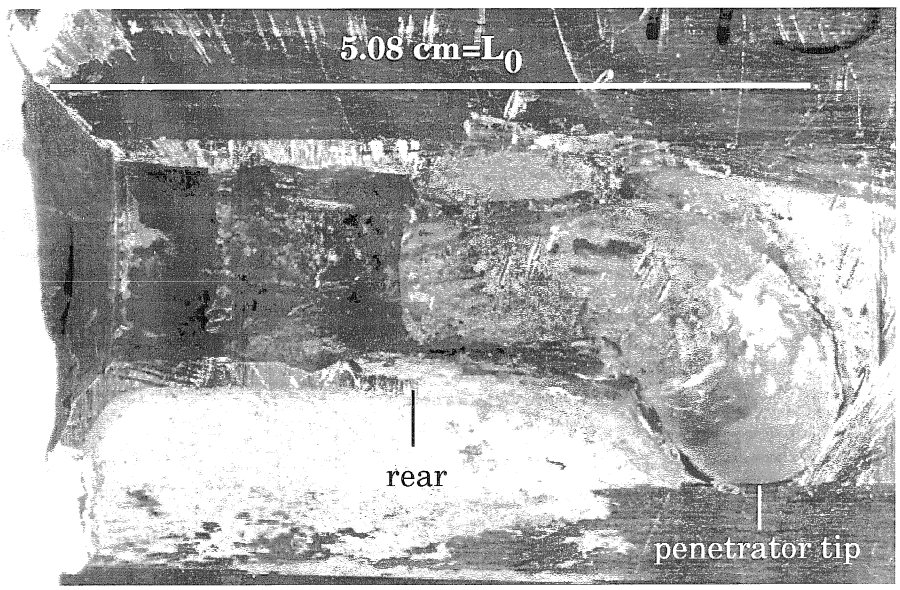

Fig. 4.17. Photograph of WHA (W-$Ni_{5.6}$-$Fe_{1.4}$) penetrator embedded in aluminum target block. Shot in forward ballistic configuration at 694 m/s. L/D=6. P/L=1.06. Test was performed by S. Yadav.

rounded. The test parameters were nearly identical, although the WHA rods were 2.0 inches long, and 0.33 inches in diameter. They, like the composite rods tested, have a L/D of 6, and were shot at a number of comparable velocities, so they can still provide a basis of comparison. For rods of the same L/D, we can calculate a normalized penetration depth, which is the penetration depth divided by the initial length. Fig. 4.18 shows a graph of the normalized penetration depth of the composite rods and the WHA rods. Linear fits have been made for each, and are also shown on the graph. The fit for the composite is significantly higher than that of the WHA.

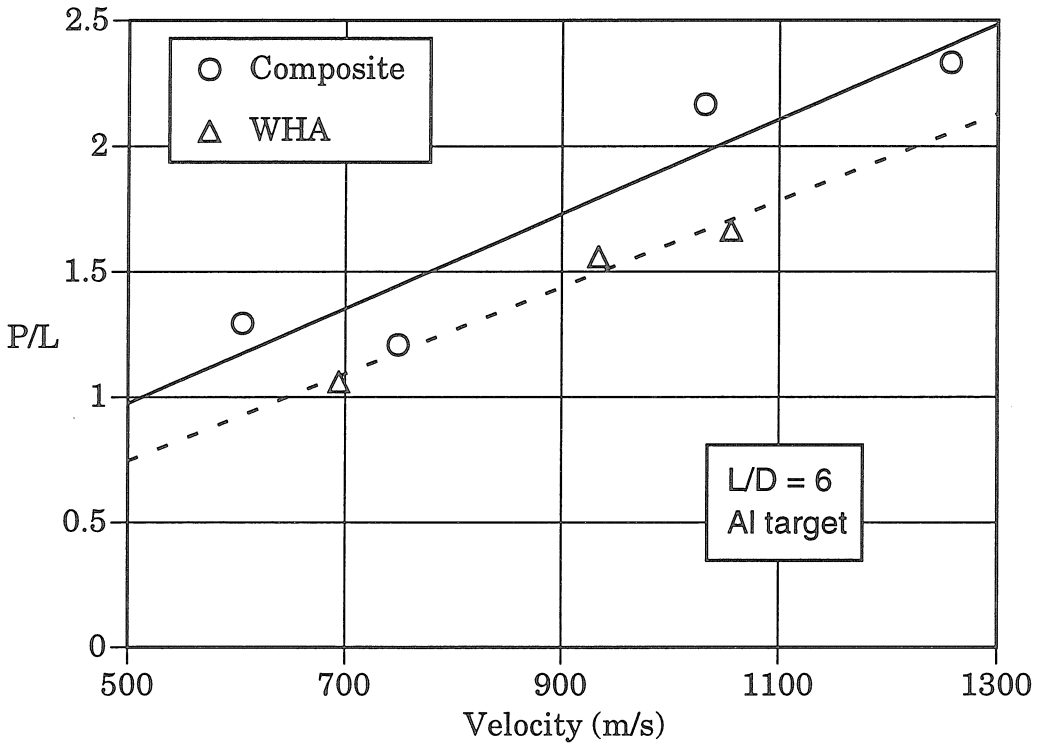

Fig. 4.18 Penetration efficiency versus impact velocity. Target was aluminum (6061 T651). Penetrators used were flat-ended rods with L/D=6. Composite was 80 vol% uniaxial tungsten wire in a metallic glass matrix. WHA was the liquid-sintered tungsten heavy alloy with composition in weight percent of $W_{93}Ni_{5.6}Fe_{1.4}$. WHA experiments by S. Yadav.

4.4.3 Results of Forward Ballistics into Steel Targets

Three shots of metallic glass composite penetrators and three shots of WHA penetrators were successfully performed into steel targets. The targets with the embedded penetrators were cut open by a combination of electrical discharge machining (EDM) and band sawing. EDM was used on the penetrator itself to minimize damage during cutting.

Fig. 4.19 is a photograph of a steel target after impact with a metallic glass composite rod. The penetrator was shot at 760 m/s. The penetration was quite shallow, as we would expect for such a low velocity and hard target material. The penetrator did not even remain embedded in the target. Fig. 4.20 shows the results of a similar test with an impact velocity of 956 m/s. The head of the penetrator has not mushroomed extensively, although it is not as clearly self-sharpening as in the case with the aluminum targets; the tip has expanded to only about 1.5 times its initial diameter. Near the tip, a line along the penetrator at about 45° from its axis is visible where the wires in the rod begin to bend over to be sloughed off. Fig. 4.21 shows a test performed at 1253 m/s. Again, the tip is only about 1.5 times the original diameter. The striated appearance of the tunnel is due to the lining of tungsten wires. It appears that the wires in the outer layer of the penetrator get bent around 180° and are left nearly intact on the wall of the tunnel.

For comparison, the next three figures show the results of the shots made with penetrator rods of X-27C WHA. Figs. 4.22, 4.23, and 4.24 show photographs of WHA penetrators fired at various velocities. The tips are larger and mushroom out more noticeably than in the composites, creating wider tunnels through the target. Correspondingly, the normalized depth is less than for the composite penetrators. In Fig. 4.24, the head of the penetrator

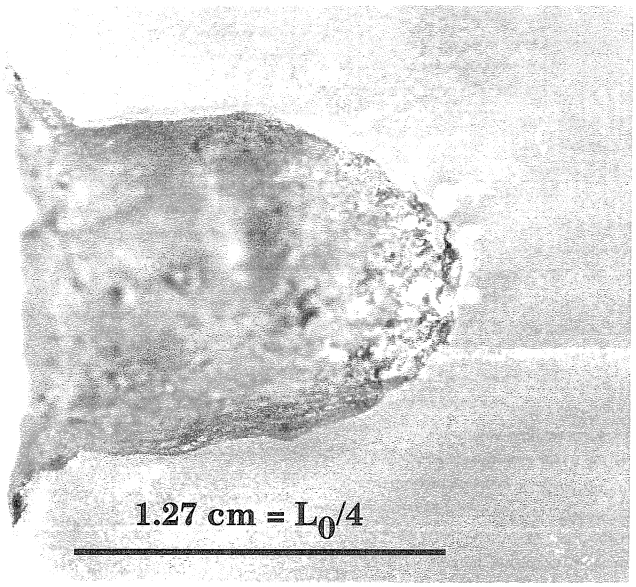

Fig. 4.19. Photograph of metallic glass matrix composite penetrator in 4130 steel target. V=760 m/s, L/D=8, and P/L = 0.312.

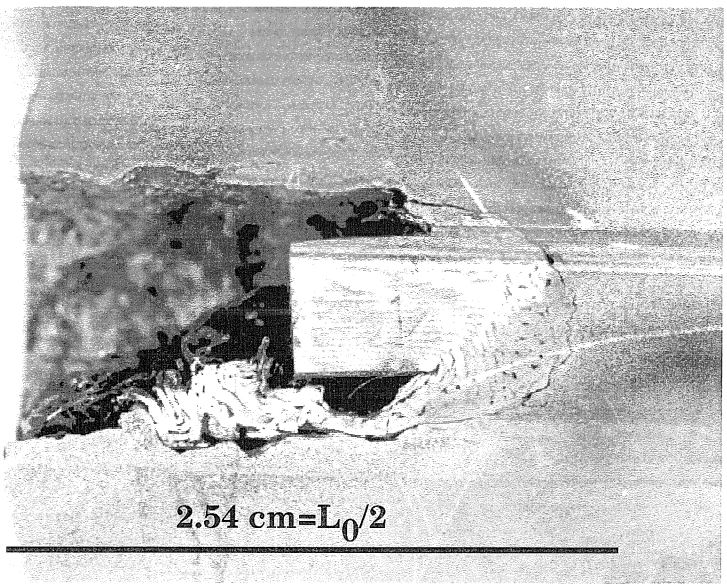

Fig. 4.20. Photograph of metallic glass matrix composite penetrator in 4130 steel target. V=956 m/s, L/D=8, and P/L = 0.469.

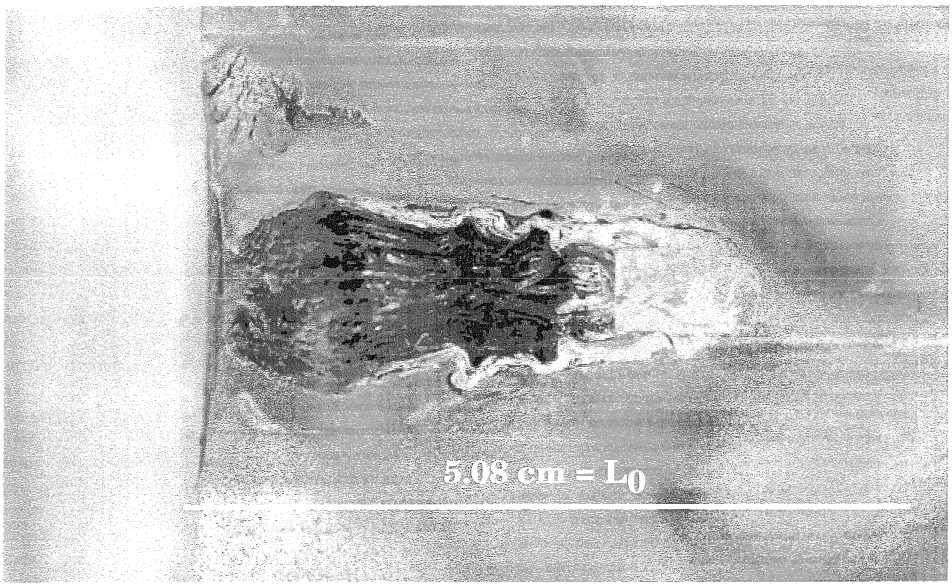

Fig. 4.21. Photograph of metallic glass matrix composite penetrator in 4130 steel target. V=1253 m/s, L/D=8, and P/L = 0.812.

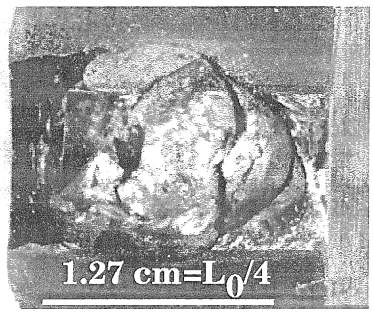

Fig. 4.22. Photograph of WHA (X27C) penetrator in 4130 steel target. V=860 m/s, L/D=8, and P/L = 0.328.

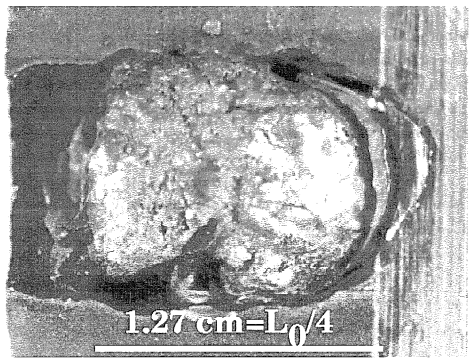

Fig. 4.23. Photograph of WHA (X27C) penetrator in 4130 steel target. V=932 m/s, L/D=8, and P/L = 0.375.

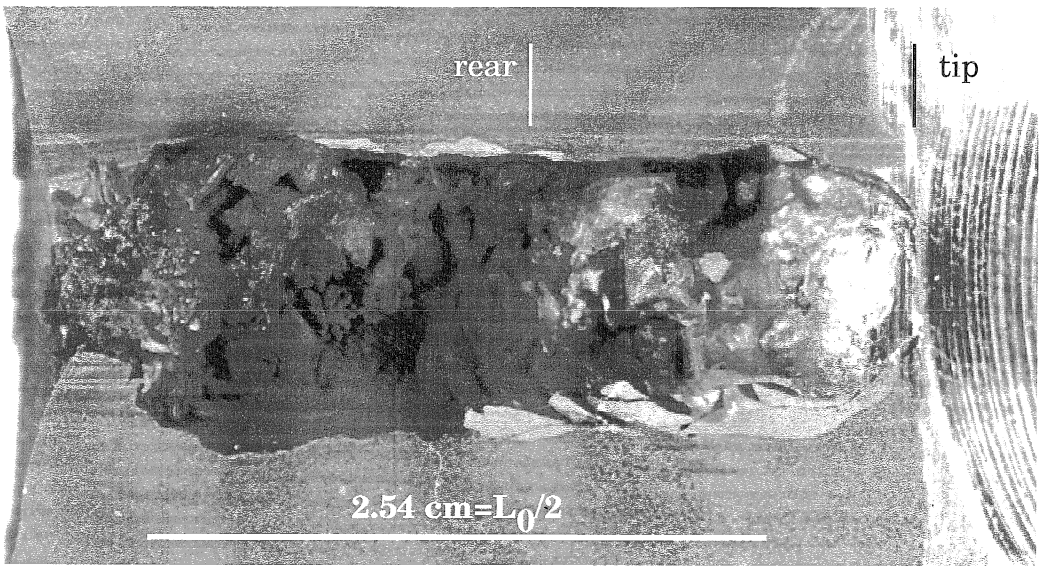

Fig. 4.24. Photograph of WHA (X27C) penetrator in 4130 steel target. V=1269 m/s, L/D=8, and P/L = 0.734.

has expanded to about twice the original diameter of the penetrator. A graph comparing the P/L ratios for the two different materials into steel targets is shown in Fig. 4.25. Like for the aluminum targets, the penetration efficiency is greater for the metallic glass composite penetrators.

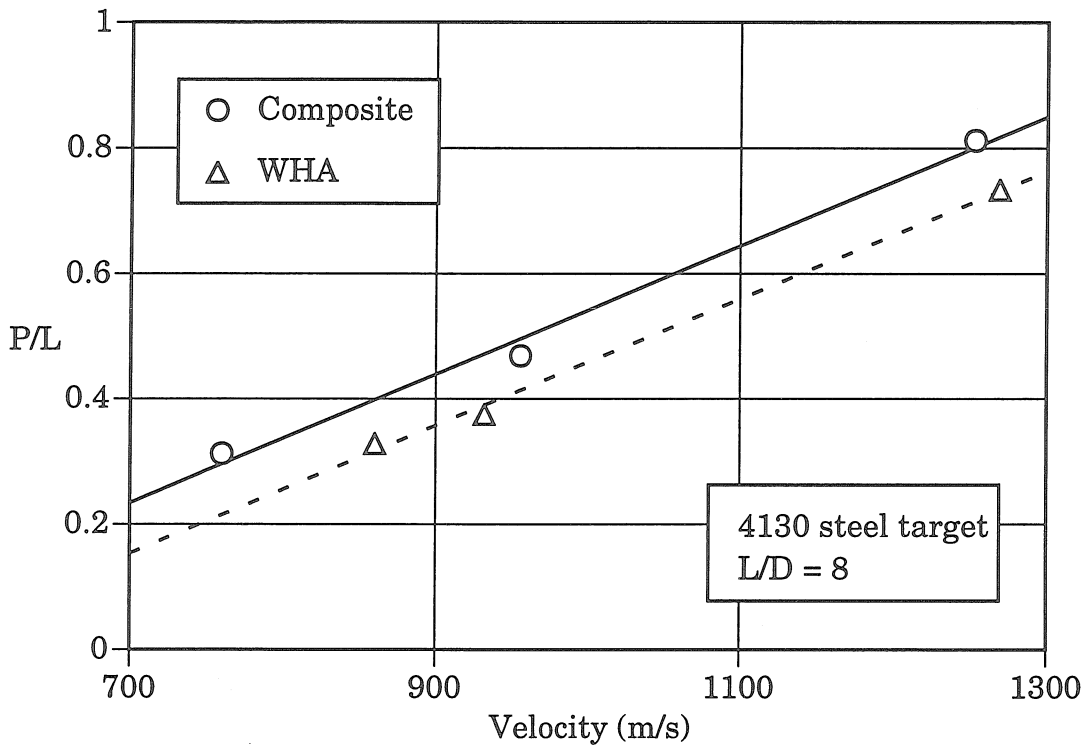

Fig. 4.25. Penetration efficiency versus impact velocity. Target was hardened 4130 steel. Penetrators used were flat-ended rods with L/D=8. Composite was 80 vol% uniaxial tungsten wire in a metallic glass matrix. WHA was the X-27C liquid-sintered tungsten heavy alloy with composition in weight percent of $W_{90.73}Ni_{4.55}Fe_{1.97}Co_{2.75}$.

4.5 CONCLUSIONS

Tungsten-wire-reinforced metallic-glass-matrix composites show promise as a new kinetic energy penetrator material. They can be made with high densities comparable to those of currently used alloys and exhibit more self-sharpening effects in penetration tests than one of the best tungsten heavy alloys. It has been reported in the literature that the WHA typically exhibits limited self-sharpening behavior, while pure tungsten exhibits no self-sharpening.[1] The metallic glass matrix composites would probably fall into the category of self-sharpening, or at least a high degree of limited self-sharpening.

For velocities of about 1 km/s and for penetrator aspect ratio L/D of six to eight, the data in Figs. 4.18 and 4.25 show that the metallic glass composite has approximately a 20 percent improvement in penetrator efficiency over the best WHAs. This improvement is comparable to the improvement in penetrator efficiency provided by depleted uranium alloys. Figs. 4.26 and 4.27 plot the penetration data from this chapter against other published results using similar test parameters. On these plots, the data obtained at Caltech is overall somewhat higher than that from the references, but this may simply be an effect of a lower L/D ratio, which is known to result in higher P/L values.[19] In addition, the different target materials used in the data shown in Fig. 4.27 created a significant difference in the P/L values. To correct for this, the Caltech data has been scaled: the P/L values were reduced so that the WHA values in each data set matched. This provides a more accurate comparison for the metallic glass composite and DU penetrator efficiencies.

There are a number of differences between the series of forward ballistic tests presented in this work and traditional penetrator testing. One is the presence of the sabot and the flyer plate behind the penetrator on impact. It is

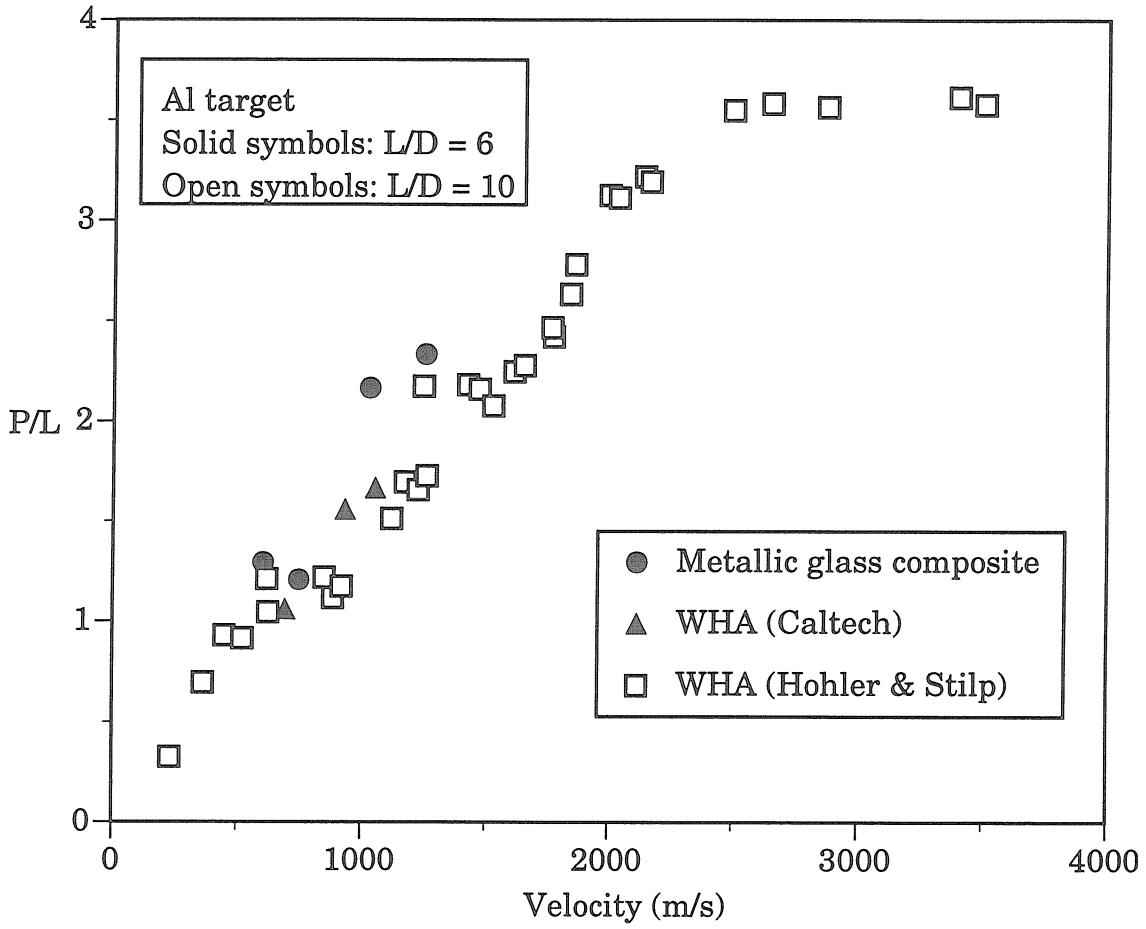

Fig. 4.26. Penetrator efficiency of metallic glass and WHA penetrators versus aluminum targets. L/D values shown for the penetrator. Hohler and Stilp data from ref. 19.

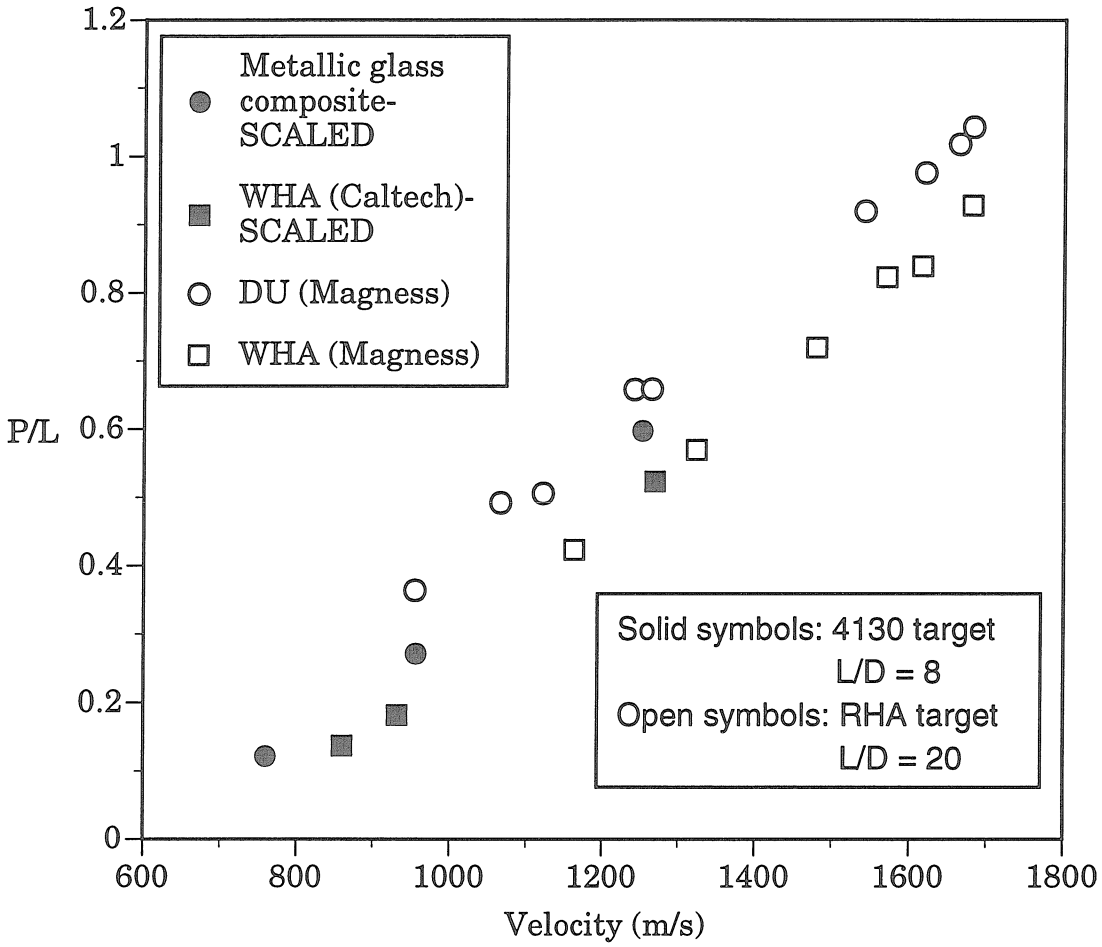

Fig. 4.27. Scaled penetrator efficiency of metallic glass composite, WHA, and depleted uranium penetrators versus steel targets. Caltech data scaled down so that WHA data from both sources match. WHA tests performed at Caltech with X-27C alloy. WHA used by Magness was liquid-sintered 93% tungsten. DU alloy is U-0.75 Ti. Magness data from ref. 4.

conceivable that extra kinetic energy was transferred to the penetrator on impact, thereby increasing the penetration depth. However, in both the tests with aluminum and steel targets, the WHA penetrators gave a suitable reference point for evaluation of the composite penetrator performance. In the aluminum target tests, a backing plate was used, but it was a slightly different size than the one used to test the composites. However, in the tests with steel targets, the entire configuration of the sabot was identical for the composite and the WHA. In addition, if the backing plate truly drove the rod into the steel target, the backing plate itself should have significant deformation. This was not observed.

Further work could include trying to fabricate full scale penetrators and perhaps full scale ballistic tests. In addition, making the composite from different metallic glass alloys, particularly from those without beryllium, would provide advantages in lower cost, simpler processing, and easier material handling. Increases in density would be possible by ensuring close-packing with the wires and using a hafnium-based version of Vitreloy™ 1. It is known that hafnium can be used to replace zirconium in the alloy with no detrimental effects to the glass-forming ability.[20] Through these techniques alone, the density of the composite could be increased up to a theoretical limit of 18.6 $g \cdot cm^{-3}$; 18.4 $g \cdot cm^{-3}$would be well within reach. Increasing the density would certainly increase the penetration efficiency as well.

REFERENCES

1. W. D. Cai, Y. Li, R. J. Dowding, F. A. Mohamed and E. J. Lavernia, *Reviews in Particulate Materials* 3, 71-132 (1995).

2. T. W. Penrice, *Progress in Powder Metallurgy* (edited by M. S. Nayar, S. M. Kaufman and K. E. Meiners), 39, 507, MPIF, Princeton, NJ (1984).

3. R. J. Dowding, *P/M in Aerospace, Defense, and Demanding Applications*, (edited by F. H. Froes), 25, MPIF, Princeton, NJ (1993).

4. L. S. Magness and T. G. Farrand, *Proceedings of the 1990 Army Science Conference*, 465 (1990).

5. K. J. Tauer, R. J. Dowding and P. Woolsey, *Tungsten and Tugnsten Alloys-1992* (edited by A. Bose and R. J. Dowding), 525, MPIF, Princeton, NJ (1992).

6. J. Mescall, in *Computational Aspects of Penetration Mechanics* (edited by J. Chandra and J. E. Flaherty), 47, Springer-Verlag, New York (1982).

7. L. S. Magness, by *Tungsten and Tungsten Alloys-1992* (edited A. Bose and R. J. Dowding), 15, MPIF, Princeton, NJ (1992).

8. M. R. Staker, *Acta Metall.* 29, 683 (1981).

9. D. A. Shockey, in *Metallurgical Applications of Shock-Wave and High-Strain-Rate Phenomena* (edited by L. E. Murr, K. P. Staudhammer and M. A. Meyers), 633, Marcel Dekker, New York (1986).

10. *Smithells Metals Reference Book*, 14.1, Butterworths, London (1983).

11. *Binary Alloy Phase Diagrams*, ASM International, Materials Park, OH (1990).

12. A. Peker and W. L. Johnson, *Appl. Phys. Lett.* 63, 17, 2342-2344 (1993).

13. H. A. Bruck, T. Christman, A. J. Rosakis and W. L. Johnson, *Scripta Metall. Mater.* 30, 4, 429-434 (1994).

14. H. A. Bruck, A. J. Rosakis and W. L. Johnson, *J. Mater. Res.* 11, 2, 503-511 (1996).

15. T. H. Courtney, *Mechanical Behavior of Materials*, McGraw Hill, New York (1990).

16. R. Busch, A. Masuhr, E. Bakke and W. L. Johnson, *MRS 1996 Fall Symp. on Glasses and Glass Formers* (1997).

17. *Metals Handbook*, American Society for Metals, Metals Park, OH (1985).

18. R. J. Dowding, K. J. Tauer, P. Woolsey and F. S. Hodi, *The Metallurgical and Ballistic Characterization of Quarter-Scale Tungsten Alloy Penetrators*, MTL TR 90-31 (Watertown, MA, U.S. Army Materials Technology Laboratory, 1990).

19. Hohler and Stilp, *A penetration mechanics database*, SwRI 3593/001 (San Antonio, TX, Southwest Research Institute, 1992).

20. W. L. Johnson, personal communication (1997).

APPENDIX 1: W interface diffraction measurement

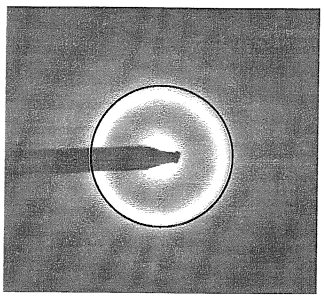

0.74 in dia.

#4738-amorph.

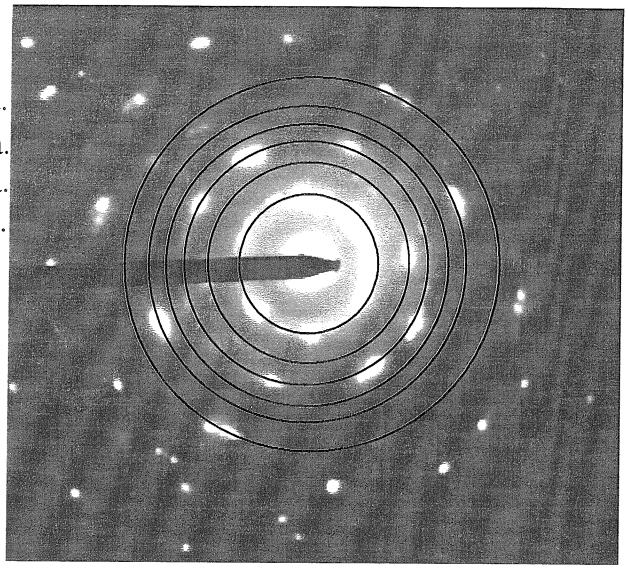

0.74 in dia.
1.05 in dia.
1.27 in dia.
1.47 in dia.
1.65 in dia.
1.95 in dia.

9.4 mm r (2.21 Å)<110>
13.3 mm r (1.56 Å)<200>
16.1 mm r (1.29 Å)<211>
18.7 mm r (**1.11** Å)<220>
21.0 mm r (0.99 Å)<310>
24.8 mm r (0.84 Å)<321>

#4743 rxn. + W

0.315, 0.73, 1.04, 1.26, 1.635, 1.95 in dia.

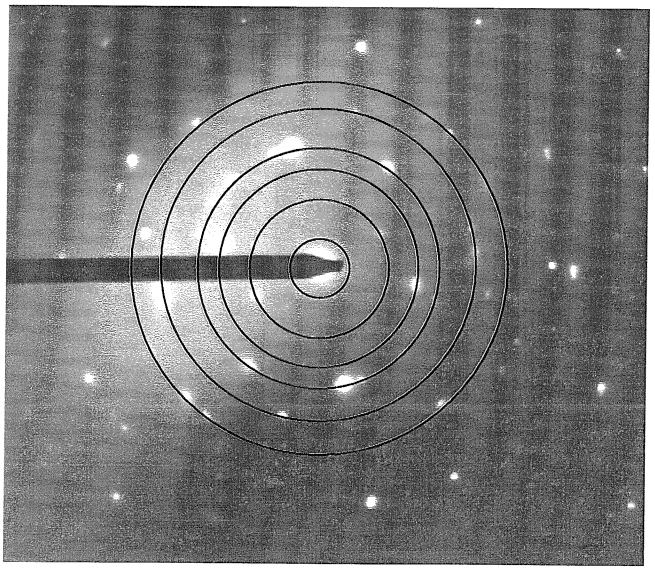

#4737 W only

0.74, 1.05, 1.276, 1.47 in dia.

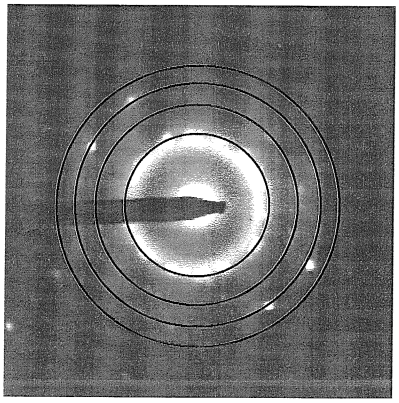

#4742 amorph + rxn.

0.315 in dia.->5.19 Å (110 for $Be_{12}W$->100 rel. intensity)
but no other lines appear (like 61 rel. ints. <101> line @ 3.65 Å)
MOST LIKELY shadow of SAD aperture.

APPENDIX 2

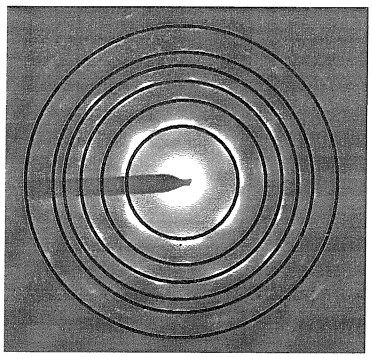

.600 in. dia->
.870 in. dia.->
1.06 in dia.->
1.23 in dia.->
1.357 in. dia.->
1.635 in. dia->

8 μm off interface
into steel

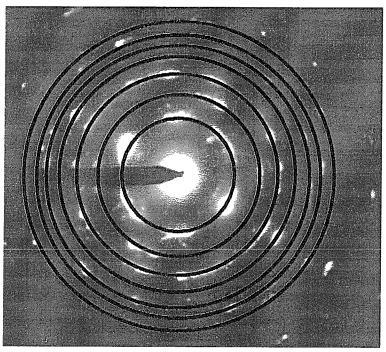

.605 in. dia.->
.858 in. dia.->
1.062 in. dia.->
1.24 in. dia->
1.38 in. dia->
1.487 in. dia->
1.625 in. dia.->

1.5 μm off interface into stl

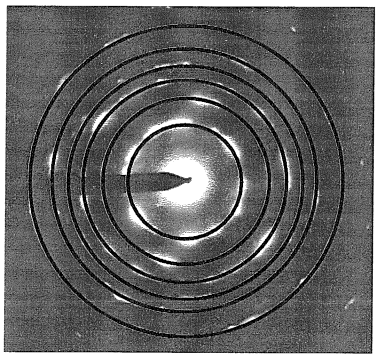

.61 in dia.
.88 in dia
1.07 in dia
1.23 in dia
1.385 in dia
1.635 in dia

.5 μm off interface into stl

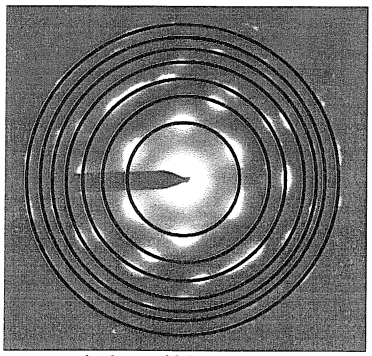

.603 in dia.
.88 in dia
1.065 in dia
1.248 in dia
1.38 in dia
1.63 in dia
1.487 in dia (light)

right off interface

.61 in dia.
0.86 in dia
1.065 in dia.

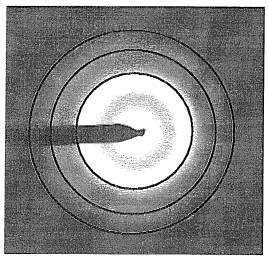

steel/metallic glass interface
2.021.A
6/5/96

dia.(in)->r(mm)->d spacing(Å)
0.605 in->10.24 mm->2.03 Å <110>
0.87 in->14.73 mm->1.41 Å <200>
1.065 in.->18.03 mm->1.15 Å <211>
1.24 in->21.00 mm->0.99 Å <220>
1.37 in.->23.20 mm->0.89 Å <310>
1.487in->25.18 mm->0.82 Å <222>
1.635 in->27.69 mm->0.75 Å <321>

all images at 75% scale
1200 mm nominal camera length
1054 mm actual camera length

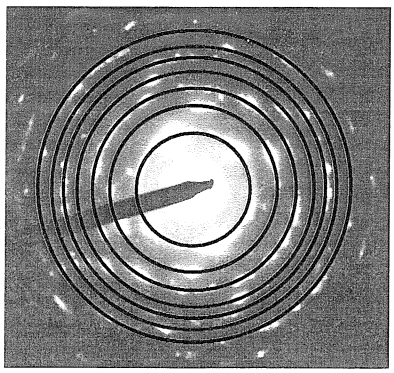

Fig. 3.18: 0.5 μm SAD-
#5093 EDX sample